

UNIVERSITY OF CALIFORNIA  
SANTA CRUZ

**SEARCH FOR  $WW$  AND  $WZ$  RESONANCE PRODUCTION IN  
 $\ell\nu qq$  FINAL STATES IN  $pp$  COLLISIONS AT  $\sqrt{s} = 13$  TEV WITH  
THE ATLAS DETECTOR**

A dissertation submitted in partial satisfaction of the  
requirements for the degree of

DOCTOR OF PHILOSOPHY

in

PHYSICS

by

**Natasha Woods**

December 2019

The Dissertation of Natasha Woods  
is approved:

---

Abraham Seiden, Chair

---

Mike Hance

---

Bruce Schumm

---

Quentin Williams  
Vice Provost and Dean of Graduate Studies

Copyright © by

Natasha Woods

2019

# Table of Contents

List of Figures	vi
List of Tables	xiii
Abstract	xiv
Dedication	xv
Acknowledgments	xvi
<b>I Theoretical Motivation</b>	<b>2</b>
<b>1 The Standard Model of Particle Physics</b>	<b>3</b>
1.1 Introduction . . . . .	3
1.2 Quantum Field Theory . . . . .	3
1.3 $U(1)_{EM}$ Local Gauge Invariance . . . . .	4
1.4 Yang-Mills Gauge Theories . . . . .	7
1.5 Particles in the Standard Model . . . . .	8
1.6 Higgs Mechanism . . . . .	13
1.7 Electroweak Theory . . . . .	14
1.8 Quantum ChromoDynamics . . . . .	15
<b>2 Standard Model Successes and Limitations</b>	<b>20</b>
<b>3 New Physics Models with Diboson Resonances</b>	<b>23</b>
3.1 Randall Sundrum Bulk Model . . . . .	23
3.2 Extended Scalar Sector . . . . .	25
3.3 Simple Standard Model Extensions . . . . .	26

<b>II Experimental Setup</b>	<b>29</b>
<b>4 LHC</b>	<b>30</b>
4.1 LHC Layout and Design . . . . .	32
<b>5 The ATLAS Detector</b>	<b>37</b>
5.1 Coordinate System . . . . .	39
5.2 Inner Detector . . . . .	40
5.2.1 Pixel Detector . . . . .	43
5.2.2 Semiconductor Tracker . . . . .	43
5.2.3 Transition Radiation Tracker . . . . .	43
5.3 Calorimeters . . . . .	45
5.4 Muon Spectrometer . . . . .	48
5.5 Magnet System . . . . .	52
5.6 Trigger System . . . . .	53
<b>III Method</b>	<b>55</b>
<b>6 Dataset and Simulated Samples</b>	<b>56</b>
6.1 Dataset . . . . .	56
6.2 Simulated Samples . . . . .	59
6.3 Object Selection . . . . .	59
6.3.1 Electrons . . . . .	59
6.3.2 Muons . . . . .	60
6.3.3 small-R jets . . . . .	62
6.3.4 large-R jets . . . . .	65
6.3.5 Variable Radius jets . . . . .	68
6.3.6 MET/neutrinos . . . . .	68
6.3.7 Jet Flavor Tagging . . . . .	68
6.3.8 Overlap Removal . . . . .	69
<b>7 Event Selection and Categorization</b>	<b>71</b>
7.1 Pre-selection . . . . .	71
7.2 Trigger . . . . .	71
7.3 GGF/VBF RNN . . . . .	74
7.4 Topological Cuts . . . . .	79
7.5 Background Estimate . . . . .	89
7.5.1 Multijet Sample . . . . .	89
<b>8 Systematic Uncertainties</b>	<b>103</b>
8.1 Experimental Systematics . . . . .	103
8.2 Theory Systematics . . . . .	105

<b>9 Statistical Analysis</b>	<b>113</b>
9.1 Likelihood Function Definition . . . . .	113
9.2 Fit Configuration . . . . .	114
9.3 Best Fit $\mu$ . . . . .	116
9.4 Discovery Test . . . . .	117
9.5 Exclusion Limits . . . . .	118
<b>IV Results</b>	<b>120</b>
<b>10 Statistical Interpretation</b>	<b>121</b>
10.1 Discovery Tests . . . . .	121
10.2 Systematic Profiling and Correlations . . . . .	127
10.3 Expected and Measured Yields . . . . .	127
10.4 Limits . . . . .	127
<b>V Quark and Gluon Tagging</b>	<b>128</b>
<b>11 Prospects</b>	<b>129</b>
<b>12 <math>n_{trk}</math> Calibration</b>	<b>136</b>
<b>13 Application</b>	<b>142</b>
<b>VI Conclusion</b>	<b>147</b>
<b>14 Conclusions</b>	<b>148</b>
<b>Bibliography</b>	<b>149</b>

# List of Figures

1.1	The particles of the Standard Model. . . . .	10
1.2	Summary of how Standard Model particles interact with other Standard Model particles. . . . .	11
1.3	This figure shows the three dominant QCD interactions. From Ref. [14] . . . . .	17
1.4	Strength of the U(1), SU(2), and SU(3) gauge couplings as a function of the energy scale of the interaction ( $Q$ ). From Ref. [10] . . . . .	18
2.1	A comparison of cross section measurements at $\sqrt{s} = 7, 8, 13$ TeV from ATLAS compared to theoretical measurements. From Ref. [5]	22
3.1	Cartoon of RS Bulk Model . . . . .	24
4.1	Scaling of cross sections with $\sqrt{s}$ . Natasha: write more here . . . . .	31
4.2	LHC Layout. Natasha write more . . . . .	33
4.3	LHC Accelerator. Natasha write more . . . . .	35
5.1	Big picture layout of ATLAS detector. Natasha: write more . . . . .	38
5.2	Big picture layout of ATLAS detector. Natasha: write more . . . . .	38
5.3	A simplified schematic of how different particles interact and are detected within ATLAS. . . . .	39
5.4	Layout of ATLAS Inner Detector . . . . .	41
5.5	Layout of ATLAS ID Barrel System. . . . .	42
5.6	Overview of ATLAS electromagnetic and hadronic calorimeters. . . . .	46

5.7	Schematic of ECAL . . . . .	47
5.8	Schematic of HCAL . . . . .	47
5.9	Schematic of Muon Spectrometer [cite G35] . . . . .	50
5.10	Schematic of MDT chamber. [cite G35] . . . . .	51
5.11	Schematic of RPC chamber, which is used for triggering in the central region of the detector [cite G35]. . . . .	51
5.12	Schematic of TGC chamber, which is used for triggering in the muon end-cap region. [cite G35] . . . . .	52
5.13	Layout of ATLAS magnet systems. . . . .	53
6.1	Integrated luminosity for data collected from ATLAS from 2011 - 2018 . . . . .	57
6.2	Mean number of interactions per crossing for data collected from ATLAS from 2011 - 2018 . . . . .	58
6.3	[4] This figure show the breakdown of the muon reconstruction efficiency scale factor measured in $Z \rightarrow \mu\mu$ as a function of $p_T$ . . . . .	62
6.4	[6] This diagram shows the calibration stages for EM jets. . . . .	65
6.5	The upper cut on $D_2$ (a) and jet mass window cut i.e. the upper and lower boundary of the mass (b) of the $W$ -tagger as a function of jet $p_T$ . Corresponding values for $Z$ -tagger are shown in (c) and (d). The optimal cut values for maximum significance are shown as solid markers and the fitted function as solid lines. Working points from $VV \rightarrow JJ$ [ATLAS-HDBS-2018-31-002] is also shown as dashed lines as a reference. Natasha reword? . . . . .	67
6.6	Natasha write caption . . . . .	67
7.1	RNN architecture. Natasha add caption . . . . .	76
7.2	RNN Score distribution for ggF and VBF signals and backgrounds. . . . .	77
7.3	ROC curve using k-fold validation for RNN. . . . .	78
7.4	Comparison of GGF Z' limits for different RNN score selections. . . . .	79
7.5	Event Categorization. Natasha write more. . . . .	82
7.6	Data MC comparison for the merged $WW$ HP TCR. . . . .	83

7.7	Data MC comparison for the merged $WW$ LP TCR. . . . .	84
7.8	Data MC comparison for the merged $WZ$ HP TCR. . . . .	85
7.9	Data MC comparison for the merged $WZ$ LP TCR. . . . .	86
7.10	Data MC comparison for the resolved $WW$ TCR. . . . .	87
7.11	Data MC comparison for the resolved $WZ$ TCR. . . . .	88
7.12	The $E_T^{miss}$ distribution in MJCR for 2017 data in the electron channel(left), muon channel with W-boson pT < 150 GeV (center) and > 150 GeV (right). Multi-jet templates are calculated as remaining data components after excluding known MC . . . . .	91
7.13	Postfit Data/MC comparison of distributions of $E_T^{miss}$ , $m_T^W$ , lepton and neutrino $p_T$ , $m_{\ell\nu jj}$ , lepton- $\nu$ angular distance in the $WW$ electron channel. The MJ template is obtained from the pre-MJ-fit.	92
7.14	Postfit Data/MC comparison of distributions of $E_T^{miss}$ , $m_T^W$ , lepton and neutrino $p_T$ , $m_{\ell\nu jj}$ , lepton- $\nu$ angular distance in the $WW$ muon channel. The MJ template is obtained from the pre-MJ-fit. . . . .	93
7.15	Postfit Data/MC comparison of distributions of $E_T^{miss}$ , $m_T^W$ , lepton and neutrino $p_T$ , $m_{\ell\nu jj}$ , lepton- $\nu$ angular distance in the $WZ$ untag electron channel. The MJ template is obtained from the pre-MJ-fit.	94
7.16	Postfit Data/MC comparison of distributions of $E_T^{miss}$ , $m_T^W$ , lepton and neutrino $p_T$ , $m_{\ell\nu jj}$ , lepton- $\nu$ angular distance in the $WZ$ untag muon channel. The MJ template is obtained from the pre-MJ-fit.	95
7.17	Postfit Data/MC comparison of distributions of $E_T^{miss}$ , $m_T^W$ , lepton and neutrino $p_T$ , $m_{\ell\nu jj}$ , lepton- $\nu$ angular distance in the $WZ$ untag electron channel. The MJ template is obtained from the pre-MJ-fit.	96
7.18	Postfit Data/MC comparison of distributions of $E_T^{miss}$ , $m_T^W$ , lepton and neutrino $p_T$ , $m_{\ell\nu jj}$ , lepton- $\nu$ angular distance in the $WZ$ untag muon channel. The MJ template is obtained from the pre-MJ-fit.	97
7.19	Postfit Data/MC comparison of distributions of $E_T^{miss}$ , $m_T^W$ , lepton and neutrino $p_T$ , $m_{\ell\nu jj}$ , lepton- $\nu$ angular distance in the VBF $WW$ electron channel. The MJ template is obtained from the pre-MJ-fit.	98

7.20 Postfit Data/MC comparison of distributions of $E_T^{miss}$ , $m_T^W$ , lepton and neutrino $p_T$ , $m_{\ell\nu jj}$ , lepton- $\nu$ angular distance in the VBF $WW$ muon channel. The MJ template is obtained from the pre-MJ-fit.	99
7.21 Postfit Data/MC comparison of distributions of $E_T^{miss}$ , $m_T^W$ , lepton and neutrino $p_T$ , $m_{\ell\nu jj}$ , lepton- $\nu$ angular distance in the VBF $WZ$ electron channel. The MJ template is obtained from the pre-MJ-fit.	100
7.22 Postfit Data/MC comparison of distributions of $E_T^{miss}$ , $m_T^W$ , lepton and neutrino $p_T$ , $m_{\ell\nu jj}$ , lepton- $\nu$ angular distance in the VBF $WZ$ muon channel. The MJ template is obtained from the pre-MJ-fit.	101
8.1 The W/Z+jet systematics for the a) Merged ggF, b) Resolved ggF, c) Merged VBF, and d) Resolved VBF regions. The top subplot shows the nominal and variation distributions/bands, the middle shows the ratio of the two, and the final shows just the shape of the envelope (the final uncertainty).	107
8.2 The two-point generator comparison between Sherpa and MadGraph for the W/Z+jet samples in the a) Merged ggF, b) Resolved ggF, c) Merged VBF, and d) Resolved VBF regions. The normalization of the Madgraph sample is set to the Sherpa value to consider only shape effects. The bottom inlet shows the ratio of the two.	108
8.3 Ratio between the variations of generator (red) and hadronization (blue) variations for the Merged regime for $t\bar{t}$ sample.	109
8.4 Ratio between the variations of generator (red) and hadronization (blue) variations for the Resolved regime for $t\bar{t}$ sample.	109
8.5 Ratio between the variations of ISR up (red) and down (blue) variations for the Merged regime for $t\bar{t}$ sample.	110
8.6 Ratio between the variations of ISR up (red) and down (blue) variations for the Resolved regime for $t\bar{t}$ sample.	111
8.7 Ratio between the variations of FSR up (red) and down (blue) variations for the Merged regime for $t\bar{t}$ sample.	112

8.8	Ratio between the variations of FSR up (red) and down (blue) variations for the Resolved regime for $t\bar{t}$ sample. . . . .	112
9.1	The HVT signal mass resolution as a function of mass fit with a straight line in the Resolved ggF region (left) and VBF (right) region. . . . .	116
9.2	The HVT signal mass resolution as a function of mass fit with a straight line in the Merged ggF region (left) and VBF (right) region. . . . .	116
10.1	These plots show the measured $p_0$ value as a function of resonance mass for HVT Z' DY production. . . . .	122
10.2	These plots show the measured $p_0$ value as a function of resonance mass for HVT Z' VBF production. . . . .	123
10.3	These plots show the measured $p_0$ value as a function of resonance mass for HVT W' DY production. . . . .	124
10.4	These plots show the measured $p_0$ value as a function of resonance mass for HVT W' VBF production. . . . .	125
10.5	These plots show the measured $p_0$ value as a function of resonance mass for the RS Graviton DY production. . . . .	126
11.1	PDGID of the truth-level parton matched to the small-R jets passing the Resolved GGF WW Signal Region selections for the (a) Leading (b) Sub-Leading jets . These distributions are shown for 300, 500, and 700GeV Z' signals and the background. . . . .	131
11.2	The number of tracks in small-R jets in events passing the Resolved GGF WW Signal Region selections for the (a) Leading (b) Sub-Leading jets. These distributions are shown for 300, 500, and 700GeV Z' signals and the background. . . . .	131

11.3 The number of tracks in background small-R jets in events passing the Resolved GGF WW Signal region selection vs. $\ln(p_T)$ for (a)Leading (b) Sub-Leading jets. The best fit line for the distribution is also shown, as well as the percentage of jets that pass a cut of number of tracks $< 4 \times \ln(p_T) - 5$ . Note the number of total entries in these plots has been normalized to one. . . . .	132
11.4 The number of tracks in small-R jets in 300GeV Z' events passing the Resolved GGF WW Signal region selection vs. $\ln(p_T)$ for (a)Leading (b) Sub-Leading jets. The best fit line for the distribution is also shown, as well as the percentage of jets that pass a cut of number of tracks $< 4 \times \ln(p_T) - 5$ .Note the number of total entries in these plots has been normalized to one. . . . .	132
11.5 The number of tracks in small-R jets in 500GeV Z' events passing the Resolved GGF WW Signal region selection vs. $\ln(p_T)$ for (a)Leading (b) Sub-Leading jets. The best fit line for the distribution is also shown, as well as the percentage of jets that pass a cut of number of tracks $< 4 \times \ln(p_T) - 5$ .Note the number of total entries in these plots has been normalized to one. . . . .	133
11.6 The number of tracks in small-R jets in 700GeV Z' events passing the Resolved GGF WW Signal region selection vs. $\ln(p_T)$ for (a)Leading (b) Sub-Leading jets. The best fit line for the distribution is also shown, as well as the percentage of jets that pass a cut of number of tracks $< 4 \times \ln(p_T) - 5$ .Note the number of total entries in these plots has been normalized to one. . . . .	133
11.7 The number of tracks in leading small-R jets in background events passing the Resolved GGF WW Signal region selection vs. $\ln(p_T)$ for (a)Gluons (b) Quarks jets. The best fit line for the distribution is also shown, as well as the percentage of jets that pass a cut of number of tracks $< 4 \times \ln(p_T) - 5$ .Note the number of total entries in these plots has been normalized to one. . . . .	134

11.8 ROC Curve for Quark and Gluon Tagging with a cut on the number of tracks that depends on the $\ln(p_T)$ . . . . .	134
11.9 The top panel shows the distribution of $m_{lvqq}$ with and without quark gluon tagging. The middle panel shows the ratio of the signals and backgrounds with and without quark gluon tagging. The bottom panel shows the change in $S/\sqrt{B}$ with quark gluon tagging. . . . .	135
13.1 The top panel shows the distribution of $m_{lvqq}$ with and without requiring jets to be true quarks. The middle panel shows the ratio of the signals and backgrounds with and without requiring jets to be true quarks. The bottom panel shows the change in $S/\sqrt{B}$ when requiring jets to be true quarks. . . . .	143
13.2 Unfolded and extracted $n_C$ qg dstbs. . . . .	144
13.3 PDGID of the truth-level parton matched to the small-R jets passing the Resolved GGF WW Signal Region selections for the (a) Leading (b) Sub-Leading jets . These distributions are shown for 300, 500, and 700GeV Z' signals and the background. . . . .	145
13.4 These figures show the impact of the uncertainties on the number of tracks in the leading jet in the sum of the background sample in the Resolved GGF WW SR (a) tracking efficiency (b) fake (c) PDF (d) ME (e) unfolding uncertainties. . . . .	146

# List of Tables

1.1	Representations of the SM fermions under $SU(3)_C \times SU(2)_L \times U(1)_Y$ gauge symmetry group. $SU(2)_L$ gauge transformations allow one to go between rows and $SU(3)_C$ transformations allow one to go between columns in these fermion representations. [REWORD]	9
7.1	The list of triggers used in the analysis. . . . .	73
7.2	Summary of selection criteria used to define the signal region (SR), $W$ +jets control region ( $W$ CR) and $t\bar{t}$ control region ( $t\bar{t}$ CR) for merged 1-lepton channel. . . . .	81
7.3	The list of selection cuts in the resolved analysis for the $WW$ and $WZ$ signal regions (SR), $W$ +jets control region (WR) and $t\bar{t}$ control region (TR). . . . .	82
7.4	Definitions of “inverted” leptons used in multijet control region . .	90
7.5	Fit validation result in WCRs for 2015+16 data. The fit is done in various WCRs, in order to obtain the corresponding scale factors for MJ templates: ggF resolved WCR for the $WW \rightarrow lvqq$ selection, ggF resolved untagged WCR for the $WZ \rightarrow lvqq$ selection, ggF resolved tagged WCR for the $WZ \rightarrow lvqq$ selection, VBF resolved WCR for the $WW \rightarrow lvqq$ selection, and VBF resolved WCR for the $WZ \rightarrow lvqq$ selection. Post-fit event yields for electroweak processes and MJ contributions are shown. The SF column shows the corresponding normalization scale factors for electroweak processes from the fit. R.U. stands for relative uncertainty. . . . .	102

## Abstract

Search for  $WW$  and  $WZ$  resonance production in  $\ell\nu qq$  final states in  $pp$  collisions at  $\sqrt{s} = 13$  TeV with the ATLAS detector

by

Natasha Woods

This thesis reviews a search for  $WW$  and  $WZ$  resonance production using data from  $pp$  collisions at  $\sqrt{s} = 13$  TeV using the ATLAS detector, corresponding to an integrated luminosity of  $139 \text{ fb}^{-1}$ . Diboson resonances are predicted in a number of Standard Model (SM) extensions, such as Extended Gauge Models, Extra dimensions, and technicolor models. This search looks for resonances where one  $W$  boson decays leptonically and the other  $W$  or  $Z$  boson decays hadronically. This search is sensitive to diboson resonance production via vector-boson fusion as well as quark-antiquark annihilation and gluon-gluon fusion mechanisms. No significant excess of events is observed with respect to the Standard Model backgrounds. As the dominant backgrounds in this search contain gluons, classifying jets as quark or gluon initiated would make this analysis more sensitive to new physics. Towards this end, this thesis considers the prospects for adding a quark gluon tagger based on the number of tracks in jets and reviews the calibration of the number of tracks in jets.

A loving dedication.

å

## **Acknowledgments**

Proper acknowledgments of everyone else who helped you graduate. Write later.

<sub>1</sub> another intro???

<sup>2</sup>

## Part I

<sup>3</sup>

# Theoretical Motivation

<sup>4</sup> **Chapter 1**

<sup>5</sup> **The Standard Model of Particle  
6 Physics**

<sup>7</sup> **1.1 Introduction**

<sup>8</sup> By determining the dynamics of the most elementary degrees of freedom, par-  
<sup>9</sup> ticle physics hopes to uncover the fundamental laws of the universe. The definition  
<sup>10</sup> of elementary has evolved through time and currently refers to matter and force  
<sup>11</sup> mediating particles: fermions and bosons, respectively. The Standard Model of  
<sup>12</sup> Particle Physics (SM) describes the quantum behavior of three of the four funda-  
<sup>13</sup> mental forces: weak, strong, and electromagnetic, via boson and fermion interac-  
<sup>14</sup> tions. Gravity is not included in the SM and still under investigation.

<sup>15</sup> **1.2 Quantum Field Theory**

<sup>16</sup> In the SM, forces (and particles) are represented as fields. In this context,  
<sup>17</sup> fields are mathematical objects that define a tensor (e.g. scalar, vector, etc) at  
<sup>18</sup> every point on a manifold, here the manifold is space-time. These fields obey laws

<sup>19</sup> dictated by Quantum Field Theory (QFT). Particles arise naturally in QFT as  
<sup>20</sup> quantized field excitations localized in spacetime.

<sup>21</sup> According to Noether's theorem, symmetries of a field give rise to conserved  
<sup>22</sup> quantities (e.g. time-translation invariance leads to energy conservation). Often  
<sup>23</sup> in the history of physics, a conserved quantity of a field is found and then the  
<sup>24</sup> underlying symmetry of the field is inferred. Gauge symmetries are symmetries  
<sup>25</sup> among the internal degrees of freedom of the field (components of the tensor),  
<sup>26</sup> which give rise to quantities associated with fields. By specifying the symmetries  
<sup>27</sup> of a system the dynamics and conserved quantities of the system may be succinctly  
<sup>28</sup> defined.

### <sup>29</sup> 1.3 $U(1)_{EM}$ Local Gauge Invariance

<sup>30</sup> The Lagrangian of Quantum Electrodynamics (QED) describes the electro-  
<sup>31</sup> magnetic force. QED may be derived by requiring local  $U(1)_{EM}$  gauge invariance  
<sup>32</sup> of the free dirac fermion Lagrangian,  $\psi$ :

$$\mathcal{L} = i\bar{\psi}\gamma^\mu\partial_\mu\psi - m\bar{\psi}\psi \quad (1.1)$$

<sup>33</sup> This symmetry may be represented as a complex number with unit modulus,  
<sup>34</sup>  $e^{i\theta}$ .  $U(1)$  gauge invariance requires this gauge transformation of  $\psi$  will leave the  
<sup>35</sup> Lagrangian unchanged.

$$\psi(x) \rightarrow \psi'(x) = e^{i\theta(x)}\psi(x) \quad (1.2)$$

<sup>36</sup> NB: This transformation is a local gauge transformation as  $\theta$  depends on the  
<sup>37</sup> spacetime coordinate.

<sup>38</sup> By requiring this symmetry of the free Dirac fermion Lagrangian:

$$\mathcal{L} = i\bar{\psi}\gamma^\mu\partial_\mu\psi - m\bar{\psi}\psi \quad (1.3)$$

<sup>39</sup> The mass term is unaffected, but the kinetic term is modified due to  $\theta(x)$ .

$$\mathcal{L} \rightarrow \mathcal{L}' = i\bar{\psi}e^{-i\theta(x)}\gamma^\mu\partial_\mu\psi e^{i\theta(x)} - m\bar{\psi}e^{-i\theta(x)}\psi e^{i\theta(x)} \quad (1.4)$$

<sup>40</sup>

$$= i\psi\gamma^\mu(\partial_\mu\psi + i\psi\partial_\mu\theta) - m\bar{\psi}\psi \quad (1.5)$$

<sup>41</sup> The  $\partial_\mu\theta$  terms breaks the gauge invariance of the Lagrangian. By introducing a  
<sup>42</sup> new field,  $A_\mu$  we can recover the gauge invariance of the derivative. Now redefining  
<sup>43</sup> the derivative as the covariant derivative:

$$D_\mu\psi \equiv (\partial_\mu - iqA_\mu)\psi \quad (1.6)$$

<sup>44</sup> And letting  $A_\mu$  transform under  $U(1)$  as:

$$A_\mu \rightarrow A_\mu + \delta A_\mu \quad (1.7)$$

<sup>45</sup> The transformed covariant derivative becomes:

$$D_\mu\psi \rightarrow D_\mu\psi' = (\partial_\mu - iqA_\mu)\psi' \quad (1.8)$$

<sup>46</sup>

$$= (\partial_\mu - iq(A_\mu + \delta A_\mu))\psi e^{i\theta} \quad (1.9)$$

<sup>47</sup>

$$= e^{i\theta}D_\mu + ie^{i\theta}\psi(\partial_\mu\theta - q\delta A_\mu) \quad (1.10)$$

<sup>48</sup> The covariant derivative can be made gauage invariant by setting the last term  
<sup>49</sup> to zero.

$$\delta A_\mu = \frac{1}{q} \partial_\mu \theta \quad (1.11)$$

50 So now  $A_\mu$  transforms as:

$$A_\mu \rightarrow A_\mu + \frac{1}{q} \partial_\mu \theta \quad (1.12)$$

51 Finally, replacing the derivative with the covariant derivative the Dirac La-  
52 grangian we have:

$$\mathcal{L} = i\bar{\psi}\gamma^\mu D_\mu \psi - m\bar{\psi}\psi - \frac{1}{4}F_{\mu\nu}F^{\mu\nu} \quad (1.13)$$

53

$$= \mathcal{L}_{QED} \quad (1.14)$$

54 Here  $F_{\mu\nu} \equiv \partial_\mu A_\nu - \partial_\nu A_\mu$ . This last term in the Lagrangian is the kinetic  
55 energy of the gauge boson field.

56 So we have derived the QED Lagrangian. By requiring the free Dirac La-  
57 grangian to be invariant under U(1) transformations we have generated a new  
58 gauge boson field,  $A_\mu$ , which describes the photon. As expected the photon inter-  
59 acts with fermions.

60 Stepping back, a global U(1) gauge symmetry of the free Dirac Lagrangian  
61 implies we cannot measure the absolute phase of a charged particle. A local U(1)  
62 gauge symmetry changes the phase of fields differently across space time. For this  
63 type of transformation to leave the Lagrangian invariant, we had to introduce an  
64 additional field,  $A_\mu$ , which "communicates" these phase changes across space-time.  
65 In less formal language this effectively means: if the field at one location changes,  
66 this change is conferred to other particles via  $A_\mu$ .

## 67 1.4 Yang-Mills Gauge Theories

68 Requiring  $U(1)_{EM}$  gauge invariance of the free Dirac Lagrangian gave us QED.

69 Requiring different gauge symmetries we can derive the structure of other inter-  
70 actions. Any gauge symmetry may be written as:

$$\psi_i \rightarrow \exp(i\theta^a T_{ij}^a) \psi_j \quad (1.15)$$

71 Here  $\theta$  is a dimensionless real parameter and  $T$  is the generator of the gauge  
72 symmetry group. With this the covariant derivative can be written as:

$$D_\mu \psi_i \equiv \partial_\mu \psi_i + ig A_\mu^a T_{ij}^a \psi_j \quad (1.16)$$

73 Then the gauge field must transform as:

$$A_\mu^a \rightarrow A_\mu^a - \frac{1}{g} \partial_\mu \theta^a - f^{abc} \theta^b A_\mu^c \quad (1.17)$$

74 Here  $f$  is the structure constant of the gauge group. The field strength tensor  
75 is given by:

$$F_{\mu\nu}^a \equiv \partial_\mu A_\nu^a - \partial_\nu A_\mu^a - g f^{abc} A_\mu^b A_\nu^c \quad (1.18)$$

76

$$F_{\mu\nu}^a \rightarrow F_{\mu\nu}^a - f^{abc} \theta^b F_{\mu\nu}^c \quad (1.19)$$

77 This gives the Yang-Mills Lagrangian:

$$\mathcal{L}_{YM} = -\frac{1}{4} F_{\mu\nu}^a F_{\mu\nu}^a + i \bar{\psi}_i \gamma^\mu D_\mu \psi_i + m \bar{\psi}_i \psi_i \quad (1.20)$$

## 78 1.5 Particles in the Standard Model

79 The SM consists of fermions (half-integer spin matter constituents) and bosons  
80 (integer spin force mediators). Fermions are spinor representations of the Poincare  
81 group and can be further separated into leptons and quarks. Bosons are the result  
82 of requiring a particular symmetry among the spinor fields:

$$SU(3)_C \times SU(2)_L \times U(1)_Y \quad (1.21)$$

83  $SU(3)_C$  is the symmetry group of the strong force and generates eight gluon  
84 fields,  $G_\mu$ .  $SU(2)_L$  is the symmetry group of the Electroweak force and generates  
85 three electroweak boson fields, and  $U(1)_Y$  generates the photon field, where  $Y$  is  
86 the weak-hypercharge:

$$Y = 2(Q - T_3) \quad (1.22)$$

87  $Q$  is the electromagnetic charge, and  $T_3$  is the z-component of the weak isospin.  
88 Weak isospin is the charge associated with the  $SU(2)_L$  symmetry. The correspond-  
89 ing covariant derivative is then:

$$D_\mu \phi \equiv (\partial_\mu + ig_1 B_\mu Y_{L/R} + [ig_2 W_\mu^\alpha T^\alpha]_L + [ig_3 G_\mu^\alpha \tau^\alpha]_C) \psi \quad (1.23)$$

90 It is important to note that the gauge symmetry of the SM yields a particular  
91 structure of the fermion representations. So for a given fermion to interact with  
92 a given gauge field it must have a non-zero corresponding Noether charge for  
93 that gauge symmetry. If the corresponding Noether charge is zero, that fermion  
94 transforms as a singlet and does not participate in that gauge interaction.

95 Fermions are divided into quarks and leptons based on their transformations  
96 under  $SU(3)_C$ . Quarks transform as color triplets. Leptons transform as color

singlets and consequently do not interact with gluons. Fermions may be further  
 classified by their  $SU(2)_L$  interactions. Only the left-chiral part of fermions (denoted by L here) transform as  $SU(2)_L$  doublets, the right-chiral part forms singlets under this gauge. Lastly, all these groups of particles come in three generations, each a heavier copy of the previous, but with differing flavor quantum numbers.  
 This is summarized in Table 1.1 and shown in Figures 1.1 and 1.2.

SM Fermion Gauge Group	First Generation	Second Generation	Third Generation	$(SU(3)_C, SU(2)_L, U(1)_Y)$ Representations
Left-handed quarks	$\begin{pmatrix} u_L^r & u_L^g & u_L^b \\ d_L^r & d_L^g & d_L^b \end{pmatrix}$	$\begin{pmatrix} c_L^r & c_L^g & c_L^b \\ s_L^r & s_L^g & s_L^b \end{pmatrix}$	$\begin{pmatrix} t_L^r & t_L^g & t_L^b \\ b_L^r & b_L^g & b_L^b \end{pmatrix}$	$(3, 2, \frac{1}{6})$
Right-handed quarks	$(u_R^r, u_R^g, u_R^b)$ $(d_R^r, d_R^g, d_R^b)$	$(c_R^r, c_R^g, c_R^b)$ $(s_R^r, s_R^g, s_R^b)$	$(t_R^r, t_R^g, t_R^b)$ $(b_R^r, b_R^g, b_R^b)$	$(3, 1, \frac{2}{3})$ $(3, 1, -\frac{1}{3})$
Left-handed leptons	$\begin{pmatrix} \nu_e^L \\ e_L \end{pmatrix}$	$\begin{pmatrix} \mu_e^L \\ \mu_L \end{pmatrix}$	$\begin{pmatrix} \tau_e^L \\ \tau_L \end{pmatrix}$	$(1, 2, -\frac{1}{2})$
Right-handed leptons	$e_R$	$\mu_R$	$\tau_R$	$(1, 1, -1)$

**Table 1.1:** Representations of the SM fermions under  $SU(3)_C \times SU(2)_L \times U(1)_Y$  gauge symmetry group.  $SU(2)_L$  gauge transformations allow one to go between rows and  $SU(3)_C$  transformations allow one to go between columns in these fermion representations. [REWORD]

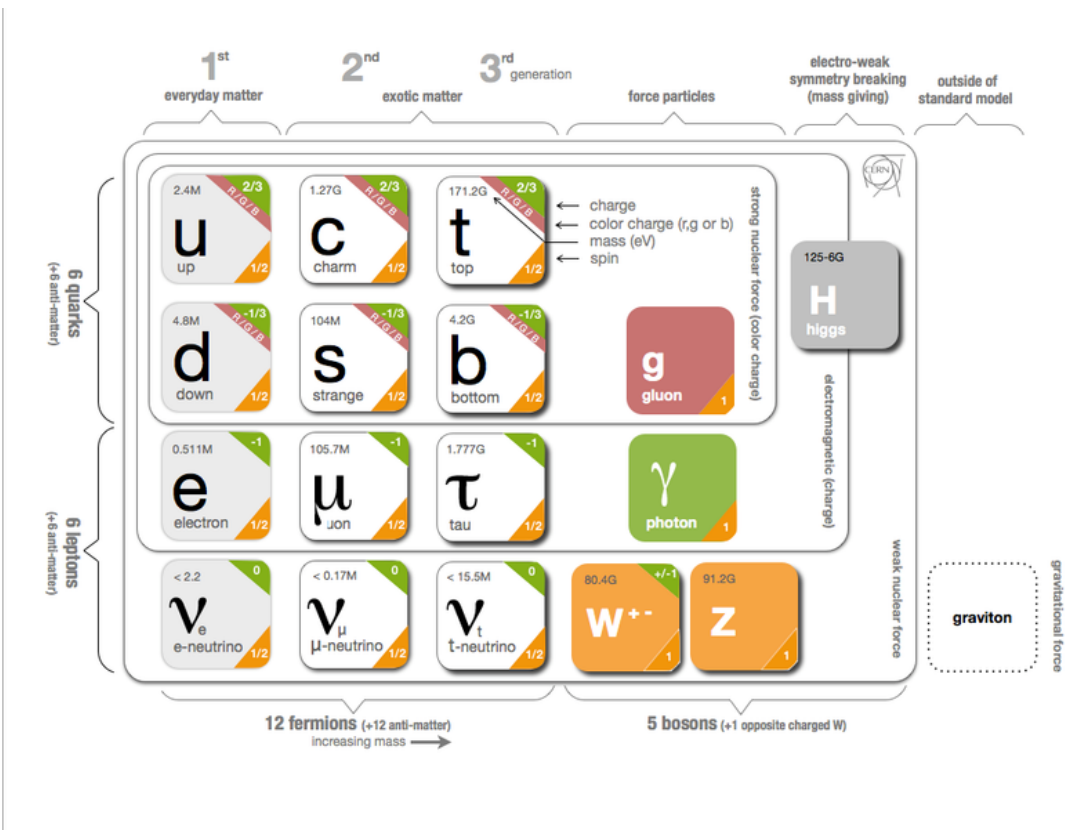


**Figure 1.1:** The particles of the Standard Model.

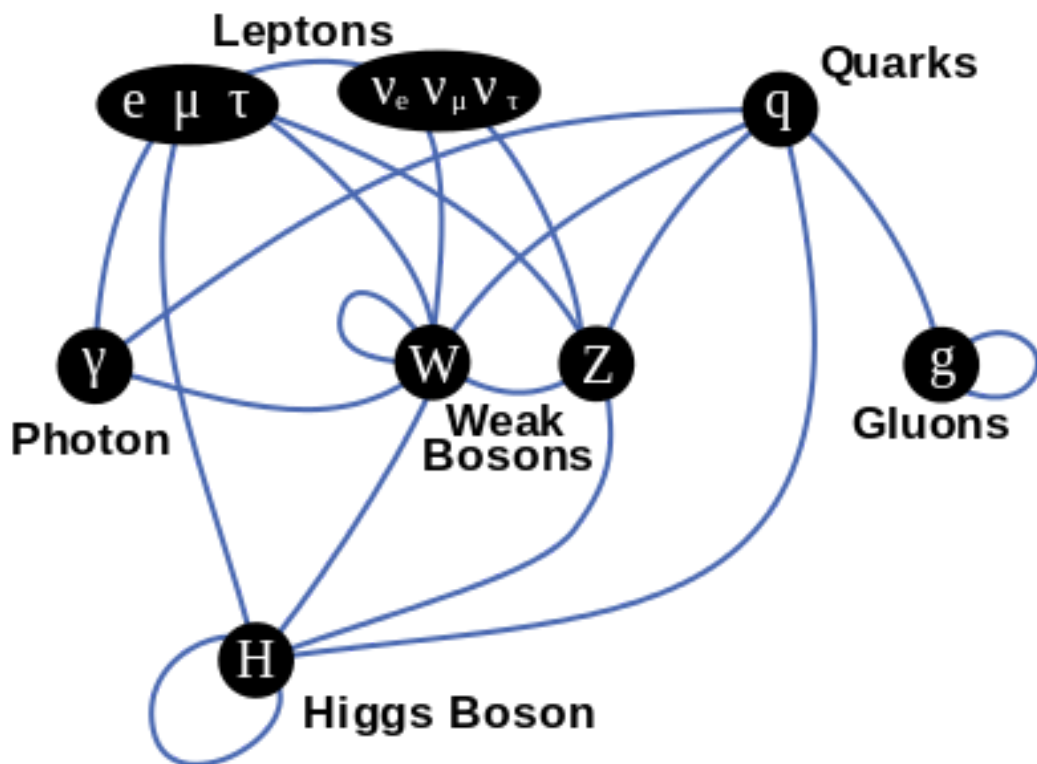


**Figure 1.2:** Summary of how Standard Model particles interact with other Standard Model particles.

<sup>103</sup> Now we can understand the SM Lagrangian density as a Yang-Mills theory  
<sup>104</sup> with the gauge group:  $SU(3)_C \times SU(2)_L \times U(1)_Y$  with an additional  $SU(2)$  complex  
<sup>105</sup> scalar Higgs field doublet that will be discussed later.

$$\begin{aligned} \mathcal{L}_{SM} = & \underbrace{-\frac{1}{4}B_{\mu\nu}B^{\mu\nu} - \frac{1}{4}W_{\mu\nu}^aW^{a\mu\nu} - \frac{1}{4}G_{\mu\nu}^\alpha G^{\alpha\mu\nu}}_{\text{Kinetic Energies and Self-Interactions of Gauge Bosons}} \\ & + \underbrace{\bar{L}_i \gamma^\mu (i\partial_\mu - \frac{1}{2}g_1 Y_{iL} B_\mu - \frac{1}{2}g_2 \sigma^a W_\mu^a) L_i}_{\text{Kinetic Energies and EW Interactions of Left-handed Fermions}} \\ & + \underbrace{\bar{R}_i \gamma^\mu (i\partial_\mu - \frac{1}{2}g_1 Y_{iR} B_\mu) R_i}_{\text{Kinetic Energies and EW Interactions of Right-Handed Fermions}} \\ & + \underbrace{\frac{ig_3}{2} \bar{Q}_j \gamma^\mu \lambda^\alpha G_\mu^\alpha Q_j}_{\text{Strong Interactions between Quarks and Gluons}} \\ & + \underbrace{\frac{1}{2} |(i\partial_\mu - \frac{1}{2}g_1 B_\mu - \frac{1}{2}g_2 \sigma^a W_\mu^a)\Phi|^2 - V(\Phi)}_{\text{Electroweak Boson Masses and Higgs Couplings}} \\ & - (\underbrace{y_{kl}^d \bar{L}_k \Phi R_l + y_{kl}^u \bar{R}_k \tilde{\Phi} L_l}_{\text{Fermion Mass terms and Higgs Couplings}} + h.c.) \end{aligned}$$

<sup>106</sup> Here several abstract spaces are being spanned:

- <sup>107</sup> –  $a$  spans the three  $SU(2)_L$  gauge fields with generators expanded in Pauli  
<sup>108</sup> matrices,  $T^\alpha = \frac{1}{2}\sigma^\alpha$
- <sup>109</sup> –  $\alpha$  spans the eight  $SU(3)_C$  gauge fields, with generators expanded in Gell-  
<sup>110</sup> Mann matrices,  $\tau^\alpha = \frac{1}{2}\lambda^\alpha$
- <sup>111</sup> – L/R represent left and right projections of Dirac fermion fields. The Strong  
<sup>112</sup> interaction is not chiral, so  $Q = L+R$

113 –  $\mu$  and  $\nu$  are four-vector indices

114 –  $i, j, k$  are summed over the three generations of SM particles.

## 115 1.6 Higgs Mechanism

116 The SM Lagrangian without the addition of a Higgs field does not allow for  
117 gauge boson and fermion mass terms:  $\frac{1}{2}m_A^2 A_\mu A_\mu$  and  $m(\bar{\psi}\psi)$ , as these terms are  
118 not gauge invariant. By introducing the Higgs field, mass terms for these particles  
119 may be included in a gauge invariant way. This field is a complex doublet with a  
120 potential  $V(\Phi)$ :

$$\Psi = \begin{pmatrix} \Phi^\dagger \\ \Phi^0 \end{pmatrix} \quad (1.24)$$

121  $V(\Phi) = \mu^2 \Phi^\dagger \Phi + \lambda |\Phi^\dagger \Phi|^2 \quad (1.25)$

122 The minima of this field occurs for  $|\Phi| = \sqrt{\frac{\mu^2}{2\lambda}} \equiv \frac{v}{2}$ . This yields degenerate  
123 minima, this symmetry is broken by choosing a specific minima (a.k.a. sponta-  
124 neous symmetry breaking). By convention  $\Phi_{min} = \frac{1}{\sqrt{2}} \begin{pmatrix} 0 \\ v \end{pmatrix}$  is chosen. This means  
125 the ground state of the Higgs field (Higgs vacuum) is non-zero,  $\sqrt{\frac{-\mu^2}{\lambda}}$ . The Higgs  
126 Field may now be expanded around this new ground state:

$$\Phi(x) = \frac{1}{\sqrt{2}} \begin{pmatrix} 0 \\ v + h(x) \end{pmatrix} \quad (1.26)$$

127 This non-zero Higgs vacuum now generates mass terms for the gauge bosons  
128 from the following term in the Lagrangian:

$$|(-\frac{1}{2}g_1B_\mu - \frac{1}{2}g_2\sigma^aW_\mu^a)\Phi|^2 = \frac{1}{2}m_W^2W_\mu^+W^{-\mu} + \frac{1}{2}m_Z^2Z_\mu Z^\mu \quad (1.27)$$

129 where:

$$W_\mu^\pm \equiv \frac{1}{\sqrt{2}}(W_\mu^1 \mp iW_\mu^2) \quad (1.28)$$

$$\begin{aligned} \text{130} \quad Z_\mu &\equiv \frac{1}{\sqrt{g_1^2 + g_2^2}}(g_2W_\mu^2 - g_1B_\mu) \end{aligned} \quad (1.29)$$

$$\begin{aligned} \text{131} \quad m_W &= \frac{vg_2}{\sqrt{2}} \end{aligned} \quad (1.30)$$

$$\begin{aligned} \text{132} \quad m_Z &= \frac{v}{\sqrt{2}}\sqrt{g_1^2 + g_2^2} \end{aligned} \quad (1.31)$$

133 The Higgs field also generates a mass term for the Higgs boson and self-  
134 interactions for the Higgs boson.

## 135 1.7 Electroweak Theory

136  $SU(2)_L$  generates  $W^\pm, W^0$  gauge bosons, which would be massless if  $SU(2)_L$   
137 was a perfect symmetry. These bosons are massive as this symmetry is broken.

138 The mass eigenstates,  $Z$  and  $\gamma$  given by:

$$\begin{pmatrix} Z_\mu \\ A_\mu \end{pmatrix} = \begin{pmatrix} \cos\theta_W & -\sin\theta_W \\ \sin\theta_W & \cos\theta_W \end{pmatrix} \begin{pmatrix} W_\mu^3 \\ B_\mu \end{pmatrix} \quad (1.32)$$

139 Here  $\theta_W$  is the Weinberg angle given by:

$$\cos\theta_W = \frac{g_2}{\sqrt{g_1^2 + g_2^2}} = \frac{m_W}{m_Z} \quad (1.33)$$

## <sup>140</sup> 1.8 Quantum ChromoDynamics

<sup>141</sup> As mentioned earlier the Strong Force, which binds the proton together, is  
<sup>142</sup> mediated by gluons. Quantum Chromodynamics is the QFT which describes the  
<sup>143</sup> interactions of quarks and gluons via  $SU(3)_C$  symmetry. QCD contains features  
<sup>144</sup> not present in Electroweak Interactions due to  $SU(3)_C$  generators not commuting  
<sup>145</sup> (a.k.a.  $SU(3)_C$  is a non-abelian group). For example, in QCD there is color  
<sup>146</sup> confinement and asymptotic freedom due to the structure constants being non-  
<sup>147</sup> zero. Requiring  $SU(3)_C$  local gauge invariance implies:

$$\psi(x) \rightarrow \psi(x)' = \exp[i g_S \alpha(x) \cdot \hat{T}] \psi(x) \quad (1.34)$$

<sup>148</sup> where  $\alpha(x)$  is the local phase function,  $g_S$  is the strong coupling constant, and  
<sup>149</sup>  $\hat{T}$  are the eight generators of  $SU(3)$  (note  $\hat{T}^a = \frac{1}{2}\lambda^a a$ , where  $\lambda^a$  are the Gell-Mann  
<sup>150</sup> matrices). As the Gell-Mann matrices are 3x3, this means  $\psi$  has three degrees of  
<sup>151</sup> freedom under these  $SU(3)$  rotations. So we represent  $\psi$  under  $SU(3)$  rotations  
<sup>152</sup> as:

$$\psi = \begin{pmatrix} \psi_{red} \\ \psi_{green} \\ \psi_{blue} \end{pmatrix} \quad (1.35)$$

<sup>153</sup> Consequently, particle fields transforming under  $SU(3)$  rotations have three  
<sup>154</sup> components which physicists describe as color components (red, green, and blue).  
<sup>155</sup> A particle's corresponding antiparticle has the corresponding anticolor. This color  
<sup>156</sup> is the "charge" of QCD and is conserved under  $SU(3)$  rotations. Combining colors,  
<sup>157</sup> color neutral states (e.g. red and antired, or red, green and blue) may be created.  
<sup>158</sup> For the Free Dirac Lagrangian to remain invariant under  $SU(3)$  transformations,  
<sup>159</sup> we must again postulate a boson field that modifies the derivative. The gluon

<sub>160</sub> field tensor is given by ( $\alpha = 1, \dots, 8$ ):

$$G_{\mu\nu}^k = \partial^\mu G_\alpha^\nu - \partial^\nu G_\alpha^\mu - g_S f^{\alpha\beta\gamma} G_\beta^\mu G_\gamma^\nu \quad (1.36)$$

<sub>161</sub> Here  $f^{\alpha\beta\gamma}$  are the structure constants of  $SU(3)$ . Combining all this gives the  
<sub>162</sub> QCD Lagrangian:

$$\mathcal{L}_{QCD} = \bar{\psi}_q i\gamma^\mu (D_\mu)_{ij} \psi^{qj} - m \bar{\psi}^{qi} \psi_{qi} - \frac{1}{4} G_{\mu\nu}^\alpha G^{\alpha\mu\nu} \quad (1.37)$$

<sub>163</sub> Here  $i$  are the color indices, and  $q$  are the quark flavors. It is important to  
<sub>164</sub> note that quarks transform under the fundamental representation of  $SU(3)$ , while  
<sub>165</sub> gluons transform under the adjoint representation. This means quarks carry a  
<sub>166</sub> single color charge (red, green, blue, antired, antigreen, antiblue) and gluons carry  
<sub>167</sub> a color and anticolor charge.

<sub>168</sub> Figure 1.3 shows the three dominant QCD interactions. Since gluons carry  
<sub>169</sub> color charge, they interact with one another. This does not occur in QED, as pho-  
<sub>170</sub> tons do not have electric charge and therefore do not interact with each other.  
<sub>171</sub> In QED, a bare electron's effective charge is largest closest to the electron and  
<sub>172</sub> decreases as a function of distance. This is because the QED vacuum fills with  
<sub>173</sub> particle antiparticle pairs spontaneously, which screen the charge of the bare elec-  
<sub>174</sub> tron. The larger the distance from the electron, the smaller the effective charge  
<sub>175</sub> and therefore the weaker the force. So for a pair of electrons, as the distance  
<sub>176</sub> between them increases the repulsive force decreases and they may be observed  
<sub>177</sub> separately.

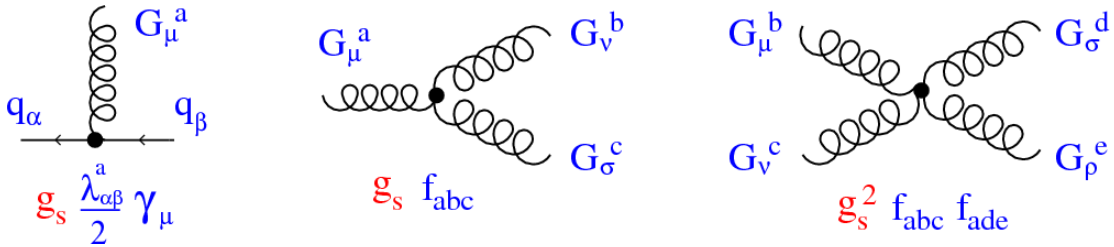


**Figure 1.3:** This figure shows the three dominant QCD interactions. From Ref. [14]

178        Bare quarks and gluons have not been observed. These particles have not  
 179        been directly observed as they have not been found in isolation. Quarks and  
 180        gluons group together to form color neutral objects, like baryons and mesons ( $qqq$   
 181        and  $q\bar{q}$ , respectively). This is because gluons have color charge and interact with  
 182        each other. As the distance from a quark increases it's effective color charge  
 183        increases due to the vacuum polarization in QCD. Color charge grows as the  
 184        distance from the source increases (a.k.a. color is anti-screened in QCD). A quark's  
 185        color charge increases with distance, so strong interactions become stronger at  
 186        large distances (low momenta interactions). At small distances (large momenta  
 187        interactions) strong interactions are significantly weaker and considered nearly  
 188        free. This effect of referred to as asymptotic freedom. At large distances, a  
 189        quark's effective charge is large and the strong force is more significant. This force  
 190        becomes so strong that quarks form colorless bound states instead of remaining  
 191        free particles. This effect is known as color confinement. This running of all SM  
 192        fields is shown in Figure 1.4.

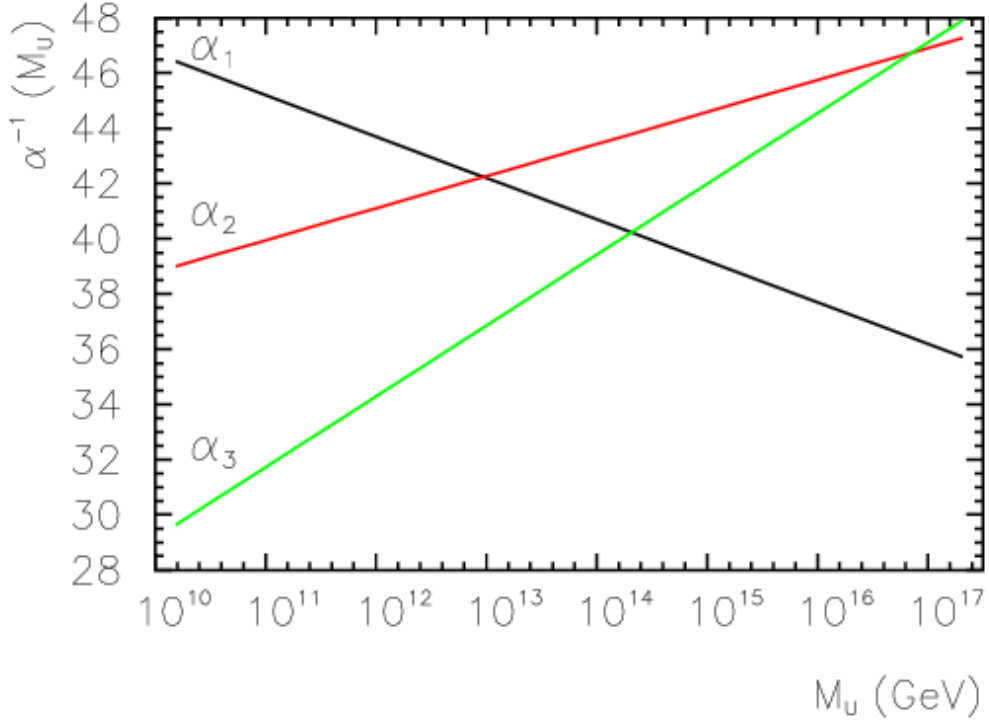


**Figure 1.4:** Strength of the U(1), SU(2), and SU(3) gauge couplings as a function of the energy scale of the interaction ( $Q$ ). From Ref. [10]

Commonly the change in a particle's effective charge under a given force is quantified with  $\beta(r) \equiv -\frac{de(r)}{d\ln r}$ , where  $e(r)$  is the effective charge of a given particle under a force. In QED this function is positive but in QCD this function is negative leading to confinement and asymptotic freedom. Moreover, one can calculate how the coupling ( $\alpha$ ) of a force varies with energies. (More deeply this amounts to incorporating renormalization and vacuum polarization in the boson propagators). For QCD this is:

$$\alpha_S(x) = \frac{\alpha_S(\mu^2)}{1 + \beta_0 \alpha_S(\mu^2) \ln(Q^2/\mu^2)} \quad (1.38)$$

200

$$\beta_0 = \frac{11N_c - 2n_f}{12\pi} \quad (1.39)$$

201 where  $Q$  is the momentum of the force is probed at,  $\mu^2$  is the renormalization scale.

203 As stated previously, quarks and gluons have not been observed in isolation.  
 204 Instead they form bound colorless states. Hadronization is the process by which  
 205 quarks and gluons form hadrons. The process of hadronization is still an active  
 206 area of research. One qualitative description is shown in Figure BLAH. In this  
 207 figure, as two quarks separate the color field between them is restricted to a tube  
 208 with energy density of  $1\text{GeV}/\text{fm}$ . As they separate further, the energy in the color  
 209 field increases, until there is enough energy to produce  $q\bar{q}$  pairs, which breaks the  
 210 color field. This process repeats until quarks and antiquarks have low enough  
 211 energy to form colorless hadrons. The resulting spray of hadrons is called a jet.

212 Since quarks and gluons carry different color charges, their respective jets have  
 213 different properties. As quarks carry only a single color charge (vs. gluons which  
 214 have color and anticolor charge), so their jets have less constituent particles. More  
 215 precisely, the Altarelli-Parisi splitting functions [3] contain a factor  $C_A$  for gluon  
 216 radiation off a gluon and  $C_F$  for gluon radiation off a quark ( $C_A/C_F = 9/4$ ). These  
 217 color factors are the prefactor in the Feynman diagrams for these processes [1],  
 218 which leads to gluon jets having more constituents and therefore more tracks than  
 219 quark jets. Gluon jets also tend to have a larger radius with lower momentum  
 220 constituents than quarks. There are many novel techniques to distinguish quarks  
 221 from gluons. For this study the number of charged particles will be focused on.

<sup>222</sup> **Chapter 2**

<sup>223</sup> **Standard Model Successes and  
Limitations**

<sup>225</sup> The Standard Model has consistently described much of reality to an extreme  
<sup>226</sup> degree of accuracy. It has predicted cross sections for strong and electroweak pro-  
<sup>227</sup> cesses that span over ten order of magnitude correctly [see Fig. 2.1] and contains  
<sup>228</sup> no known logical inconsistencies. Despite the strength and reality of the Stan-  
<sup>229</sup> dard Model, it still fails to describe aspects of reality and suffers from aesthetic  
<sup>230</sup> issues. To date, dark matter and energy comprise 95% of the universe, but are  
<sup>231</sup> not accounted for in the SM. Additionally, neutrinos are known to have mass but  
<sup>232</sup> are massless in the SM. There are mechanisms for introducing massive neutrinos  
<sup>233</sup> in the SM, but these mechanisms create hierarchy problems.

<sup>234</sup> Possibly the most significant aesthetic issue is the hierarchy between the elec-  
<sup>235</sup> troweak and Planck scales. The electroweak scale is the scale of electroweak  
<sup>236</sup> symmetry breaking. The Planck scale is the scale where the gravitational force  
<sup>237</sup> is comparable in strength to the other forces. (This is also the scale where the  
<sup>238</sup> gravitational potential energy of two objects separated by a distance  $r$  is equal to  
<sup>239</sup> the energy of a photon with a wavelength  $r$ .) The Planck scale is where the SM

240 breaks down, as there is not an experimentally verified theory of quantum gravity,  
241 and at this scale gravity cannot be ignored (like it can at the electro-weak scale).  
242 These scales differ by  $\sim 30$  orders of magnitude. Understanding this difference in  
243 scales would not only explain the weakness of gravity at electroweak scales, but  
244 also hopefully lead to a QFT for gravity. (NB: This hierarchy can also be framed  
245 in terms of the corrections to the Higgs mass, which depend on the UV cutoff  
246 scale - where the SM is suppose to break, which is taken at the Planck scale. This  
247 leads the quantum corrections to the Higgs mass to force the Higgs mass to  $10^{18}$   
248 TeV.)

249 These stark contrasts in scales may indicate that a more fundamental theory  
250 exists. It is hoped that such a theory would explain and motivate some of the ad-  
251 hoc features of the SM. In particular, there currently are no experimentally verified  
252 explanations of why there are three generations of fermions, the values of the 19  
253 SM parameters (6 quark masses, 3 charged lepton masses, 3 gauge couplings,  
254 Higgs parameters ( $\mu^2, \lambda$ )), the structure of the fermion representations, etc.

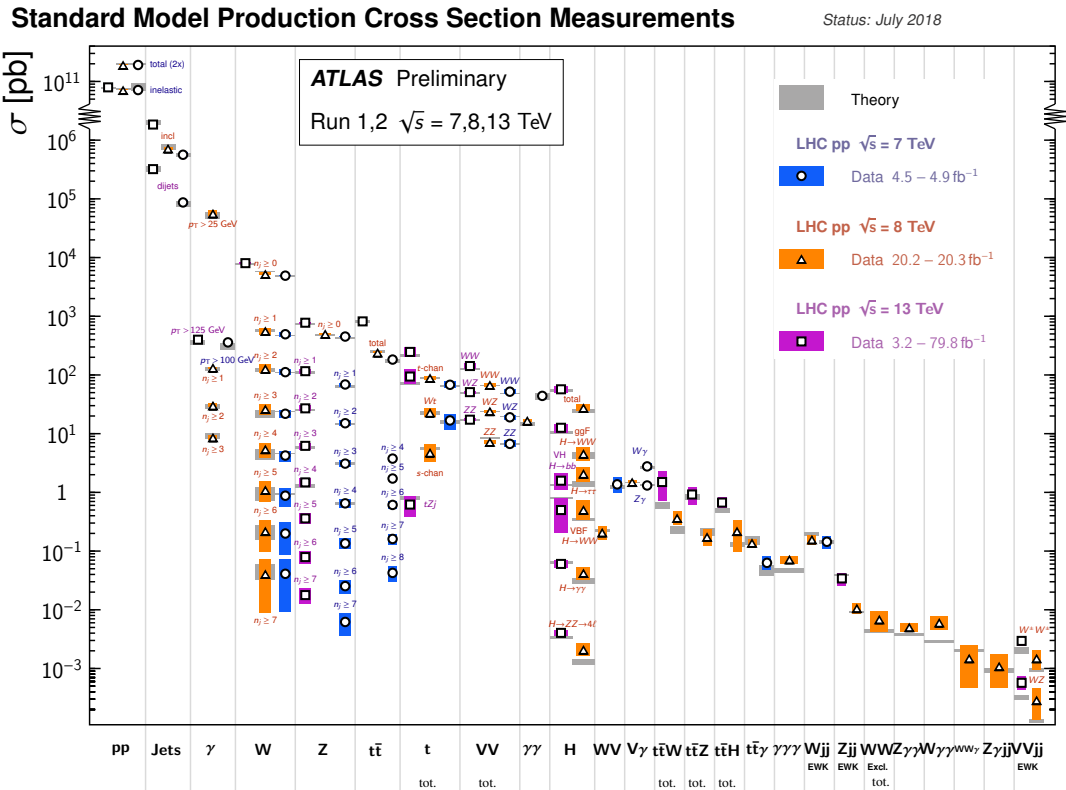


**Figure 2.1:** A comparison of cross section measurements at  $\sqrt{s} = 7,8,13$  TeV from ATLAS compared to theoretical measurements. From Ref. [5]

255 **Chapter 3**

256 **New Physics Models with  
257 Diboson Resonances**

258 **3.1 Randall Sundrum Bulk Model**

259 The electroweak-planck hierarchy may be explained by the existence of extra  
260 dimensions, like the 5D Randall Sundrum Bulk Model ([15], [2]). In this model,  
261 there is one extra warped spatial dimension,  $y$ , with a metric:

$$ds^2 = e^{-2k|y|} \eta_{\mu\nu} dx^\mu dx^\nu + dy^2 \quad (3.1)$$

262 where  $e^{-k|y|}$  is the warp factor of the extra dimension, which is compactified on  
263 a  $S^1/Z_2$  orbifold (a.k.a. a circle where  $y \rightarrow -y$ ). This can be visualized as every  
264 point in space time having a line extending from it a distance  $L$ , representing  
265 this fifth dimension. At the end of this line is the Planck brane. This fourth  
266 spatial dimension separates two 4-D branes: Planck brane and TeV brane. We  
267 live on the TeV brane, as shown in Figure 3.1. The Higgs field (and to a lesser  
268 degree the top quark and graviton fields) is localized near the TeV Brane, while

269 the light fermion fields are localized more near the Planck brane. Fundamental  
 270 parameters are set on the Planck brane. The warp factor may be scaled away from  
 271 all dimensionless SM terms by field redefinitions. However, the only dimensionful  
 272 parameter,  $m_H^2 = v^2$  is rescaled by  $\tilde{v} \sim e^{-kL} M_{Pl} \sim 1\text{TeV}$  for  $kL \sim 35$ , explaining  
 273 why gravity is so weak on the TeV brane. Also, by localizing the light fermion  
 274 fields near the Planck brane and top and graviton fields near the TeV brane, the  
 275 light quarks will have smaller masses.

276 The two free parameters of this theory are  $M_{Pl}$  and  $k$ . Based on this RS Bulk  
 277 model, all SM particles should have Kaluza-Klein (KK) excitations. In particular,  
 278 the graviton would have KK excitations that prefer to decay to WW or ZZ, which  
 279 is why this analysis searches for RS Gravitons.

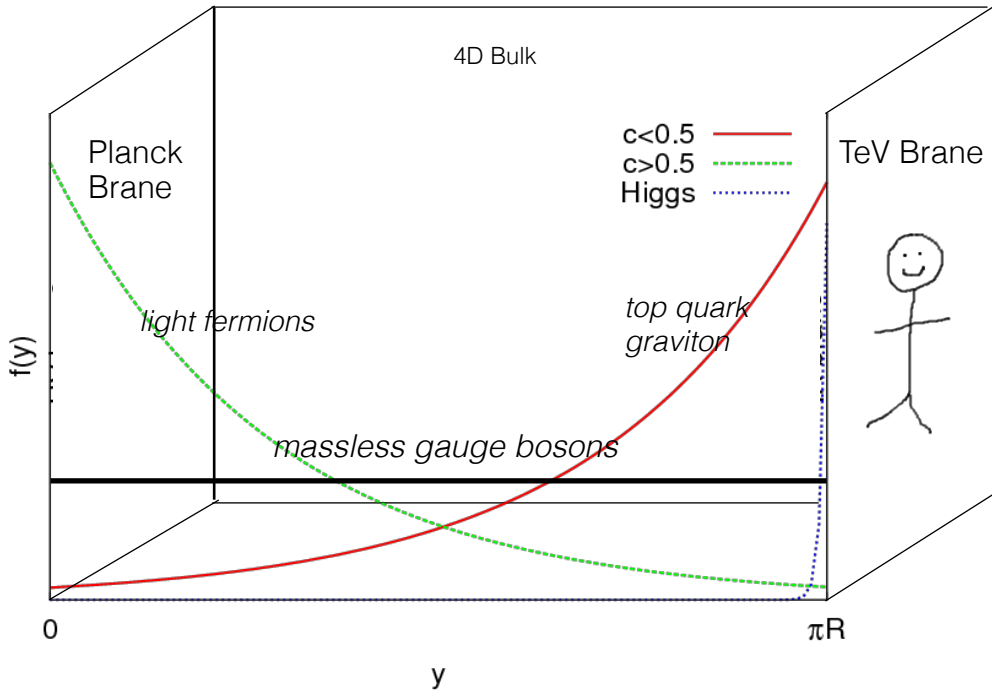


**Figure 3.1:** Cartoon of RS Bulk Model

## 280 3.2 Extended Scalar Sector

281 A further striking asymmetry of the SM is the simplicity of the scalar sector in  
282 comparison to the boson and fermion sectors. To date, the scalar sector has only  
283 one member, the Higgs boson. Therefore, it is natural to posit an extension to the  
284 scalar sector. From a theoretical standpoint this could also help generate baryon  
285 asymmetry through additional sources of CP violation. This analysis searches for  
286 a simple extension to the scalar sector as proposed in Ref. [16]. The extended  
287 scalar sector includes a real Higgs singlet ( $S$ ) and complex  $SU(2)_L$  doublet ( $\Phi$ )  
288 (the SM Higgs), where mass eigenstates are mixtures of the fields.  $S$  has a vev of  
289  $v$  and  $\Phi$  has a vev of  $x$ . This then gives a Lagrangian of:

$$\mathcal{L} \supset (D^\mu \Phi)^\dagger D_\mu \Phi + \partial^\mu S \partial_\mu S - m^2 \Phi^\dagger \Phi - \mu^2 S^2 + \lambda_1 (\Phi^\dagger \Phi)^2 + \lambda_2 S^4 + \lambda_3 \Phi^\dagger \Phi S^2 \quad (3.2)$$

290 The mass eigenstates of the scalar sector are then mixtures of  $S$  and  $\Phi$  and  
291 the free parameters of the theory are  $m_H$ ,  $\sin\alpha$ , and  $\tan\beta = v/x$ . The fields are  
292 then given by:

$$\Phi \equiv \begin{pmatrix} 0 \\ \frac{\tilde{h}+v}{\sqrt{2}} \end{pmatrix} \quad (3.3)$$

$$S \equiv \frac{h' + x}{\sqrt{2}} \quad (3.4)$$

294 Diagonalizing the mass matrix leads to the mass eigenstates  $h$  (discovered  
295 Higgs boson) and  $H$  (the physical particles):

$$\begin{pmatrix} h \\ H \end{pmatrix} = \begin{pmatrix} \cos\alpha & -\sin\alpha \\ \sin\alpha & \cos\alpha \end{pmatrix} \quad (3.5)$$

<sup>296</sup> This suppressed h and H production and SM H couplings:

$$BR_{H \rightarrow SM} = \sin^2 \alpha \times \frac{\Gamma_{SM, H \rightarrow SM}}{\Gamma_{tot}} \quad (3.6)$$

<sup>297</sup> Moreover, in the case that  $m_H > m_h$ ,  $H \rightarrow hh$  is possible. This further suppresses  
<sup>298</sup>  $H \rightarrow VV/ff$ . This search is most sensitive to  $H \rightarrow WW$ .

### <sup>299</sup> 3.3 Simple Standard Model Extensions

<sup>300</sup> The RS Bulk model is motivated by resolving the hierarchy problem. Extending the Scalar sector is a natural space to look for new physics due to the complexity of fermion and boson groups. There are many other interesting and well motivated frameworks, but there is a lack of completely predictive models, due to model flexibility (free parameters). Therefore it is hard for experimentalists to know which theories to search for in data. However, as seen in 3[13], a "Simplified Model" approach may be taken. In the search for reasonably narrow width particles, as in this search, the search is not sensitive to all the details and free parameters of the theory. Generally such searches are only sensitive to the resonance mass and its interactions. Therefore, a theory's Lagrangian may be reduced to only retain this information (mass parameters and couplings). Experimental results using this framework may then be reinterpreted in a given theory.

<sup>312</sup> In the simplified approach, a real vector field is represented under  $SU(2)_L$  with vanishing hypercharge. This results in two charged and one neutral bosons.  
<sup>314</sup> Defined as:

$$V^\pm = \frac{V_\mu^1 \mp iV_\mu^2}{\sqrt{2}} \quad (3.7)$$

<sup>315</sup>  $V_\mu^0 = V_\mu^3 \quad (3.8)$

<sup>316</sup> The Lagrangian is then:

$$\mathcal{L} \supset -\frac{1}{4}D_{[\mu}V_{\nu]}^a D^{[\mu}V^{\nu]}_a + \frac{m_V^2}{2}V_\mu^a V^{a\mu} + ig_V c_H V_\mu^a H^\dagger \tau^a \overset{\leftrightarrow}{D}^\mu H + \frac{g^2}{g_V} c_F V_\mu^a J_F^{\mu a} \quad (3.9)$$

<sup>317</sup> In order the terms represent: the kinetic,  $V$  mass, Higgs- $V$  interaction, and  
<sup>318</sup>  $V$ -left-handed fermion interaction terms. Phenomenologically the three physical  
<sup>319</sup> particles this predicts are degenerate, where  $V$  couples most strongly to  $VV$ , via  
<sup>320</sup> the  $g_V$  coupling factor. The dominant production modes are DY and VBF.

<sup>321</sup> Two versions of HVT are considered, Model A and B. Model A is a weakly  
<sup>322</sup> coupled model where  $g_V \ll 1$ , like the extended gauge symmetry discussed in Ref .  
<sup>323</sup> [16]. Model B is a strongly coupled model, where  $1 < g_V < 4\pi$ . The width of the  
<sup>324</sup> resonance grows with  $g_V$  so for this narrow resonance search only  $g_V$  is chosen to  
<sup>325</sup> be less than 6 (so  $\Gamma/M < 10\%$ ). More precisely, the coupling of these resonances  
<sup>326</sup> to fermions scales as  $g_f = g^2 c_F/g_V$ , where  $g$  is the SM  $SU(2)_L$  gauge coupling  
<sup>327</sup> and  $c_F$  is the free parameter (expected to be of order 1 for Model A and B). This  
<sup>328</sup> then means that for Model B the coupling is to fermions is more suppressed than  
<sup>329</sup> for Model A, leading to a smaller DY production rate and BR to fermionic final  
<sup>330</sup> states. The coupling of  $V$  to SM bosons scales as  $g_H = g_V c_H$ , where  $c_H$  is a  
<sup>331</sup> free parameter on the order of 1 for Model A and B. So for small values of  $g_V$   
<sup>332</sup> (i.e. Model A - weakly coupled theories) the BR to gauge boson is smaller than  
<sup>333</sup> for Model B. So weakly coupled vectors have large production cross sections and  
<sup>334</sup> decay predominantly to leptons or jets, while strongly coupled vectors are produced  
<sup>335</sup> less and decay predominantly to gauge bosons.

<sup>336</sup> Vectors in Model A and B are generally produced via quark-anti-quark annihi-  
<sup>337</sup> lation. The more rare production via vector-boson-fusion is considered by setting  
<sup>338</sup>  $g_H = 1$  and  $g_F = 0$ . In Model B diboson final states are enhanced as stated  
<sup>339</sup> previously due to  $g_H$  and moreover the BR to WZ, WH, WW, and ZH are the

<sup>340</sup> same.

<sup>341</sup> In summary,  $V$  couples most strongly to left-handed fermions and  $VV$  dependent on  $g_V$ .

## Part II

343

## Experimental Setup

344

<sup>345</sup> **Chapter 4**

<sup>346</sup> **LHC**

<sup>347</sup> The Large Hadron Collider (LHC) is the highest-energy particle collider in the  
<sup>348</sup> world. It was designed to expand the frontier of high energy particle collisions in  
<sup>349</sup> energy and luminosity. This enables LHC experiments to test the Standard Model  
<sup>350</sup> and search for new physics at higher energies than tested with previous colliders.  
<sup>351</sup> Collisions at higher energies not only produce more massive particles but also  
<sup>352</sup> more weakly interacting particles. Fig. 4.1 shows production cross sections for  
<sup>353</sup> various processes at hadron colliders. The rate for electroweak physics pcoesses  
<sup>354</sup> including  $W$  and  $Z$  scale with the center-of-momentum energy,  $\sqrt{s}$ .

<sup>355</sup> The LHC consists of a 26.7 km (17 miles) ring, approximately 100 m un-  
<sup>356</sup> derground, outside Geneva, Switzerland. Counter-circulating proton (and occa-  
<sup>357</sup> sionally heavy ions) beams collide inside four experiments along the beam line:  
<sup>358</sup> ATLAS, CMS, LHCb, ALICE. ATLAS and CMS are general purpose detectors  
<sup>359</sup> designed to explore high energy frontier. LHCb is designed to study the physics  
<sup>360</sup> of  $b$ -quarks. ALICE specializes in studying heavy ion collisions.

## proton - (anti)proton cross sections

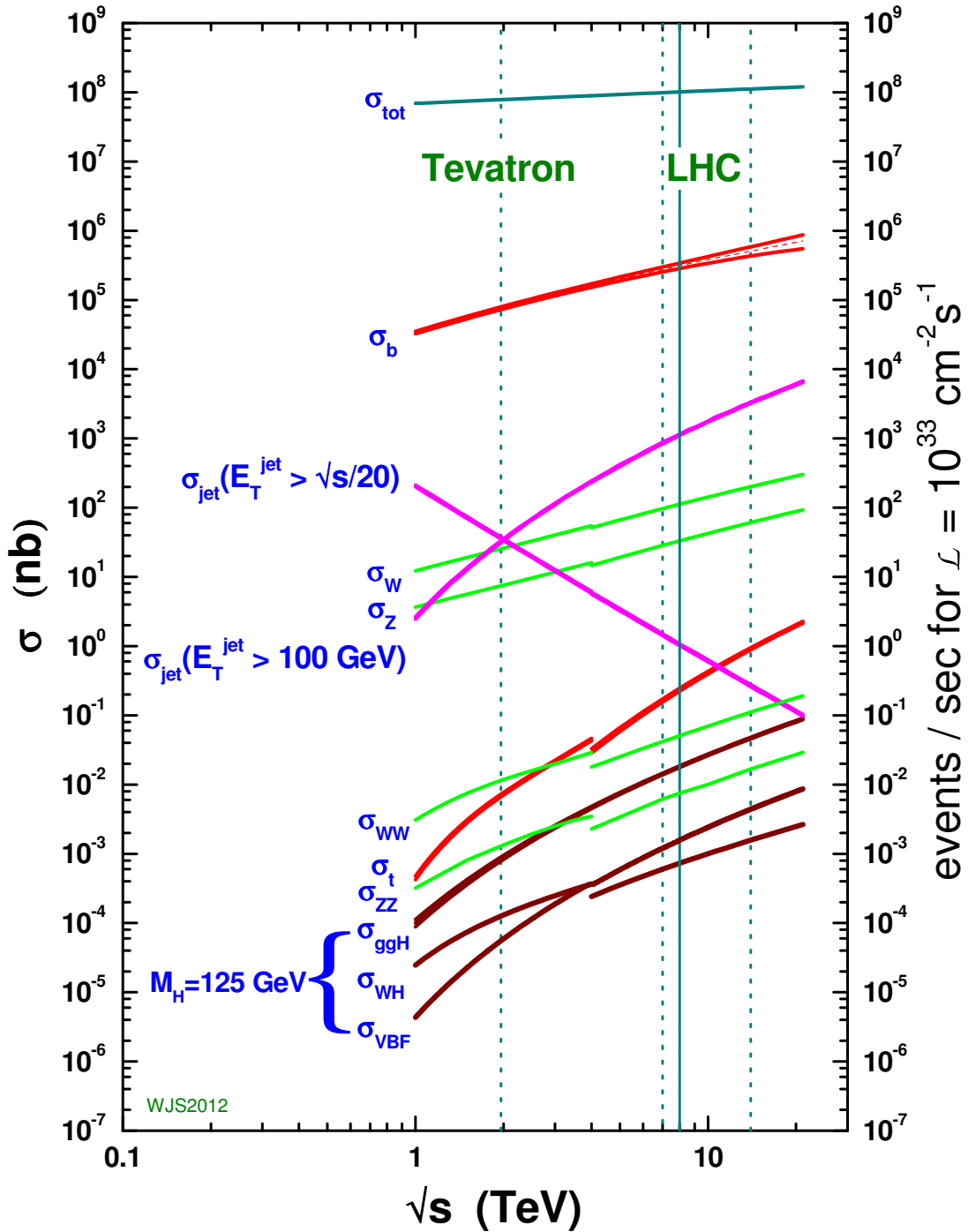
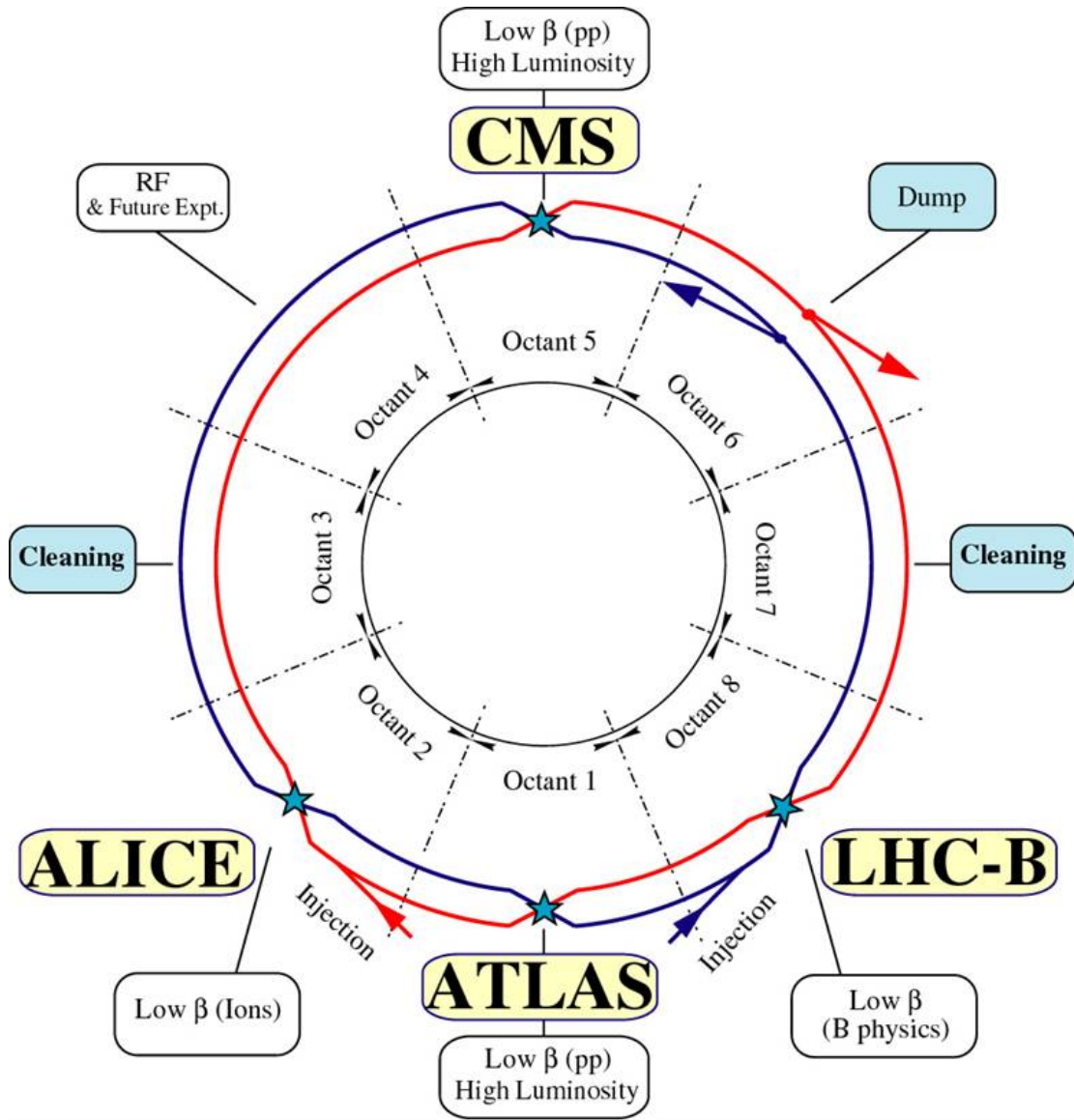


Figure 4.1: Scaling of cross sections with  $\sqrt{s}$ . Natasha: write more here

361        The first proton beams circulated in September, 2008. Nine days later an  
362 electrical fault lead to mechanical damage and liquid helium leaks in the collider.  
363 This incident delayed further operation until November 2009, when the LHC be-  
364 came the world's highest energy particle collider, at 1.18TeV per beam. This first  
365 operational run continued until 2013, reaching 7 and 8 TeV collision energies. Dur-  
366 ing this run a particle who's properties were consistent with the Standard Model  
367 Higgs boson was discovered. The next operational began after a two year shut-  
368 down after upgrades to the LHC and experiments. This run lasted from 2013 to  
369 2018 reaching 13 TeV collision energies. This analysis uses data from the second  
370 operational run.

## 371 **4.1 LHC Layout and Design**

372        The layout of the LHC is shown in Figure 4.2. The red and blue lines in the  
373 figure represent the counter-circulating proton beams. The LHC is divided into  
374 eight octants. Octant 4 contains the RF cavities that accelerate the protons and  
375 octant 6 contains the beam dump system. Octants 3 and 7 house the collimation  
376 systems for beam cleaning. The beams collide inside the four aforementioned  
377 experiments. Each octant contains a curved and straight section. The LHC  
378 magnets are built with NbTi superconductors cooled with super-fluid Helium to  
379 2K, creating a 8.3T magnetic field to bend the proton beams.

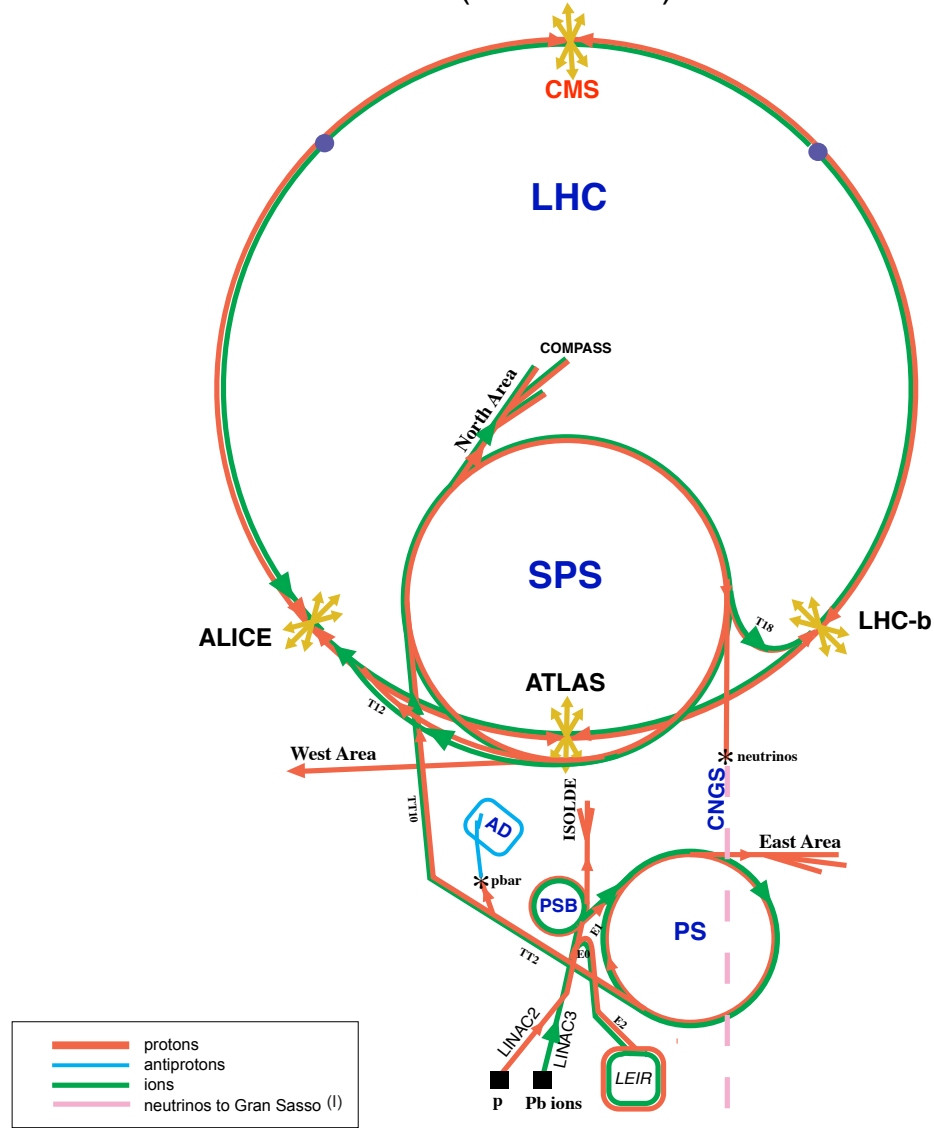


**Figure 4.2:** LHC Layout. Natasha write more

380        Four sequential particle accelerators are used to accelerate proton from rest as  
 381        shown in Figure 4.3. First, Hydrogen gas is ionized to produce protons which  
 382        are then accelerated to 50 MeV using Linac 2, a linear accelerator. The result-  
 383        ing proton beam is then passed to three circular particle accelerators: Proton  
 384        Synchrotron Booster, Proton Synchrotron, and Super Proton Synchrotron (SPS),

385 accelerating protons to 1.4, 25, and 450 GeV, respectively. Once the protons exit  
386 SPS, they are injected into the LHC at octant 2 and 8. Each proton bunch contains  
387  $10^{11}$  protons. The spacing between bunches is 25 ns, which means each beam con-  
388 tains 3564 bunches. However, some bunches are left empty due to injection and  
389 safety requirements, yield 2808 bunches per beam. Once the proton beams are  
390 injected they are accelerated to 13 TeV.

## CERN Accelerators (not to scale)



LHC: Large Hadron Collider

SPS: Super Proton Synchrotron

AD: Antiproton Decelerator

ISOLDE: Isotope Separator OnLine DEvice

PSB: Proton Synchrotron Booster

PS: Proton Synchrotron

LINAC: LINear ACcelerator

LEIR: Low Energy Ion Ring

CNGS: Cern Neutrinos to Gran Sasso

Rudolf LEY, PS Division, CERN, 02.09.96  
Revised and adapted by Antonella Del Rosso, ETT Div.,  
in collaboration with B. Desforges, SL Div., and  
D. Manglunki, PS Div. CERN, 23.05.01

**Figure 4.3:** LHC Accelerator. Natasha write more

391 As many new physics models predict cross-sections below the weak scale it was  
392 important to design the LHC to be capable of collecting enough data, by running  
393 in high luminosity conditions. The machine luminosity depends only on beam  
394 parameters:

$$L = \frac{N_p^2 f}{4\epsilon\beta^*} F \quad (4.1)$$

395 where  $N_p$  is the number of protons per bunch,  $f$  is the bunch crossing frequency,  
396  $\epsilon$  is the transverse beam emittance,  $\beta^*$  is the amplitude function at the collision  
397 point, and  $F$  is the geometric luminosity reduction factor due to the beams crossing  
398 at an angle (rather than head-on).

399 This analysis uses data from Run 2, totally 139/fb. The peak luminosity was  
400 [Natasha add info here]. [Natasha add lumi and integrated lumi figures].

401 **Chapter 5**

402 **The ATLAS Detector**

403 The ATLAS detector measures the position, momentum and energy of parti-  
404 cles produced in the proton collisions by using magnetic fields, silicon detectors,  
405 sampling calorimeters, and gaseous wire detectors. It is located approximately  
406 100 m underground at Point-1 around the LHC beam line and weighs 7000 metric  
407 tons. The detector is 46 m long, 25 m high, 25 m wide as shown in Figure 5.2.  
408 The detector can be divided into three subsystems: the Inner Detector (ID), the  
409 Calorimeters, and the Muon Spectrometer (MS). Figure 5.3 shows an overview of  
410 how different particles interact in the detector.

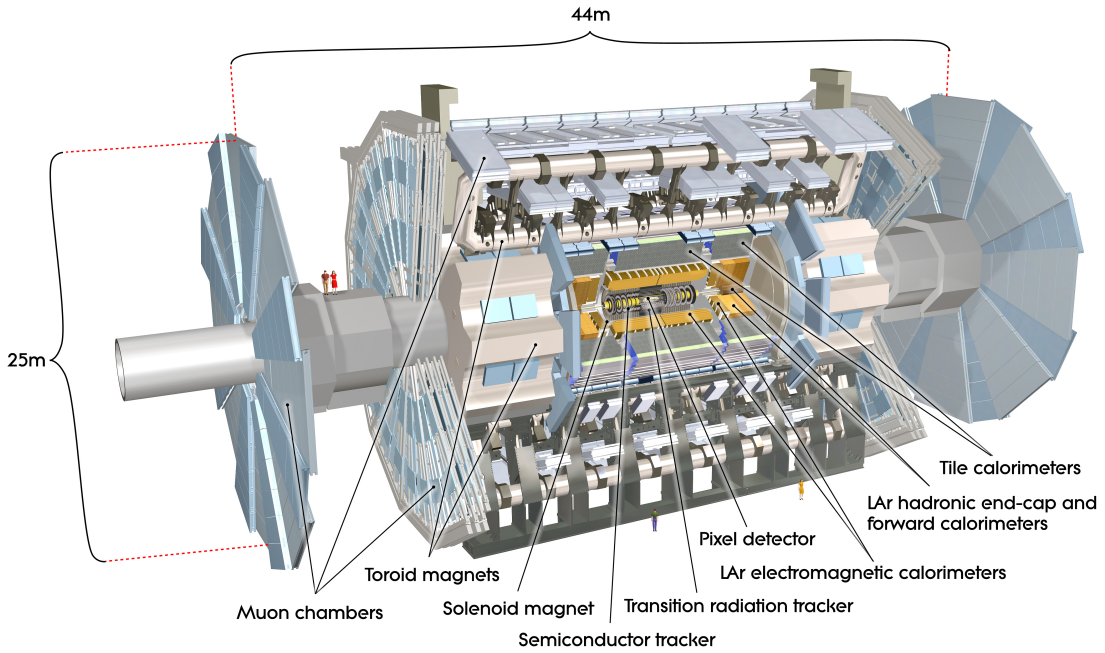


**Figure 5.1:** Big picture layout of ATLAS detector. Natasha: write more

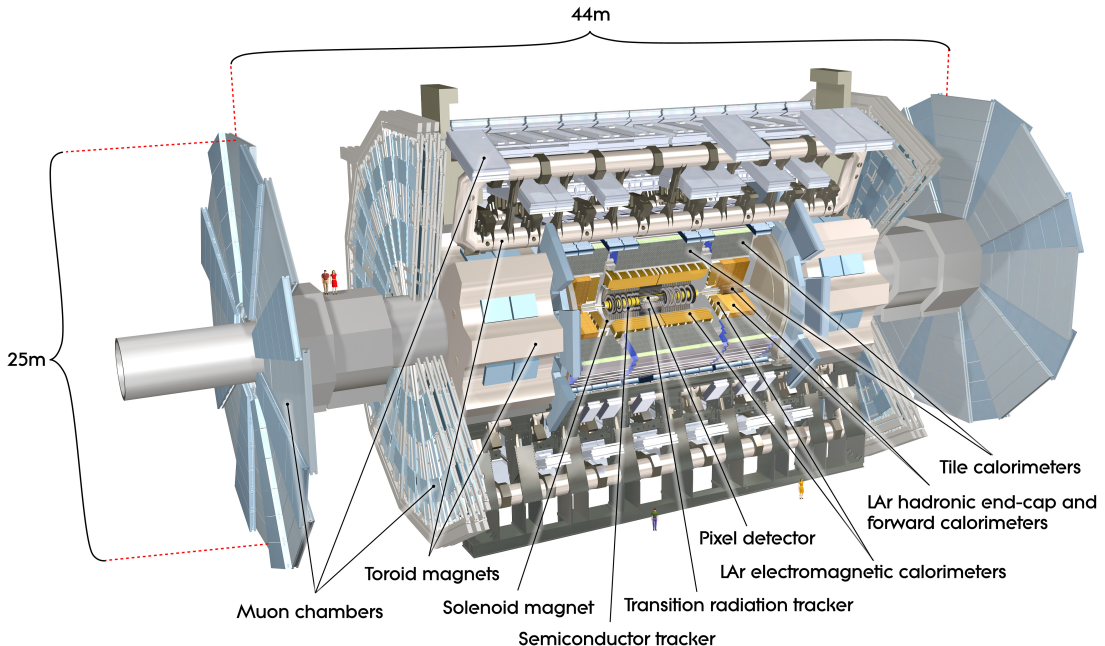


**Figure 5.2:** Big picture layout of ATLAS detector. Natasha: write more

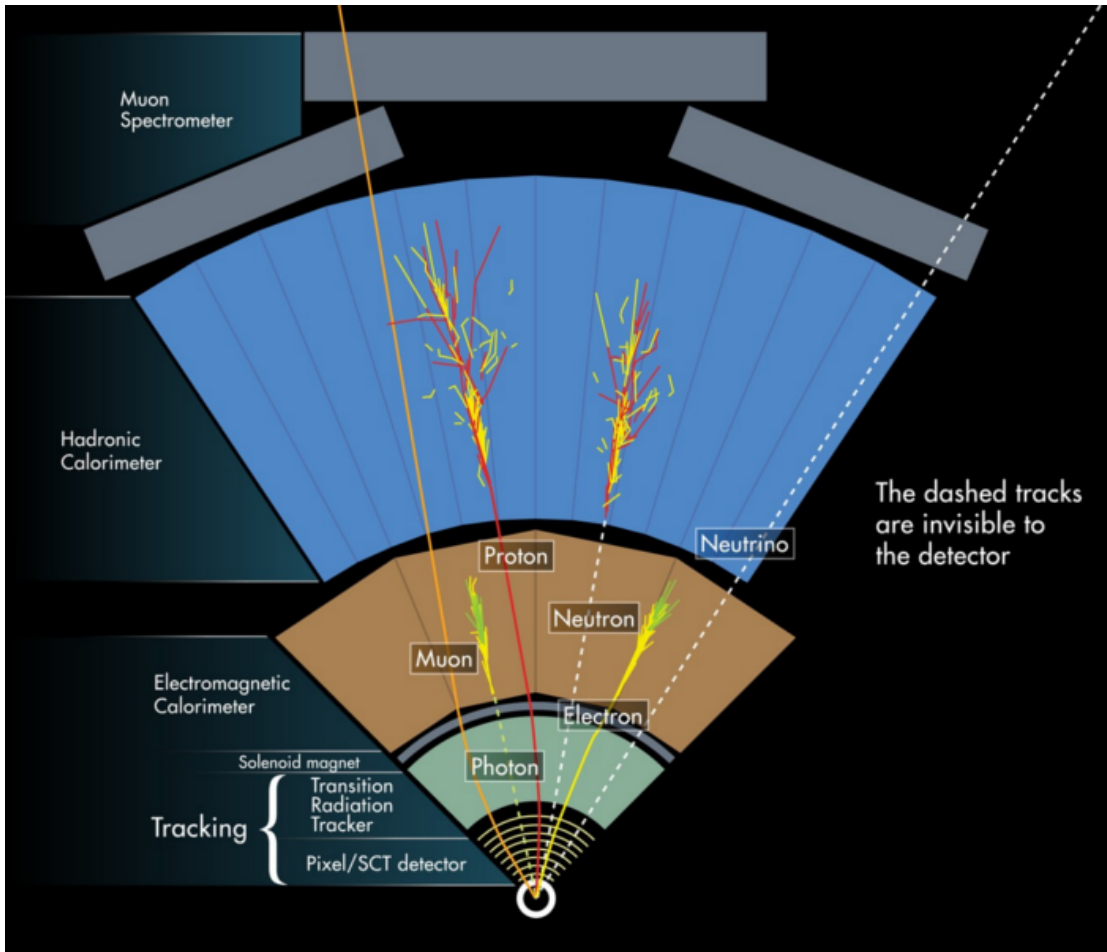


**Figure 5.3:** A simplified schematic of how different particles interact and are detected within ATLAS.

## 411 5.1 Coordinate System

412     The trajectory of particles within ATLAS is measured relative to the nominal  
 413 interaction point. The  $z$ -axis points along the beam line, such that when the  
 414 LHC is viewed from above, the counter-clockwise circulating beam points along  
 415 the positive- $z$  direction. The  $x - y$  plane is transverse to the beam line, with  
 416 the positive  $x$ -axis pointing towards the center of the LHC ring. The positive  
 417  $y$ -axis points vertically upward. The azimuthal angle,  $\phi$ , is the angular distance

about the  $z$ -axis, with  $\phi = 0$  along the  $x$ -axis. The polar angle from the  $z$ -axis is denoted as  $\theta$ . The polar angle is usually replaced by pseudo-rapidity,  $\eta = -\ln \tan(\frac{\theta}{2})$ . Pseudo-rapidity is preferred as  $\Delta\eta$  is invariant under boosts along  $z$  and particle production is approximately invariant under  $\eta$ . Angular separation between particles in ATLAS are given by  $\Delta R = \sqrt{\Delta\eta^2 + \Delta\phi^2}$ . The distance from the beamline is given by  $r = \sqrt{x^2 + y^2}$

## 5.2 Inner Detector

The Inner Detector (ID) was designed to identify and reconstruct vertices, distinguish pions from electrons, and measure the momentum of charged particles. The ID uses three different technologies for particle reconstruction: the Pixel Detector, Semiconductor Tracker (SCT), and the Transition Radiation Tracker (TRT), shown in Figure 5.4 and 5.5. The entire ID is immersed in a 2T solenoidal magnetic field parallel to  $z$ , causing charged particles to bend in the transverse-plane, allowing particle momentum measurements.

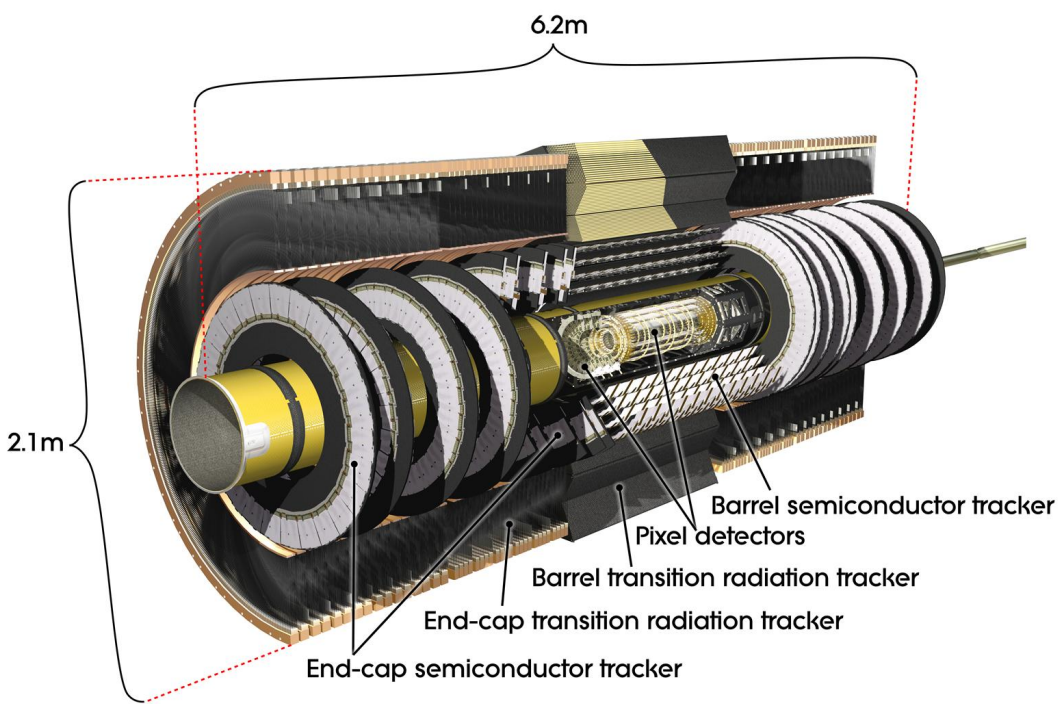


**Figure 5.4:** Layout of ATLAS Inner Detector

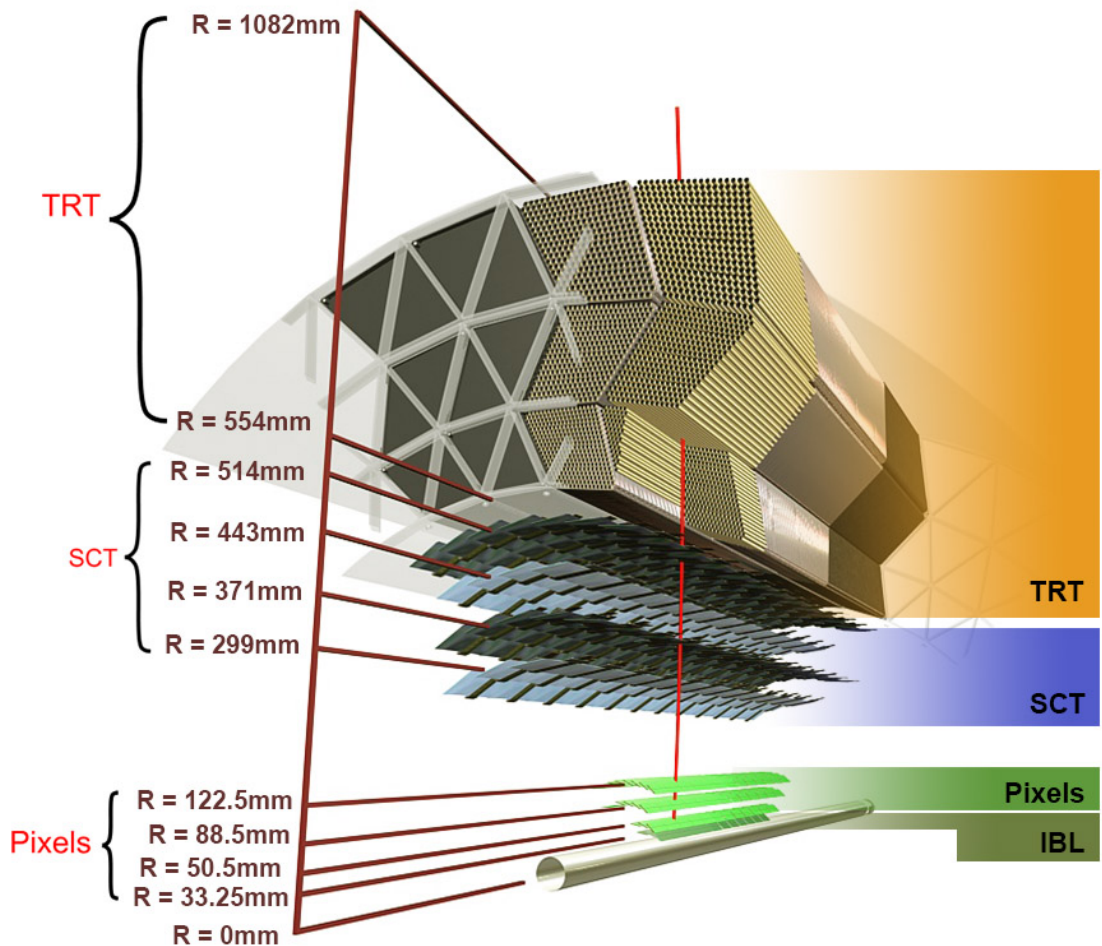


Figure 5.5: Layout of ATLAS ID Barrel System.

432 **5.2.1 Pixel Detector**

433 The pixel detector consists of four barrel layers between  $r = 32.7$  and  $122.5$   
434 mm, extending to  $|z| = 400.5$  mm. The innermost pixel barrel, the Insertable  
435 b-Layer (IBL), only extends to  $|z| = 332$  mm. The pixel detectors closer to the  
436 beam line (larger  $\eta$  values) consists of six parallel cylindrical rings of pixel de-  
437 tectors transverse to the beam line. The entire pixel detector consists of 1744  
438 identical pixel sensors each with 46080 readout channels, totaling about 80 mil-  
439 lion individual pixels. Most of the pixel sensors are  $50 \times 400 \mu\text{m}^2$ . The intrinsic  
440 measurement accuracy of a individual pixel detector in the barrel (end-cap) in  
441  $r - \phi$  is  $10 \mu\text{m}$  and  $115 \mu\text{m}$  in  $z(r)$ .

442 **5.2.2 Semiconductor Tracker**

443 The SCT is located outside the pixel detector and has the same barrel and  
444 endcap geometry as the pixel detector. SCT sensors are  $80 \mu\text{m} \times 12$  cm ( $80 \mu\text{m}$   
445 strip pitch). In the barrel the strips are parallel to the  $z$ -axis and are segmented  
446 in  $\phi$ . In the endcaps, the strips extend radially. Sensors are grouped in modules  
447 containing two layers of strips rotated 40 mrad with respect to each other. This  
448 offset allows for the two-dimensional position of a track to be determined by  
449 identifying the crossing point of the strips that registered a hit. SCT modules  
450 measure tracks with an accuracy of  $17 \mu\text{m}$  in  $r - \phi$  and  $580 \mu\text{m}$  in  $z(r)$  in the  
451 barrel (end-cap) region.

452 **5.2.3 Transition Radiation Tracker**

453 The transition radiation tracker (TRT), enveloping the SCT, is a gaseous  
454 straw-tube tracker mainly used for electron/pion track separation. Each straw  
455 is 4 mm in diameter and filled with a Xe- $\text{CO}_2$ - $\text{O}_2$  gas mixture. An anode wire at

456 the center of the straw is held at ground potential, while the walls of the straw are  
457 kept at -1.4kV. When a charged particle passing through the TRT ionizing the  
458 gaseous mixture, and the resulting ions form an avalanche on the anode wire with  
459 a grain of  $10^4$ . The resulting signal from the anode wire is then digitized and  
460 amplified. Signals passing a low threshold cutoff are used to distinguish noise from  
461 tracks. Signals passing a high threshold cutoff are sensitive to transition radiation  
462 (TR). TR photons are emitted when charged particles pass between materials  
463 with different dielectric constants. The probability that a charged particle with  
464 energy  $E$  and mass  $m$  passing between two materials emits a TR photon in the keV  
465 range is proportional to  $\gamma = E/m$ . In the TRT straws these often then convert via  
466 the photoelectric effect, causing a large avalanche triggering the high-threshold.  
467 Since electrons have a smaller mass than pions, tracks from electrons are more  
468 likely to trigger the high threshold. Consequently, the high threshold TRT trigger  
469 provides electron identification information that is uncorrelated with calorimeter  
470 shower-shape information.

471 The barrel region of the TRT extends from  $r = 563\text{-}1066$  mm and  $|z| < 712$   
472 mm. Barrel Straws are 144 cm long (divided  $\eta \approx 0$ ) and orientated parallel to  
473 the beam direction. End-cap straws extend radially and are 37 cm long. There  
474 are 53,544 straws in the barrel and 160,000 straws in the end-caps. Radiator mats  
475 of polypropylene/polyethylene fibers in the barrel are aligned perpendicular to the  
476 barrel straws (with holes for the straws to pass through). In the end-cap region,  
477 radiator foils are layered between the radial TRT straws.

478 The width of the signal pulse is sensitive to the distance between the charged  
479 particle track and the anode wire and allows for a hit resolution of  $130\mu\text{m}$ . The  
480 TRT extends to  $|\eta| = 2.0$  and provides about 36 hits per track.

481    **5.3 Calorimeters**

482    The ATLAS electromagnetic and hadronic calorimeters (EMC and HCAL,  
483    respectively) absorb and measure the energy of high energy hadrons, photons,  
484    and electrons with  $|\eta| < 4.9$ . Both systems use sampling calorimeters which  
485    consist of alternating layers of dense absorbing and active layers. In the absorbing  
486    layer particles interact and lose energy, creating showers. These showers are then  
487    detected and measured in the active layer. The amount of charge measured in the  
488    active material scales with the energy of the incident particle, and thus provides a  
489    measurement of the particle's energy. An overview of the layout of the calorimeter  
490    system is shown in Figure 5.6.

491    The EMC measures and contains the energy of electromagnetically interacting  
492    particles with 170k channels. It consists of layered accordion-shaped Lead ab-  
493    sorber plates and electrodes immersed in liquid Argon. Using accordion-shaped  
494    electrode and absorbers ensures  $\phi$  symmetry and coverage. The EMC is com-  
495    posed of a barrel part ( $|\eta| < 1.475$ ), two end-caps ( $1.375 < |\eta| < 3.2$ ), and a  
496    presampler ( $|\eta| < 1.8$ ). The presampler, containing only liquid Argon, corrects  
497    for upstream energy losses of electrons and photons. The EMC barrel is segmented  
498    into three layers. The first layer has finest segmentation with readout cells ex-  
499    tending  $\Delta\eta \times \Delta\phi = 0.025/8 \times 0.1$ . This provides a precise shower measurements  
500    used to separate prompt photons from  $\pi^0 \rightarrow \gamma\gamma$  decays. The second layer has  
501    coarser segmentation and is approximately 16 radiation lengths long. A radiation  
502    length is the average distance an electron travels before losing all but  $1/e$  of its  
503    energy to bremsstrahlung. The last layer is the most coarse and measures the tail  
504    of the electromagnetic shower. A schematic of the ECAL is shown in Figure ??.

505    The hadronic calorimeter located outside the EMC and is used to contain  
506    and measure the energy of hadronically interacting particles. It consists of a tile

507 calorimeter (TileCal), hadronic end-cap calorimeter (HEC), and liquid Argon for-  
 508 ward calorimeter (FCAL). TileCal is located behind the LAr EMC and uses steel  
 509 absorbers and liquid Argon as the active material. TileCal consists of three barrel  
 510 layers in the central and forward regions, extending up to  $|\eta| < 1.7$ . Radiated  
 511 photons from the steel tiles are collected via wavelength-shifting fibers connected  
 512 to photomultiplier tubes, as shown in Figure 5.8. The HEC lies behind the EMC  
 513 endcap wheels. It uses copper absorbers and liquid Argon as the active material  
 514 and covers  $1.5 < |\eta| < 3.2$ . Finally, the FCAL covers  $3.1 < |\eta| < 4.9$  and consists  
 515 of three modules all using liquid Argon as the active material. The first module  
 516 uses copper absorber and was designed for electromagnetic measurements. The  
 517 second and third modules consist of tungsten absorber and are used to measure  
 518 the kinematics of hadronically interacting particles. A schematic of the HCAL is  
 519 shown in Figure 5.8.

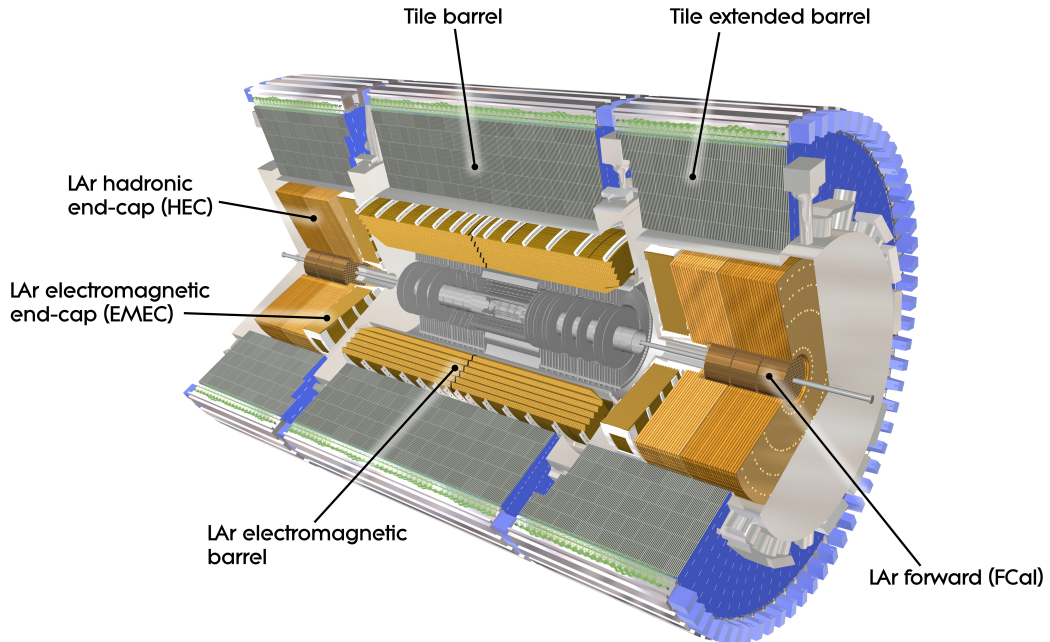


**Figure 5.6:** Overview of ATLAS electromagnetic and hadronic calorimeters.

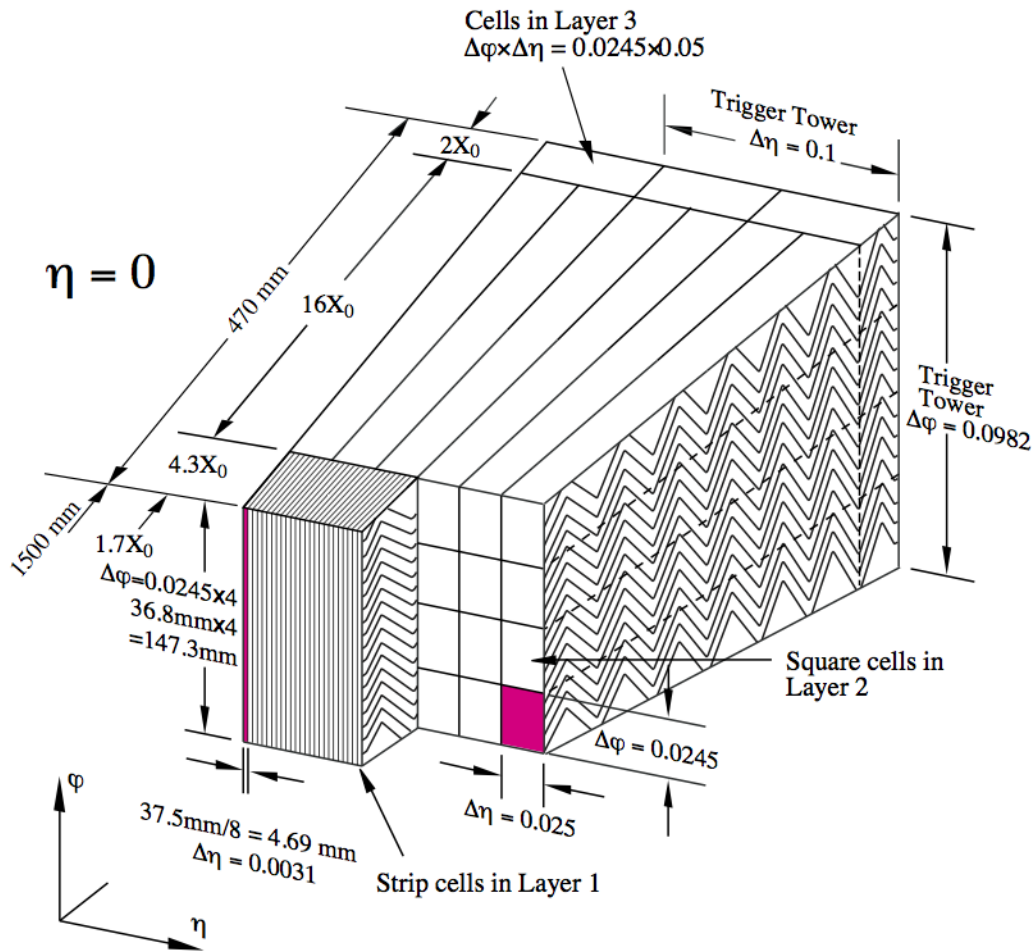


**Figure 5.7:** Schematic of ECAL.

**Figure 5.8:** Schematic of HCAL.

520 The energy resolution of the calorimeter subsystems are:

521 
$$\frac{\sigma_E}{E} = \frac{10\%}{\sqrt{E}} \oplus 0.7\% \text{ EMC}$$

522 
$$\frac{\sigma_E}{E} = \frac{50\%}{\sqrt{E}} \oplus 3\% \text{ hadronic barrel -Natasha check if barrel and end-cap truly}$$

523 have same energy resolution

524 
$$\frac{\sigma_E}{E} = \frac{50\%}{\sqrt{E}} \oplus 3\% \text{ hadronic end-cap}$$

525 
$$\frac{\sigma_E}{E} = \frac{100\%}{\sqrt{E}} \oplus 10\% \text{ hadronic end-cap}$$

526    **5.4 Muon Spectrometer**

527       The muon spectrometer (MS) is the outermost detector system in ATLAS.  
528       Muons with a  $p_T > 4$  GeV are energetic enough to reach the MS. To measure the  
529       momentum of these muons two barrel and end-cap toroid magnets are used covering  
530        $|\eta| < 1.4$  and  $1.6 < |\eta| < 2.7$ . For  $1.4 < |\eta| < 1.6$ , a combination of the barrel  
531       and end-cap toroidal magnetic fields bend muon trajectories. The detector in the  
532       barrel region form three concentric rings at  $R = 5, 7.5, 10$ m and are segmented  
533       in  $\phi$  to accommodate the magnets. The end-cap region consists of three circular  
534       planes perpendicular to  $z$  and located at  $|z| = 7.4, 14, 21.5$ m from the interaction  
535       region. An additional detector at  $|z| = 10.8$ m covers the transition region between  
536       the barrel and end-cap.

537       The MS consists of four subsystems: Monitored Drift Tubes (MDT), Cathode  
538       Strip Chambers (CSC), Resistive Plate Chambers (RPC), and Thin Gap Cham-  
539       bers (TGC). The first two subsystems are used primarily for measuring muon track  
540       parameters, while the RPC and TGC subsystems are used for muon triggering.  
541       A schematic of this system is shown in Figure 5.9.

542       The MDT subsystem consists of precision tracking chambers for  $|\eta| < 2.7$ ,  
543       except for the inner most end-cap layer ( $2.0 < |\eta| < 2.7$ ), where CSCs are used.  
544       The basic unit of MDT chambers are thin walled Aluminum tubes with a diameter  
545       of 3 cm and length of 0.9-6.2 m. These tubes are filled with a mixture of Ar-CO<sub>2</sub>  
546       gas with a 50μm W-Rn wires running down the center of the tube which is kept at  
547       3080 V. Since the maximum drift time of these chambers is 700 ns, they are not  
548       used for triggering. MDT chambers consist of 3-4 layers of tubes mounted on a  
549       rectangular support system, as seen in Figure 5.10, orientated along  $\phi$  to measure  
550       the coordinate in the bending plane of the magnetic field with a resolution of 35  
551       μm.

552        The MDT subsystem can only handle hit rate below  $150\text{Hz}/\text{cm}^2$ . For this  
553 reason, CSCs are used in the innermost end-cap layer where hit rates are larger.  
554 CSCs can handle hit rates up to  $1000\text{Hz}/\text{cm}^2$ . CSC are multiwire proportional  
555 chambers. These chambers are filled with a Ar- $\text{CO}_2$  gas mixture and evenly spaced  
556 wires kept at 1900 V. These wires are orientated in the radial direction but not  
557 read out. Instead on one side of the cathode are copper strips parallel to the wires,  
558 measuring  $\eta$ , while on the other side of the cathode are strips parallel to the wires  
559 measuring  $\phi$ . The width between strips is approximately 1.5 mm providing a  
560 resolution of  $60\ \mu\text{m}$  in the bending-plane and 5 mm in the non-bending plane.

561        Since the CSC and MDT systems do not poor time resolution, the RPC and  
562 TGC systems are used for triggering. The RPC system is used in the barrel region  
563 ( $|\eta| < 1.05$ ). RPC consist of two parallel resistive plates separated by a 2 mm  
564 insulated spacer with 100 mm spacing kept at 9.8 kV 5.11. A gaseous mixture of  
565  $\text{C}_2\text{H}_2\text{F}_4$ ,  $\text{C}_4\text{H}_{10}$ , and  $\text{SF}_6$  fills the space between the two plates. Metallic strips  
566 on the outer faces of the plates are used to read out signals produced by the  
567 gas ionizing. The middle barrel layer consists of two layers of RPCs on either  
568 side of the MDT layer and one layer on the outermost MDT layer. Each layer  
569 contains two orthogonal sets of metallic strips providing  $\eta$  and  $\phi$  measurements.  
570 The timing resolution of RPCs is 1.5 ns, and therefore may be used to identify  
571 bunch crossings.

572        Finally, the TGCs are used in the end-cap regions and primarily used to pro-  
573 vide L1 trigger decisions and  $\phi$  measurements. TGCs are multi-wire proportional  
574 chambers consisting of arrays of gold-coated tungsten wires placed between two  
575 cathode planes. These wires are separated by 1.8 mm and cathodes are 1.4 mm  
576 from the wires. Orthogonal to the wires, on the opposite side of the cathode plane  
577 are copper strips held at 2900 V. The chambers are filled with a mixture of  $\text{CO}_2$

578 and n-pentane gas, the latter acts as a quenching gase to prevent avalances initiated  
579 by secondary  $\gamma$ -rays from the primary avalanche. Figure 5.12 is a schematic  
580 of a TGC. The timing resolution of TGCs is less than 25 ns and therefore are used  
581 for bunch crossing measurements.

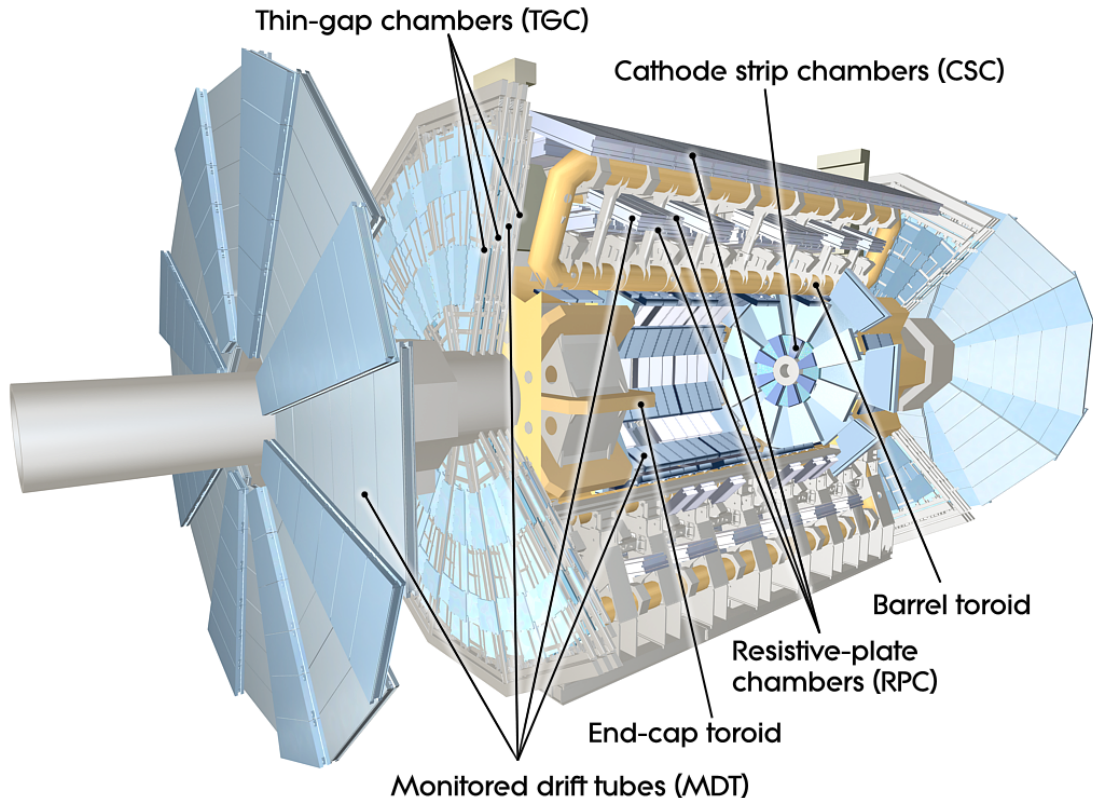


**Figure 5.9:** Schematic of Muon Spectrometer [cite G35]

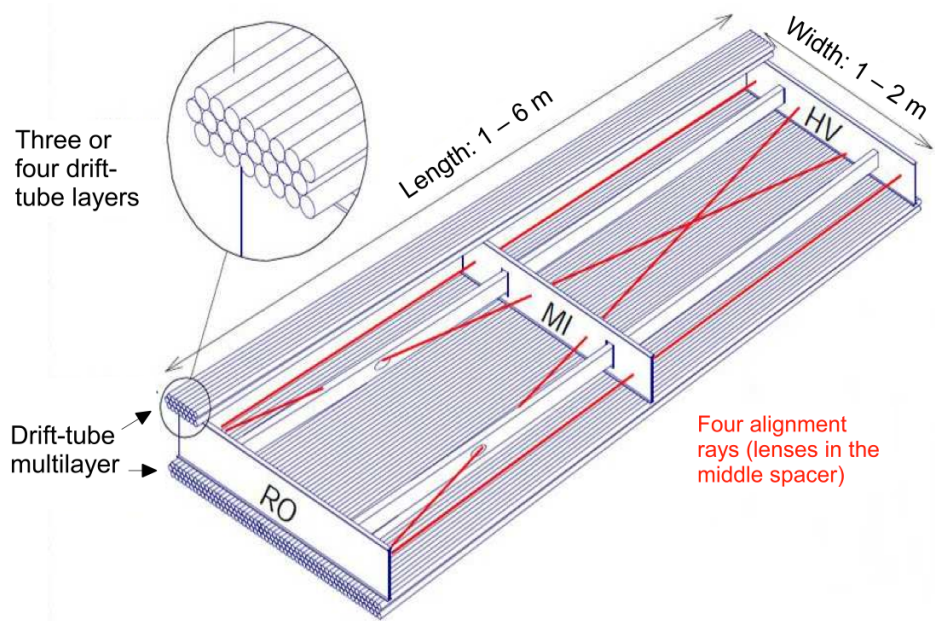


**Figure 5.10:** Schematic of MDT chamber. [cite G35]

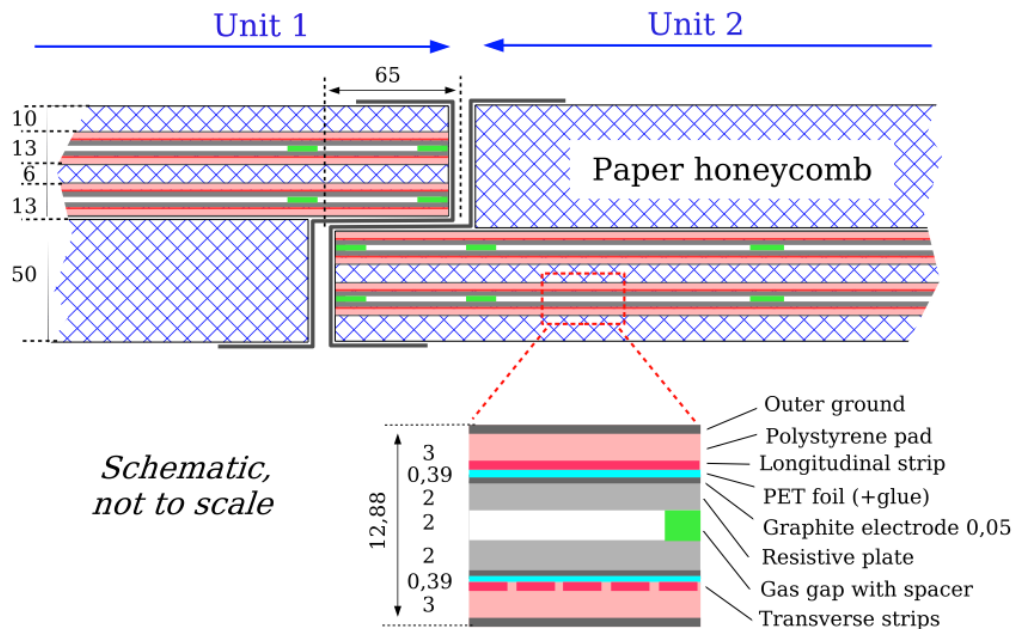


**Figure 5.11:** Schematic of RPC chamber, which is used for triggering in the central region of the detector [cite G35].

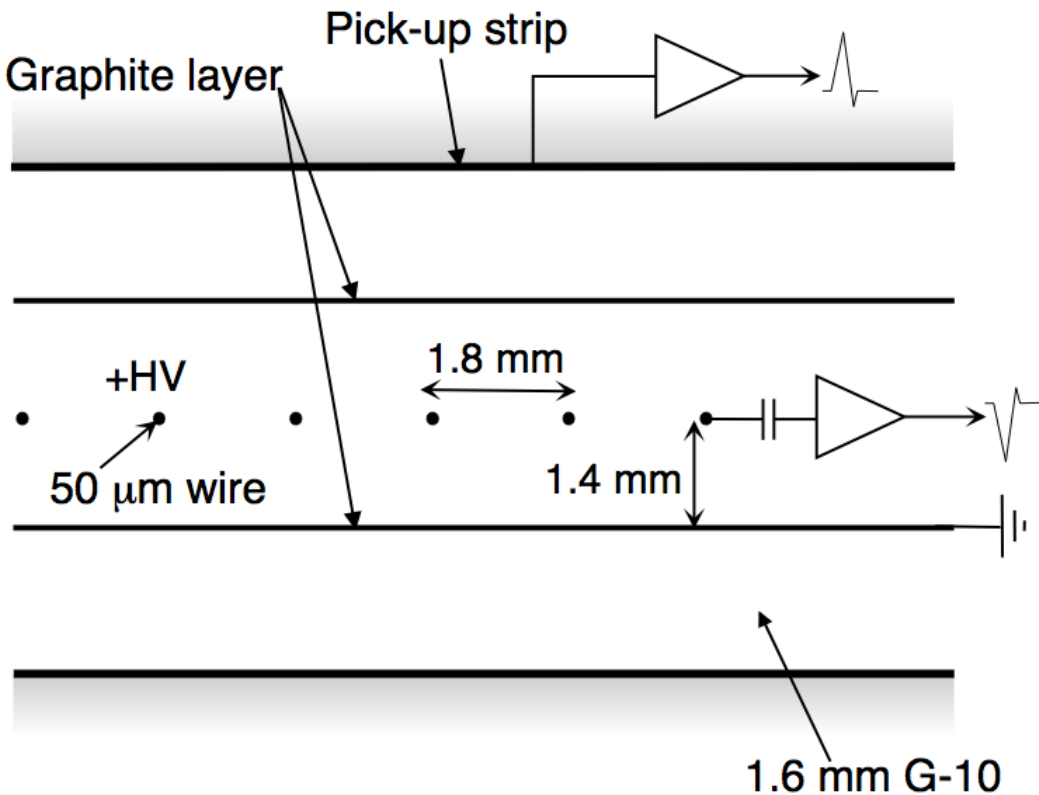


**Figure 5.12:** Schematic of TGC chamber, which is used for triggering in the muon end-cap region. [cite G35]

## 582    5.5 Magnet System

583    A particles with charge,  $q$ , and velocity  $v$ , moving in magnetic field,  $B$ , ex-  
 584    periences a force,  $F = qv \times B$ . This force can cause charged particles to have a  
 585    curved trajectory in magnetic fields, which the ID and MS use to determine the  
 586    particles  $p_T$ . The central solenoid provides the magnetic field for the ID and the  
 587    toroidal magnets provide the magnetic field for the MS.

588    The layout of the magnet system is shown in Figure 5.13. The central solenoid  
 589    consists of a single-layer Al-stabilized NbTi conductor coil wound inside an Al

590 support cylinder. The solenoid is 5.8 m long, 50 cm thick and has an inner radius  
591 of 1.23 m. It is cooled to 4.5 K to reach superconducting temperatures and shares  
592 the liquid argon calorimeter vacuum vessel to minimize material in the detector.  
593 A current of 7.730kA produces a 1.998 T solenoidal magnetic field, pointing in  
594 the  $+z$  direction.

595 The toroidal magnet system consists of a barrel and two end-cap toroidal  
596 magnets used to a magnetic field outside the calorimeters that is orientated along  
597  $\phi$ . Each barrel toroid is 25.3 m long with an inner and outer diameter of 9.4 and  
598 20.1 m and weighs 830 tonnes. Endcap toroids are 5 m long with an inner and  
599 outer radius of 1.65 and 10.7 m. Both toroid systems use Al-stabilized Nb/Ti/Cu  
600 conductors. The magnetic field strength of the barrel and endcap regions are 0.5  
601 and 1 T.

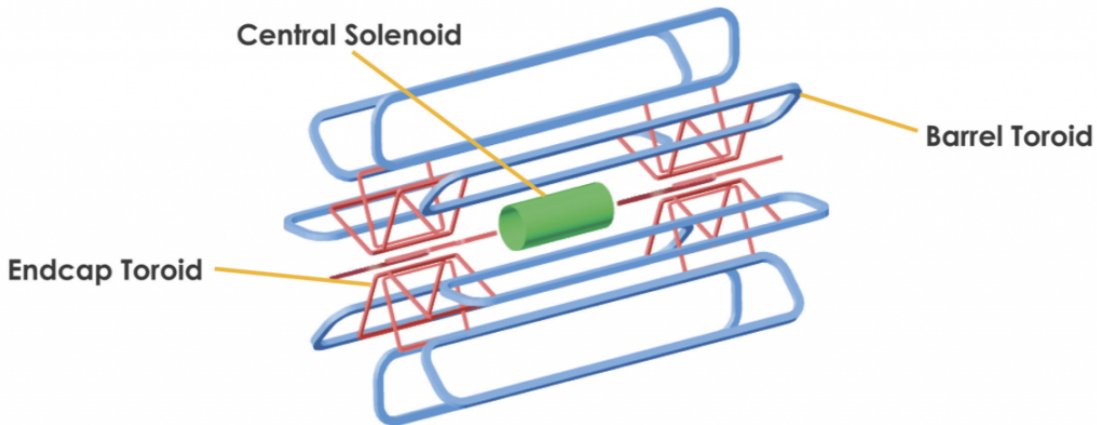


**Figure 5.13:** Layout of ATLAS magnet systems.

## 602 **5.6 Trigger System**

603 Since collisions occur every 25 ns and reading out all detector channels and  
604 storing that information is not currently feasible (saving 60 million megabytes per

second), the majority of events are not kept for analysis. ATLAS uses a multi-stage trigger system to select approximately 1,000 of the 1.7 billion collisions that occur each second (corresponding to a rate of 1 kHz from the 40 MHz proton collision rate). The first stage of the trigger system is the hardware level (L1) trigger. This trigger reduces the event rate to 100 kHz by identifying Regions-of-Interest (ROIs) containing high  $p_T$  leptons, photons, jets, or  $E_T^{miss}$  by using information from RPCs, TGCs, and calorimeters to make a 2.5  $\mu$ s decision. This information is then passed to a high-level trigger (HLT) which further decreases event rates to 1 kHz. The HLT uses finer granularity measurements from the MS and ID to perform simplified offline reconstruction to decide which events to keep.

## **Part III**

616

## **Method**

617

618 **Chapter 6**

619 **Dataset and Simulated Samples**

620 **6.1 Dataset**

621 This analysis uses  $pp$  collision data collected from 2015 to 2018 at  $\sqrt{s} = 13$   
622 TeV, corresponding to 139/fb of data as shown in Figure 6.1 and 6.2. From this  
623 dataset, only those events in which the tracker, calorimeters, and muon spectrom-  
624 eter have good data quality are used. For a given event, the solenoid and toroidal  
625 magnets must also be operating at their nominal field strengths. In addition to  
626 this, events must pass further quality checks to reject events where detector sub-  
627 systems may have failed. These selections reject events that containing LAr noise  
628 bursts, saturation in the electromagnetic calorimeter, TileCal errors, and failures  
629 in event recovery due to tracker failures. Events with information missing from  
630 subsystems (usually due to busy detector conditions) are rejected. Events must  
631 also contain a primary vertex with at least two associated tracks, where the pri-  
632 mary vertex is selected as the vertex with the largest  $\sum p_T^2$  over tracks associated  
633 with the vertex and  $p_T > 0.5$  GeV.

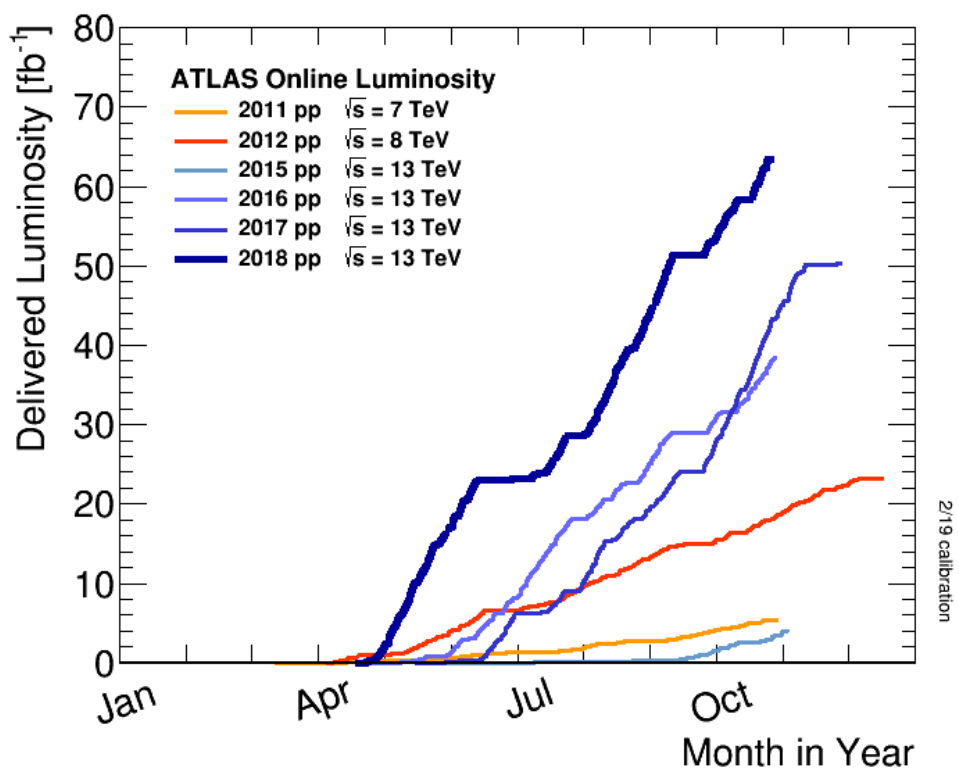


**Figure 6.1:** Integrated luminosity for data collected from ATLAS from 2011 - 2018

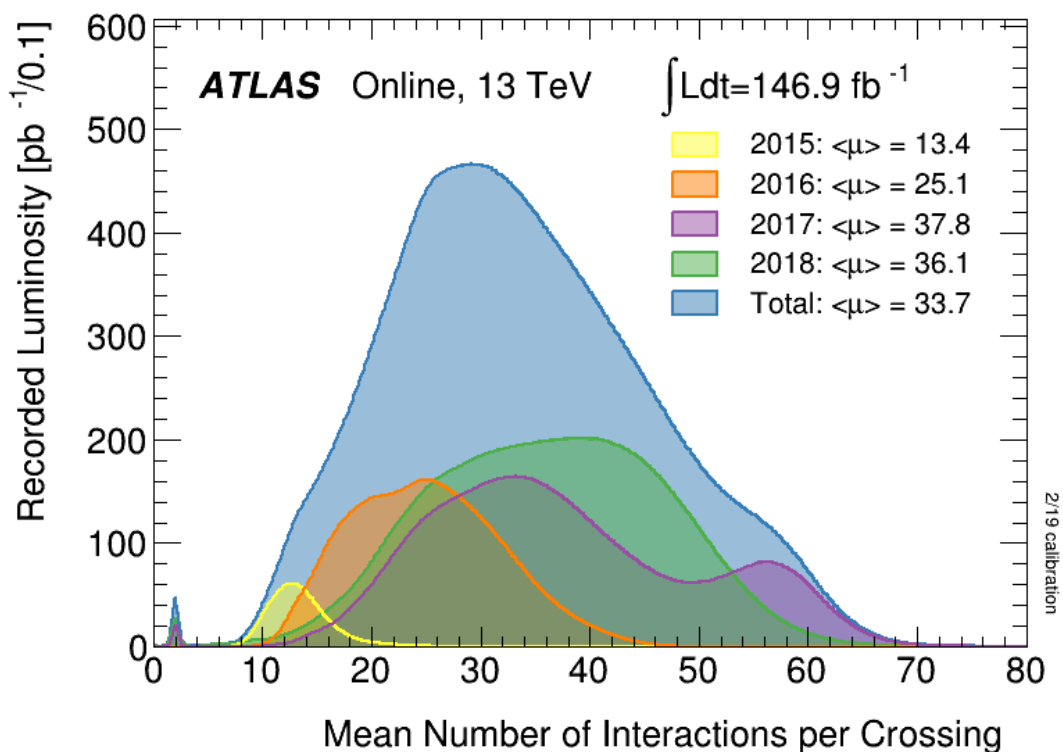


**Figure 6.2:** Mean number of interactions per crossing for data collected from ATLAS from 2011 - 2018

634 **6.2 Simulated Samples**

635 Samples are simulated in order to model backgrounds, evaluate signal ac-  
636 ceptance, optimize event selection and estimate systematic and statistical uncer-  
637 tainties. The dominant backgrounds for this analysis are  $W/Z + \text{jets}$ , diboson  
638 ( $WZ/WW$ ),  $t\bar{t}$ , single top and multijet production.

639  $W/Z+\text{jet}$  events are simulated using Sherpa 2.2.1 at NLO [cite [29]] and merged  
640 with the Sherpa parton shower using the ME+PS prescription [11]. These events  
641 are then normalized to NNLO cross sections. The  $t\bar{t}$  and single-top backgrounds  
642 are generated with Powheg-Box with NNPDF3.0NLO PDF sets in the matrix  
643 element calculation [cite[35]]. Top quarks are decayed using MadSpin [cite[36]].  
644 For all processes, the parton shower, fragmentation, and underlying event are  
645 simulated using Pythia 8.320 with the A14 tune set[cite[ATL-PHYS-PUB-2014-  
646 02]]. Diboson processes are generated using Sherpa 2.2.1.

647 Signal samples are simulated using MadGraph 5-2.2.2 [cite 42] and Pythia  
648 8.186 with NNPDF230LO. RS Graviton samples are generated with  $k/M_{PL}=1$ .  
649 HVT Model A and B samples are simulated with  $g_H = -0.56$  and  $g_f = -0.55$ ,  
650 as the difference in the width of the samples is smaller than detector resolution.  
651 Model C is generated by setting  $g_H = 1$  and  $g_f = 0$  to model VBF production of  
652 HVT bosons. Signals are generated for masses between 300 GeV and 6 TeV.

653 **6.3 Object Selection**

654 **6.3.1 Electrons**

655 Electrons are reconstructed from electromagnetic showers in the LAr EM  
656 calorimeter. During reconstruction cells of  $\Delta\eta \times \Delta\phi = 0.025 \times 0.025$  are grouped  
657 into  $3 \times 5$  clusters. These clusters are then scanned for local maxima that seed elec-

tron clusters. These clusters must then be matched to ID track from the PV. This requirement minimizes non-prompt electron and fake electron backgrounds. Electrons must pass identification and isolation requirements. Electron identification (loose, medium, tight) classification is based on the discriminant of the multivariate analysis that identifies electrons using a likelihood based method. For this analysis tight electrons are used. Electrons are also required to be isolated. The electron isolation is calculated by comparing the sum of the transverse momentum in a cone around the electron of size  $\Delta R = 0.2$  to the transverse momentum of the electron. This quotient must be less than 3.5, to further reject non-prompt photons and other fake backgrounds (multijet). Electrons in this analysis are also required to have  $p_T > 30$  GeV and  $|\eta| < 2.47$ . Electrons are also required to have  $p_T > 30$  GeV.

Electrons are calibrated to determine a data-driven scale factors from  $J/\Psi \rightarrow ee$ ,  $Z \rightarrow ee$ ,  $Z \rightarrow \ell\ell\nu$  processes. These corrections account for the non-uniform response of the detector by introducing modeling and reconstruction uncertainties.

### 6.3.2 Muons

As muons traverse the entire detector, they are reconstructed from ID and MS tracks. For this analysis the muon identification and isolation working points are chosen to minimize the contributions from non-prompt muons. Towards this end, the medium muon identification working point is used. For this working point, two types of reconstructed muons are used: combined and extrapolated muons (CB and ME, respectively). For CB muons, ID and MS tracks are reconstructed independently and a combined track fit is performed by adding or removing MS tracks to improve the fit quality. ME muons are reconstructed from only MS tracks with hits in at least two layers, which ensures the track originates from the

683 PV. ME muons extend the acceptance for muon reconstruction outside the ID  
684 from  $2.5 < |\eta| < 2.7$ . The medium identification working point uses CB and ME  
685 tracks. CB tracks must have at least 3 hits in two MDT layers. ME tracks are  
686 required to have at least three MDT/CSC hits. To further minimize contributions  
687 from fake muons, the selected muons are required to be isolated from other tracks,  
688 as muons from  $W, Z$  decays are often isolated from other particles. To insure the  
689 selected muons are isolated, the scalar sum of the transverse momentum of tracks  
690 in a cone of  $\Delta R = 0.3$  compared to the transverse momentum of the muon must  
691 be less then 0.06. Muons are also required to have  $p_T > 30$  GeV.

692 Muons are calibrated using well-studied resonances  $J/\Psi \rightarrow \mu\mu$  (low- $p_T$ ),  $Z \rightarrow$   
693  $\mu\mu$  (high- $p_T$ ). Figure 6.3 shows the combined muon  $p_T$  uncertainty from this  
694 calibration. The total systematic uncertainty is less then 1% for all  $p_T$  ranges  
695 considered in this analysis.

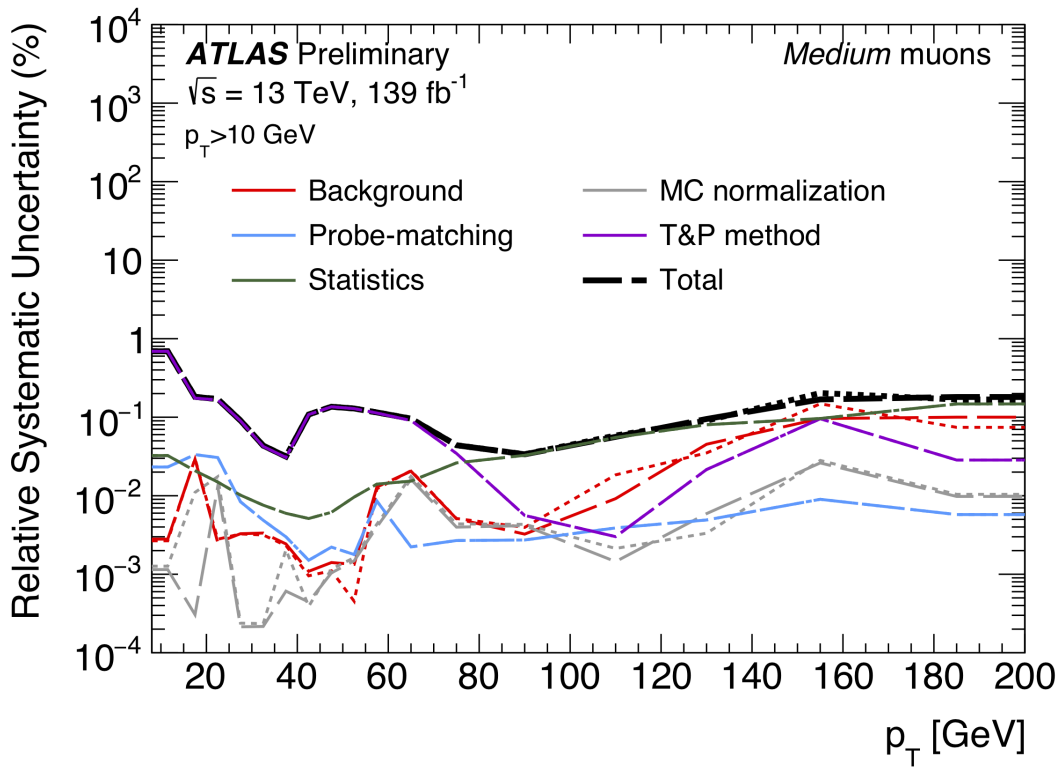


**Figure 6.3:** [4] This figure show the breakdown of the muon reconstruction efficiency scale factor measured in  $Z \rightarrow \mu\mu$  as a function of  $p_T$

### 6.3.3 small-R jets

Calorimeter jets are used to reconstruct the hadronically decaying  $W/Z$  candidates in the resolved analysis. These jets are less boosted and therefore spatially separated and reconstructed separately. These jets are constructed from topologically connected clusters of calorimeter cells (topoclusters), seeded from calorimeter cells with energy deposits significantly above the noise threshold. These cells are then used as inputs to the  $anti - k_T$  algorithm [12] with a distance = 0.4, here called small-R jets. These jets are calibrated to compensate and account for biases from jet reconstruction.

The jet energy is calibrated sequentially as shown in Figure 6.4. After the

706 jet direction is corrected to point to the PV, the energy of the jet is corrected.

707 First, the jet energy is corrected to account for pileup contributions based on the  
708  $p_T$  and area of the jet (these corrections are extracted from a  $pp \rightarrow jj$  sample).

709 Following this, another pileup correction is applied that scales with  $\mu$  and  $N_{PV}$ .

710 Then, MC-based corrections are applied that are meant to transform the jet  
711 energy and  $\eta$  back to truth level. Therefore, these corrections account for the  
712 non-compensating nature of the ATLAS calorimeters and inhomogeneity of the  
713 detector. Following this the Global sequential calibration is applied that reduces  
714 flavor dependence and jet that deposit energy outside the calorimeters. Finally,  
715 in-situ corrections are applied that account for differences in jet responses between  
716 data and simulation ( $\gamma/Z+jet$  and multijet samples are used). These differences  
717 can be due to mismodelling of the hard scatter event, pile-up, jet formation, etc.

718 Jet used in this analysis must have  $p_T > 30$  GeV and  $|\eta| < 2.5$ . To further  
719 reduce fake jets the jet-vertex-tagger (JVT) is used to reject pile-up jets [cite 43  
720 P]. The JVT uses two track-based variables, corrJVF and  $R_{p_T}$  to calculate the  
721 likelihood that the jet originated from the PV. The corrJVF compares the scalar  
722 sum of the  $p_T$  of tracks associated with the jet and PV to the scalar sum of the  
723  $p_T$  of tracks associated with the jet. This variable also includes a correction that  
724 reduces the dependency of corrJVF with the number of reconstructed vertices in  
725 the event.  $R_{p_T}$  is given by the ratio of the scalar sum of the  $p_T$  of tracks associated  
726 with the jet and PV to the  $p_T$  of the jet. Both of these variables peak around zero  
727 for pileup jets, as these jets are unlikely to have tracks associated with the PV.  
728 JVT cuts are applied to all jets with  $p_T > 120$  GeV. Central jets ( $|\eta| < 2.4$ ) are  
729 required to have a  $JVT > 0.59$  and forward jets ( $2.4 < |\eta| < 2.5$ ) are required to  
730 have  $JVT > 0.11$ .

731 To further reject fake jets, jets must pass quality requirements based on the

<sup>732</sup> following variables ([cite P42]):

<sup>733</sup> -  $f_Q^{LAr}$ : fraction of energy of jet's LAr cells with poor signal shape

<sup>734</sup> -  $f_Q^{HEC}$ : fraction of energy of jet's HEC cells with poor signal shape

<sup>735</sup> -  $E_{neg}$ : sum of cells with negative energy

<sup>736</sup> -  $f_{EM}$ : fraction of jet's energy deposited in EM calorimeter

<sup>737</sup> -  $f_{HEC}$ : fraction of jet's energy deposited in HEC calorimeter

<sup>738</sup> -  $f_{max}$ : maximum energy fraction in any single calorimeter layer

<sup>739</sup> -  $f_{ch}$ : ratio of the scalar sum of the  $p_T$  of a jet's charged tracks to the jet's  $p_T$

<sup>740</sup> Jets selected for the resolved analysis must pass one of the following criteria:

<sup>741</sup> -  $f_{HEC} > 0.5$  and  $|f_Q^{HEC}| > 0.5$  and  $\langle Q \rangle > 0.8$

<sup>742</sup> -  $|E_{neg}| > 60$  GeV

<sup>743</sup> -  $f_{EM} > 0.95$  and  $f_Q^{LAr} > 0.8$  and  $\langle Q \rangle > 0.8$  and  $|\eta| < 2.8$

<sup>744</sup> -  $f_{max} > 0.99$  and  $|\eta| < 2$

<sup>745</sup> -  $f_{EM} < 0.05$  and  $f_{ch} < 0.05$  and  $|\eta| < 2$

<sup>746</sup> -  $f_{EM} < 0.05$  and  $|\eta| > 2$

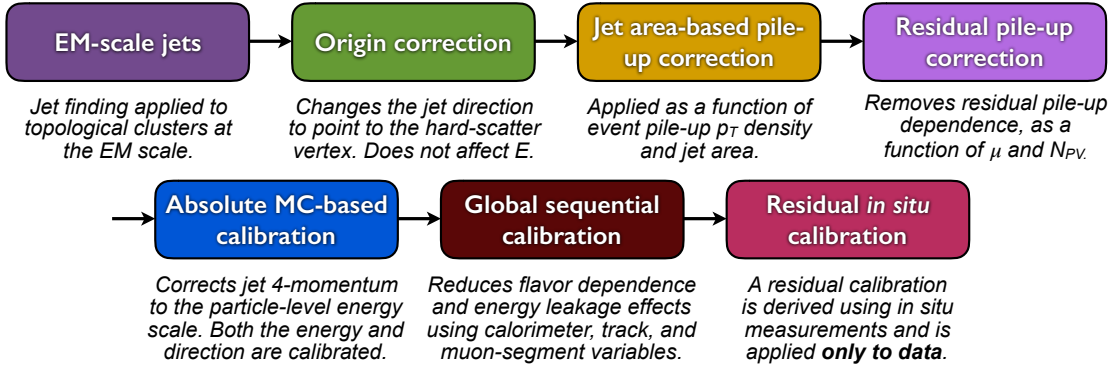


**Figure 6.4:** [6] This diagram shows the calibration stages for EM jets.

### 747 6.3.4 large-R jets

748 Large-R ( $\Delta R = 1.0$ ) jets are used to reconstruct the high- $p_T W/Z \rightarrow qq$  candi-  
 749 dates in the merged analysis. Track-Calorimeter Clusters (TCCs) are used to reconstruct  
 750 these jets [cite ANA 50]. These jets are constructed via a pseudo particle flow  
 751 method using ID tracks matched to calorimeter clusters. The angular resolution  
 752 of the calorimeter degrades sharply with jet  $p_T$ , but the jet energy resolution im-  
 753 proves. The tracker has excellent angular resolution improves with  $p_T$ . Therefore,  
 754 by matching tracks to jets, TCCs have more precise energy and angular resolution  
 755 the jets constructed from calorimeter information only. These jets are required to  
 756 have  $p_T > 200$  GeV,  $|\eta| < 2.0$  and  $m_J > 50$  GeV.

757 TCC jets are trimmed as detailed in [cite ANA 45], which suppresses pileup  
 758 and soft radiation in the jet, the jet mass is calculated as the four-vector sum  
 759 of the jet's constituents (assuming massless constituents). The jet mass peaks  
 760 around the  $W/Z$  boson mass for  $W/Z \rightarrow qq$  jets, and more broadly for quark and  
 761 gluon induced jets.

762 These jets are then tagged as  $W/Z$  jets if they pass the jet mass and  $D_2$   
 763 cuts. The jet substructure variable  $D_2$  is given by the ratio of energy correlation  
 764 functions based on energies and pair-wise angles of a jet's constituents [cite ANA

765 46, 47]:

$$D_2^{\beta=1} = E_{CF3} \left( \frac{E_{CF1}}{E_{CF2}} \right)^3 \quad (6.1)$$

766 Where the energy correlation functions are defined as:

$$E_{CF1} = \sum_i p_{T,i} \quad (6.2)$$

767

$$E_{CF2} = \sum_{ij} p_{T,i} p_{T,j} \Delta R_{ij} \quad (6.3)$$

768

$$E_{CF3} = \sum_{ijk} p_{T,i} p_{T,j} p_{T,k} \Delta R_{ij} \Delta R_{jk} \Delta R_{ki} \quad (6.4)$$

769 A two-dimensional optimization of the jet mass and  $D_2$  thresholds was per-  
770 formed to provide maximum sensitivity for this analysis. Figure ?? shows the  
771 optimized thresholds on  $D_2$  and jet mass as a function of  $p_T$ . Figure 6.6 shows  
772 the efficiency of the optimized  $W/Z$  taggers as a function of jet  $p_T$ .

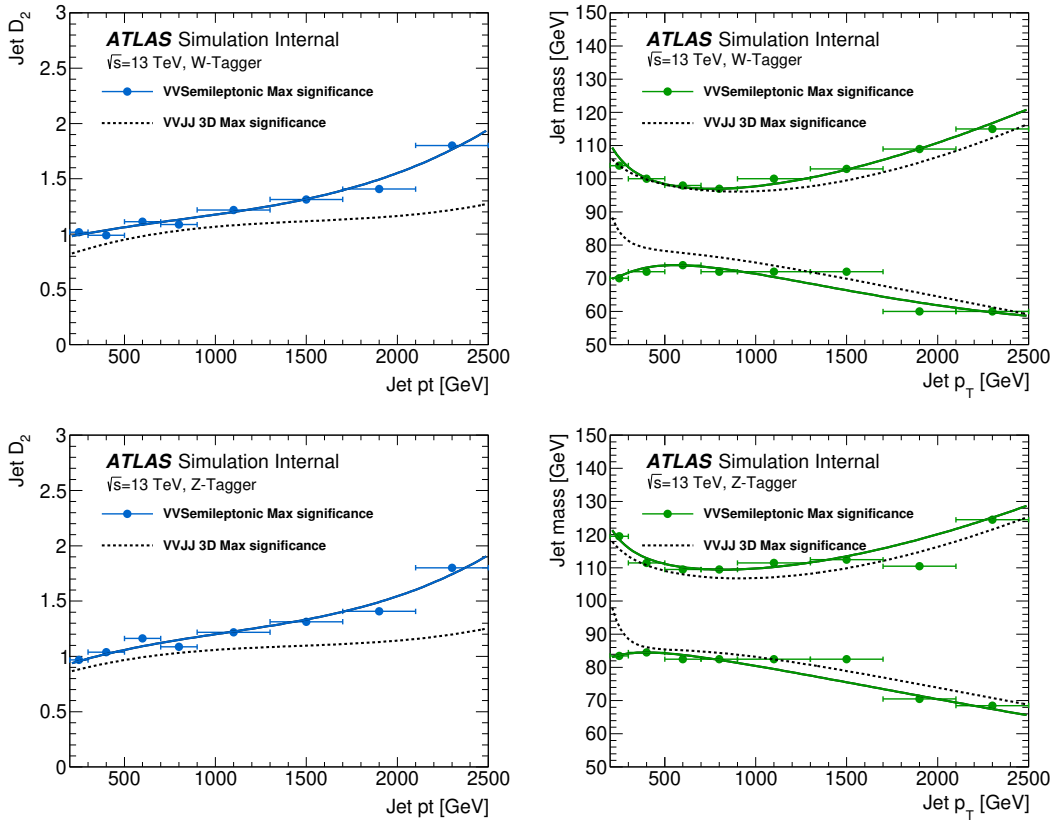


**Figure 6.5:** The upper cut on  $D_2$  (a) and jet mass window cut i.e. the upper and lower boundary of the mass (b) of the  $W$ -tagger as a function of jet  $p_T$ . Corresponding values for  $Z$ -tagger are shown in (c) and (d). The optimal cut values for maximum significance are shown as solid markers and the fitted function as solid lines. Working points from  $VV \rightarrow JJ$ [ATLAS-HDBS-2018-31-002] is also shown as dashed lines as a reference. Natasha reword?

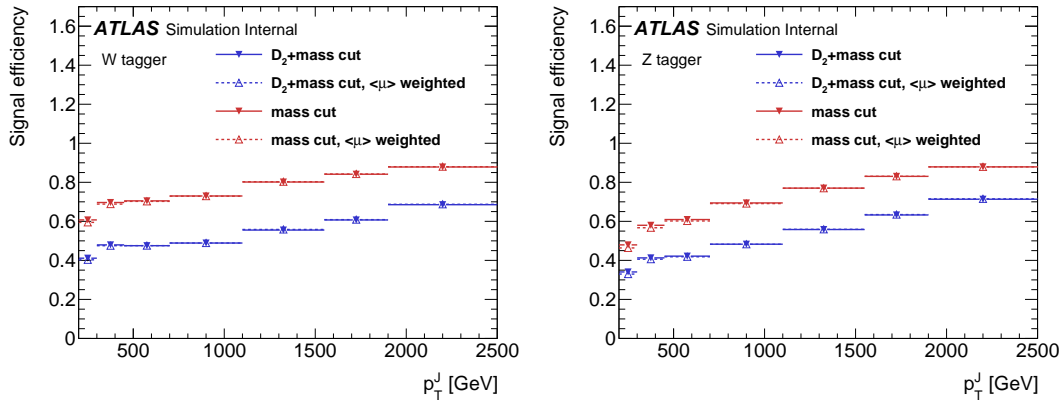


**Figure 6.6:** Natasha write caption

773 **6.3.5 Variable Radius jets**

774 Variable-radius (VR) track jets are used to identify b-quark induced jets in  
775 large-R jets [cite ANA 52]. These jets use a  $p_T$  dependent cone size defined as:

$$R_{eff}(p_{T,i} = \frac{\rho}{p_{T,i}}) \quad (6.5)$$

776 for building jets from ID tracks with an anti-kt algorithm. For this analysis  
777  $\rho = 30$  GeV and an upper and lower limit on cone size are set to 0.02 and 0.4,  
778 respectively. Collinear VR jets are possible, so track jets that are not separated  
779 by the the smaller jet's cone size are not used. These jets are also required to  
780 have  $p_T > 10$  GeV and  $|\eta| < 2.5$ .

781 **6.3.6 MET/neutrinos**

782 As neutrinos are uncharged and color less they do not leave tracks or jets in  
783 the detector. For this reason, neutrinos are reconstructed calculated the  $E_T^{miss}$ .  
784 This quantity is defined as negative vector sum of  $p_T$  all the physics objects and  
785 an extra "soft" term. The "soft" term accounts for energy depsoits not associated  
786 with any of the objects in the event. For this analysis the soft term is given by  
787 the summing the  $p_T$  of all ID tracks not associated with objects in the event. The  
788 selected tracks must be matched to the primary vertex, which decreases pile-up  
789 contamination [cite G 217 218]. The tight working point is used [Natasha look up  
790 what this means].

791 **6.3.7 Jet Flavor Tagging**

792 To further classify events, the small radius jets are identified as originated  
793 for a b-quark or not using the multivariate  $b$ -tagging algorithm (BDT), MC2c10

794 [cite G 210 199]. This algorithm uses the impact parameters of the jet's ID tracks,  
795 secondary vertices (if they exist), and reconstructed flight paths of  $b$  and  $c$  hadrons  
796 in the jet to determine if the jet was induced by a  $b$ -quark. For this analysis the  
797 85% efficient working point of this algorithm is used to a fixed cut on the BDT  
798 discriminant that yields an 85% tag rate, and  $c$ ,  $\tau$ , and light-flavor jet rejection of  
799 3, 8, and 34 respectively in a simulated  $t\bar{t}$ .

800 **6.3.8 Overlap Removal**

801 The reconstructed jets and leptons in this analysis can arise from the same  
802 energy deposits. For instance, a jet may radiate an electron that is then recon-  
803 structed separately as the signal lepton in the event. To mitigate this confusion  
804 of multiple objects originating from a single jet or lepton overlapping objects are  
805 removed via a procedure referred to a overlap removal. In this procedure the sep-  
806 aration of the two objects,  $\Delta(R) = \sqrt{(\Delta\eta)^2 + (\Delta\text{phi})^2}$  determines which object is  
807 removed from the event.

808 The overlap selections used in this analysis are:

- 809 - when an electron shares a track the electron with the lower  $p_T$  is rejected,  
810 as it is more likely to be a fake electron
- 811 - when a muon and electron share a track the muon is rejected if it is a  
812 calo-muon, otherwise the electron is rejected
- 813 - when  $\Delta R < 0.2$  for an electron and jet, the jet is rejected to maximize signal  
814 acceptance
- 815 - when  $\Delta R > 0.2$  for an electron and jet, the electron is rejected as likely  
816 originated from decays within the jet

- 817        - when  $\Delta R < \min(0.4, 0.04 + 10\text{GeV}/p_T^\mu)$  the muon is rejected, again maxi-
- 818              mizing signal acceptance, otherwise the jet is rejected
- 819        - when  $\Delta R < 1.0$  for the a large-R jet and electron, the jet is rejected

820 **Chapter 7**

821 **Event Selection and**

822 **Categorization**

823 **7.1 Pre-selection**

824 Before applying topological cuts to suppress backgrounds and reduce data  
825 size in this search, preselection cuts are applied which include trigger and event  
826 requirements. Events must contain exactly one tight lepton (no additional loose  
827 leptons), the  $p_T^{\ell\nu} > 75$  GeV, and there must be at least two small-R jets or one  
828 large-R jet.

829 **7.2 Trigger**

830 The data was collected using the lowest unprescaled single-lepton or  $E_T^{miss}$   
831 triggers, as summarized in Table [natasha add table]. Since the muon term is not  
832 considered in the trigger  $E_T^{miss}$  calculation, the  $E_T^{miss}$  trigger is fully efficient to  
833 events with high- $p_T$  muons. For this reason, the  $E_T^{miss}$  trigger is used for events  
834 where  $p_T^\mu > 150$  GeV, to compensate for the poor efficiency of the single muon

<sup>835</sup> trigger below 150 GeV (due to detector coverage).

**Table 7.1:** The list of triggers used in the analysis.

Data-taking period	$e\nu qq$ channel	$\mu\nu qq$ ( $p_T(\mu\nu) < 150$ GeV) channel	$\mu\nu qq$ ( $p_T(\mu\nu) > 150$ GeV) channel
2015	HLT_e24_lhmedium_L1EM20 OR HLT_e60_lhmedium OR HLT_e120_lhloose	HLT_mu20_iloose_L1MU15 OR HLT_mu50	HLT_xe70
2016a (run $< 302919$ ) $(L < 1.0 \times 10^{34} \text{ cm}^{-2} \text{ s}^{-1})$	HLT_e26_lhtight_nod0_ivarloose OR HLT_e60_lhmedium_nod0 OR HLT_e140_lhloose_nod0 HLT_e300_etcut	HLT_mu26_ivarmedium OR HLT_mu50	HLT_xe90_mht_L1XE50
2016b (run $\geq 302919$ ) $(L < 1.7 \times 10^{34} \text{ cm}^{-2} \text{ s}^{-1})$	same as above	same as above	HLT_xe110_mht_L1XE50
2017	same as above	same as above	HLT_xe110_pufit_L1XE55
2018	same as above	same as above	HLT_xe110_pufit_xe70_L1XE50

836    **7.3 GGF/VBF RNN**

837    To classify events as originating from GGF/DY or VBF production a recursive  
838    neural network (RNN) is used. This approach is more powerful than a cut-based  
839    classification as it improves signal efficiency and analysis sensitivity by exploit-  
840    ing correlations between variables that the RNN learns. In particular, a RNN  
841    architecture is ideal as it can handle variable numbers of jets in the events.

842    The RNN uses the four-momentum of candidate VBF jets to classify events  
843    as VBF or GGF topologies. As sometimes jets will be incorrectly reconstructed  
844    the number of jets in the event are expected to vary across the inputs samples.  
845    VBF candidate jets are identified by removing jets from the event that are likely  
846    from  $W/Z \rightarrow qq$ . For the resolved regime this means removing the two leading  
847    small-R jets from the VBF candidate jet list. For the merged regime this means  
848    removing small-R jets that are  $\Delta R < 1.0$ . Also the VBF candidate jets are also  
849    required to be within  $|\eta| < 4.5$ . From the list of remaining VBF candidate jets,  
850    the two highest- $p_T$  jets are chosen.

851    The architecture of the RNN is show in Figure 7.1. LSTMs are a type of  
852    RNN that extract meaningful information and can retain it (unlike other neural  
853    networks architectures). This is useful for VBF event classification for events with  
854    two jets, where using the kinematic properties of both jets (and their correlations)  
855    will lead to more efficient event classification.

856    In this RNN architecture, the VBF candidates are first passed to a masking  
857    layer which checks the number of jets in the event. If there is only one jet, only  
858    one LSTM layer is used. The output of masking is then passed to a LTSM cell  
859    (with a tanh activation) [natasha cite LSTM], and then to a dropout layer, that  
860    has a probability of 0.3 to completely forget the output of the LSTM. Dropout  
861    is a regularization method, that prevents overfitting. The output of the dropout

862 layer is then passed to the second LSTM and then through another dropout layer  
863 with a probability of 0.3.

864 The weights and other parameters of the network are learned by training the  
865 network with VBF and GGF signals over 200 epochs with an Adam Optimizer  
866 [natasha add reference]. The training is truncated if the network parameters are  
867 unchanged after ten iterations. The training, testing and validation sets are 56,  
868 30, and 14 percent of the input samples, respectively. Figure [add INT figure  
869 32] shows the loss function of the network as a function of training epochs. The  
870 validation test set has a smaller loss function as dropout was not applied. Figure  
871 7.3 shows the ROC curve for the RNN using k-fold cross validation.

872 Finally this output is passed to a dense layer [natasha ask antonio about this]  
873 and then to a sigmoid activation layer, leading to an overall RNN score. Figure 7.2  
874 shows the RNN discriminant for shows modeling of the discriminant. The RNN  
875 score is 0 for GGF and background processes and 1 for VBF processes. Figure  
876 ?? shows the limits for various signal processes based on the RNN cut applied.  
877 The most efficient cut was found to be RNN Score > 0.8, for VBF classification.

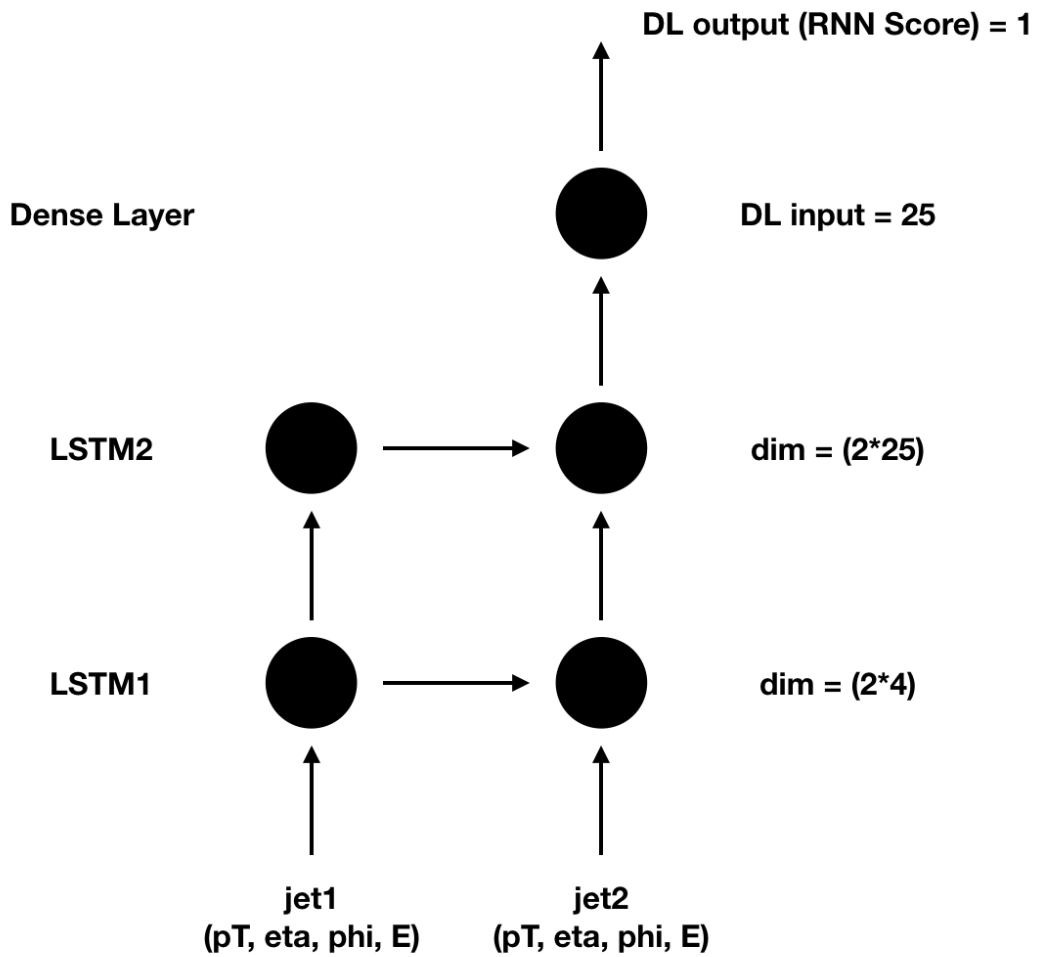


**Figure 7.1:** RNN architecture. Natasha add caption

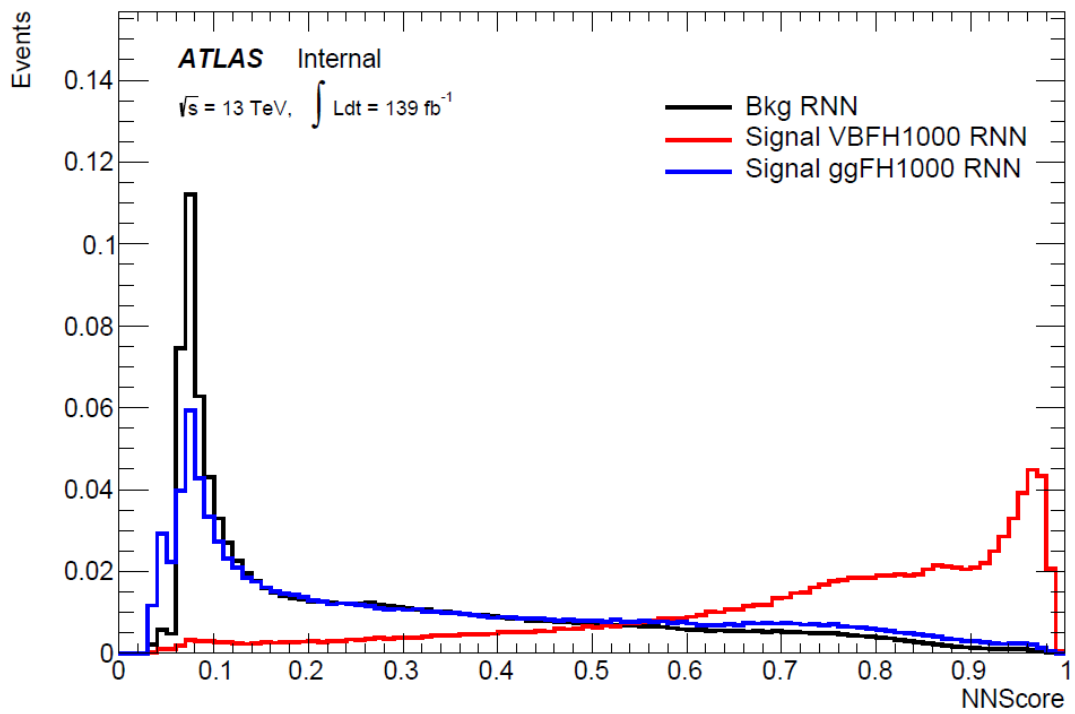


**Figure 7.2:** RNN Score distribution for ggF and VBF signals and backgrounds.

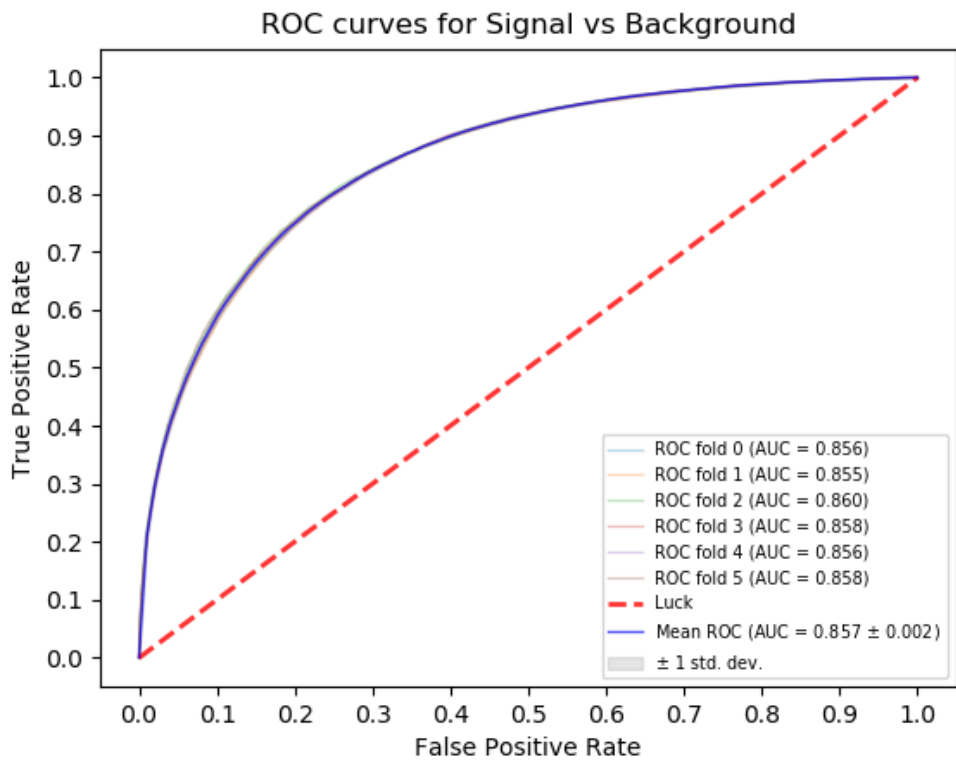


**Figure 7.3:** ROC curve using k-fold validation for RNN.

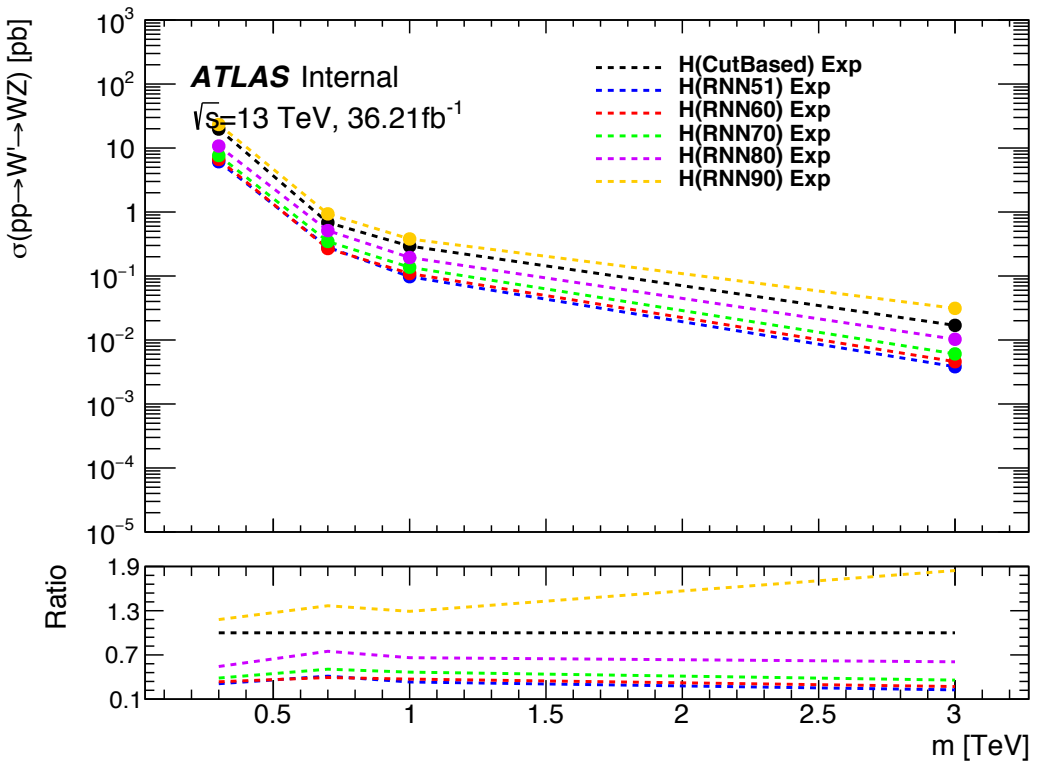


**Figure 7.4:** Comparison of GGF  $Z'$  limits for different RNN score selections.

## 878    7.4 Topological Cuts

879       Once an event is classified as VBF or GGF via the RNN it must pass other  
 880       topological cuts that maximize signal efficiency and background rejection. First,  
 881       to efficiently select events with  $W \rightarrow \ell\nu$  candidate exactly one tight lepton is  
 882       required and  $E_T^{miss} > 100(60)$  GeV and  $p_{T,\ell\nu} > 200(75)$  GeV in the merged (re-  
 883       solved) analysis to suppress the multi-jet background. To more accurately model  
 884       the two dominant backgrounds in this analysis,  $W + \text{jets}$  and  $t\bar{t}$ , control regions are  
 885       used constructed for each. These control regions are dominated by these processes  
 886       and used to extract normalization factors that are then used in the signal region  
 887       estimates.

888       For the merged analysis, in addition to the  $W \rightarrow \ell\nu$  and  $W/Z \rightarrow J$  selections

above, the relative boson  $p_T$  is cut to enhance signals, i.e.  $\min(p_{T,\ell\nu}, p_{T,J})/m_{WV} > 0.35(0.25)$  for the GGF (VBF) category. To minimize  $t\bar{t}$  contamination the signal region and  $W+\text{jets}$  control region events with at least one b jet with  $\Delta R > 1.0$  from the large-R jet are excluded. For the  $t\bar{t}$  control region the event must contain at least one such b jet. High purity signal regions require the  $D_2$  and  $W/Z$  mass window cut to be passed, whereas the low purity region only requires the  $W/Z$  mass window cut to be passed. Finally for events to be classified as tagged the large-R jet must contain exactly two b-tagged jets. Untagged events must have no more than one b-tagged jet matched to the large-R jet. These selections are shown in Table 7.2. The distributions for the variables used in merged analysis for top control regions are shown in Figure 7.6- 7.9.

Events failing the merged selection are then re-analyzed in the resolved category. To enhance resolved signals, the event should contain two high- $p_T$  boson that are back-to-back in the x-y plane as shown by the cuts in Table 18. Again to suppress the  $t\bar{t}$  background in the WCR and SR events are required to have no additional b-jets.

The  $WV$  system mass,  $m_{WV}$  is reconstructed from the lepton, neutrino, and hadronically-decaying boson candidate. The momentum of the neutrino along the  $z$ -direction is obtained by constraining the  $W((Z))$  boson mass of the lepton neutrino system to be  $80.3$  ( $91.8$ )  $\text{GeV}/c^2$ . For complex solutions to this constraint,  $p_Z$  is taken as either the real component of the complex solutions or the one with the smaller absolute value of the two real solutions. For the resolved analysis,  $m_{WV}$  is reconstructed by constraining the  $W(Z)$  dijet system:

$$p_{T,jj}^{corr} = p_{T,jj} \times \frac{m_{W/Z}}{m_{jj}} \quad (7.1)$$

$$m_{jj}^{corr} = m_{W/Z} \quad (7.2)$$

**Table 7.2:** Summary of selection criteria used to define the signal region (SR),  $W$ +jets control region ( $W$  CR) and  $t\bar{t}$  control region ( $t\bar{t}$  CR) for merged 1-lepton channel.

Selection		SR		W CR (WR)		$t\bar{t}$ CR (TR1)	
		HP	LP	HP	LP	HP	LP
$W \rightarrow \ell\nu$	Num of Tight leptons	1					
	Num of Loose leptons	0					
	$E_T^{\text{miss}}$	$> 100 \text{ GeV}$					
	$p_T(\ell\nu)$	$> 200 \text{ GeV}$					
$W/Z \rightarrow J$	Num of large- $R$ jets	$\geq 1$					
	$D_2$ cut	pass	fail	pass	fail	pass	fail
	$W/Z$ mass window cut	pass	pass	fail	fail	pass	pass
	Numb. of associated VR track jets $b$ -tagged	For $Z \rightarrow J$ : $\leq 1$ ( $= 2$ ) for untagged (tagged) category					
	$\min(p_{T,\ell\nu}, p_{T,J}) / m_{WV}$	$> 0.35(0.25)$ for DY/ggF (VBF) category					
	Top-quark veto	Num of $b$ -tagged jets outside of large- $R$ jet	0		$\geq 1$		
Pass VBF selection			no (yes) for DY/ggF (VBF) category				

913 where  $m_{jj}$  and  $m_{W/Z}$  are the reconstructed invariant mass of the hadronically-  
914 decaying  $W/Z$  boson and the PDG values of the  $W/Z$  boson masses, respectively.  
915 A summary of the resolved selections is shown in Table 7.3. The distributions for  
916 the variables used in the resolved analysis in the TCR are shown in Figure 7.10,  
917 7.11.

918 Events classified as VBF events are classified as Merged High purity, low  
919 purity or resolved signal region selections sequentially. If the event does not pass  
920 any of these selections but passes a VBF control region selection it is classified as  
921 a VBF CR event. If the event fails the VBF selection it is then checked if it passes  
922 the Merged High purity, Low purity or resolved signal region selections (NB: for  
923 the WZ decay modes all the regions have tagged and untagged categories). If the  
924 event fails all the GGF signal region selections, it is then kept for GGF control  
925 region selections, if it passes those selections. This cutflow is shows in Figure 7.5.

**Table 7.3:** The list of selection cuts in the resolved analysis for the  $WW$  and  $WZ$  signal regions (SR),  $W+\text{jets}$  control region (WR) and  $t\bar{t}$  control region (TR).

cuts	SR	$W$ CR (WR)	$t\bar{t}$ CR (TR1)
$W \rightarrow \ell\nu$	Number of Tight leptons	1	
	Number of Loose leptons	0	
	$E_T^{\text{miss}}$	$> 60 \text{ GeV}$	
	$\cancel{p}_T(\ell\nu)$	$> 75 \text{ GeV}$	
$W/Z \rightarrow jj$	Number of small-R jets	$\geq 2$	
	Leading jet $p_T$	$> 60 \text{ GeV}$	
	Subleading jet $p_T$	$> 45 \text{ GeV}$	
	$Z \rightarrow q\bar{q}$ $W \rightarrow q\bar{q}$	$78 < m_{jj} < 105 \text{ GeV}$ $68 < m_{jj} < 98 \text{ GeV}$	$50 < m_{jj} < 68 \text{ GeV}$ or $105 < m_{jj} < 150 \text{ GeV}$
Topology cuts	Num. of $b$ -tagged jets	For $Z \rightarrow jj$ : $\leq 1$ ( $= 2$ ) for untagged (tagged) category	
	$\Delta\phi(j, \ell)$	$> 1.0$	
	$\Delta\phi(j, E_T^{\text{miss}})$	$> 1.0$	
	$\Delta\phi(j, j)$	$< 1.5$	
	$\Delta\phi(\ell, E_T^{\text{miss}})$	$< 1.5$	
Top vetos	$\min(p_{T,\ell\nu}, p_{T,jj}) / m_{WW}$	$> 0.35(0.25)$ for DY/ggF (VBF) category	
	Number of additional $b$ -tagged jets	0	$\geq 1$
Pass VBF selection		no (yes) for DY/ggF (VBF) category	

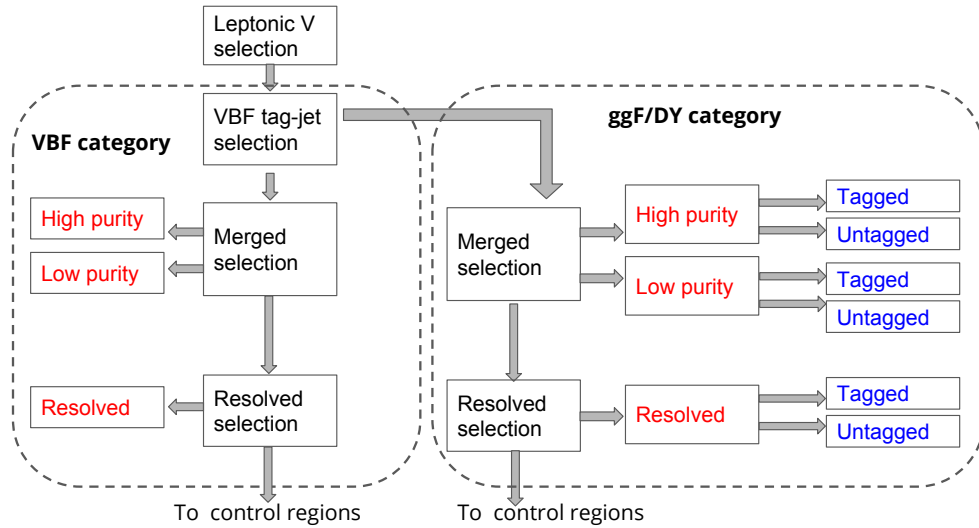


**Figure 7.5:** Event Categorization. Natasha write more.

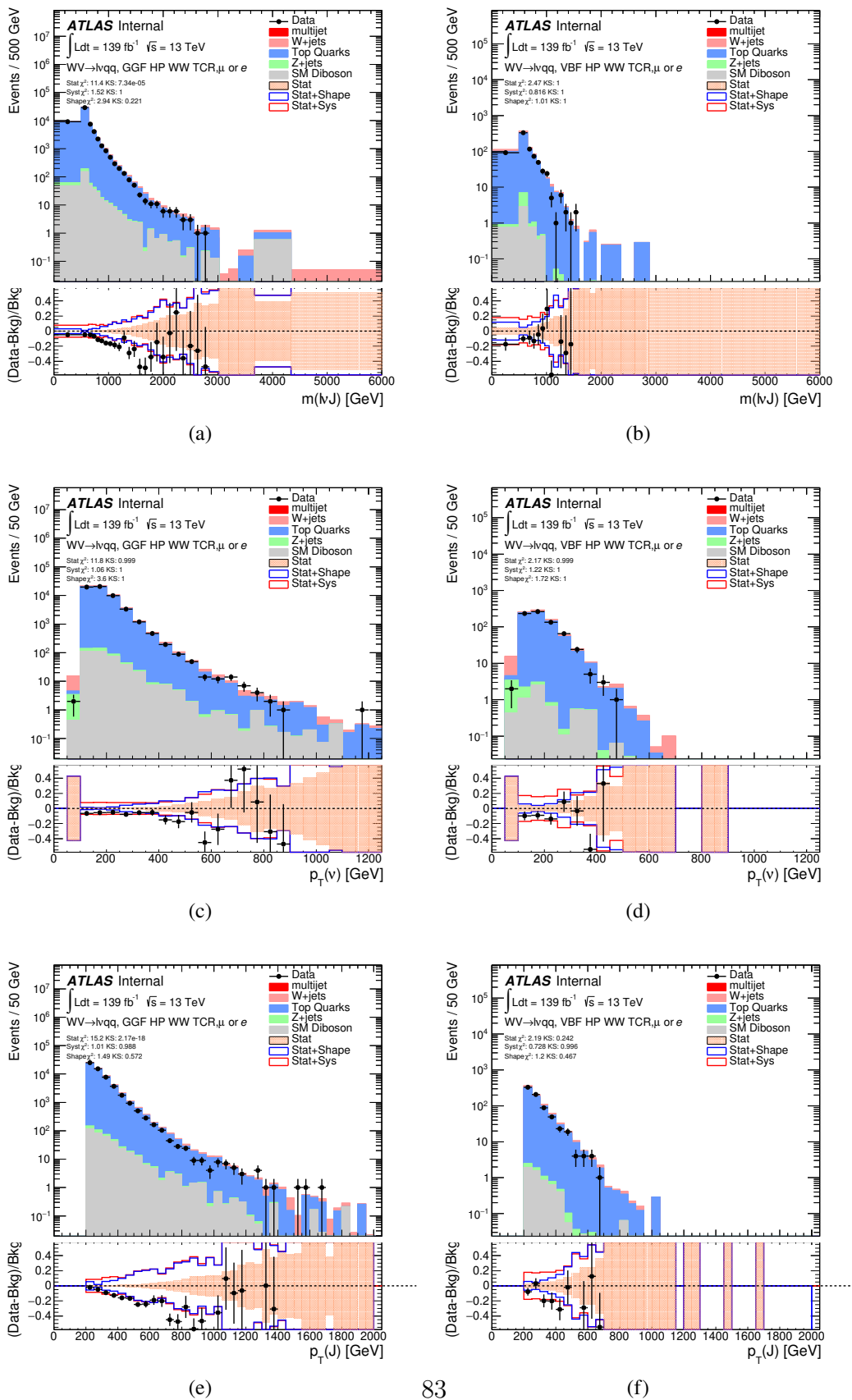


**Figure 7.6:** Data MC comparison for the merged  $WW$  HP TCR.

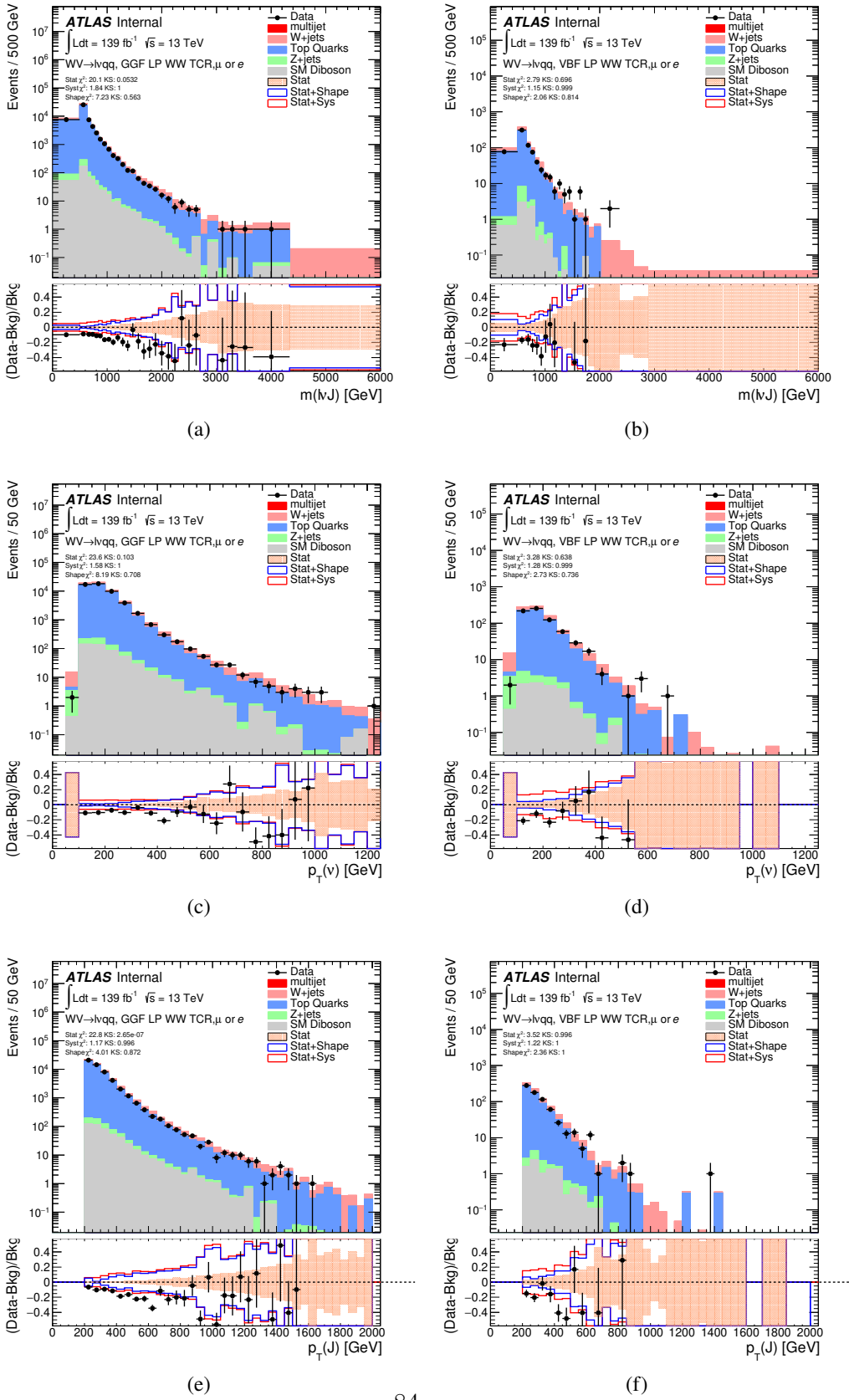
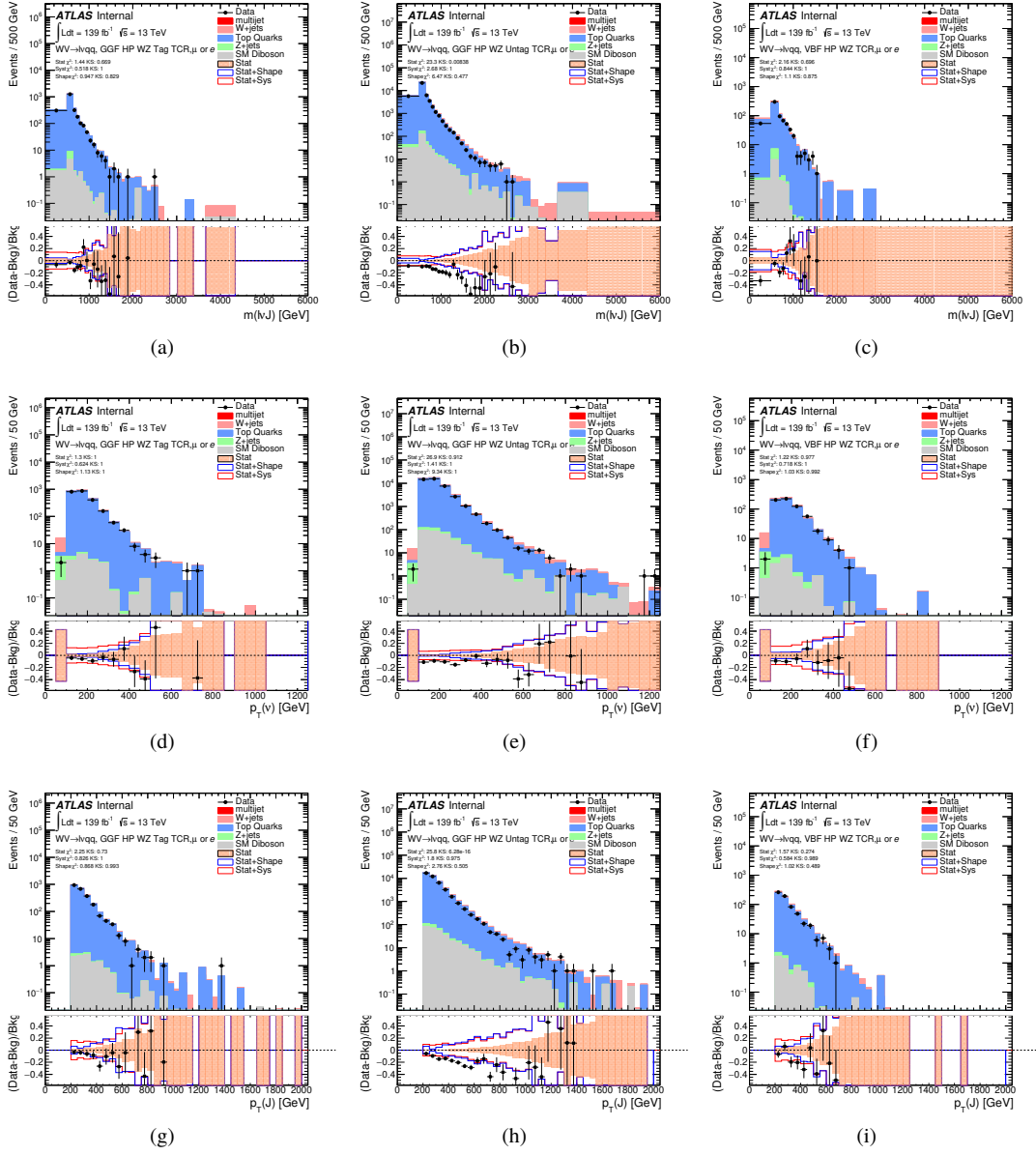
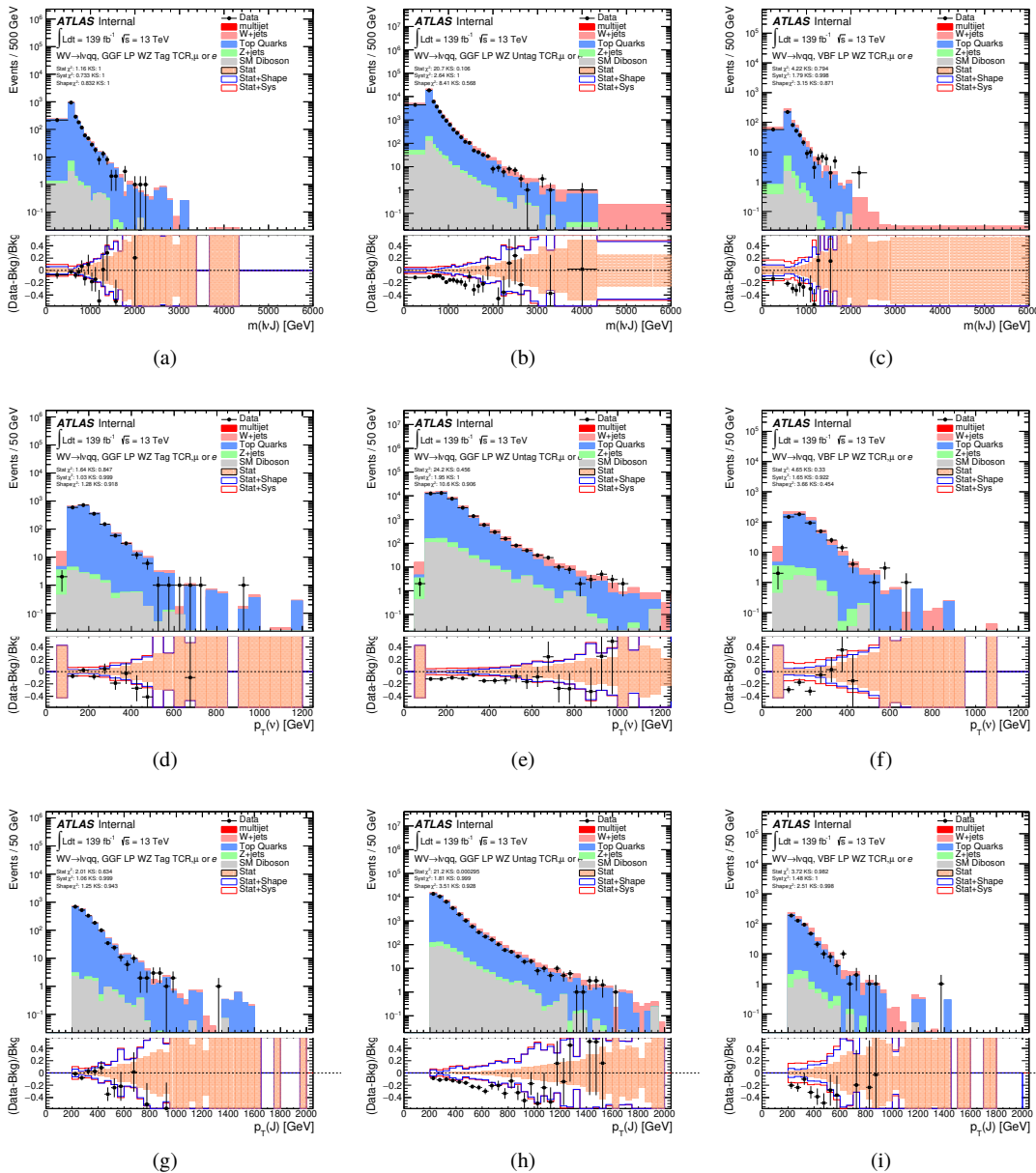


Figure 7.7: Data MC comparison for the merged  $WW$  LP TCR.



**Figure 7.8:** Data MC comparison for the merged  $WZ$  HP TCR.



**Figure 7.9:** Data MC comparison for the merged  $WZ$  LP TCR.

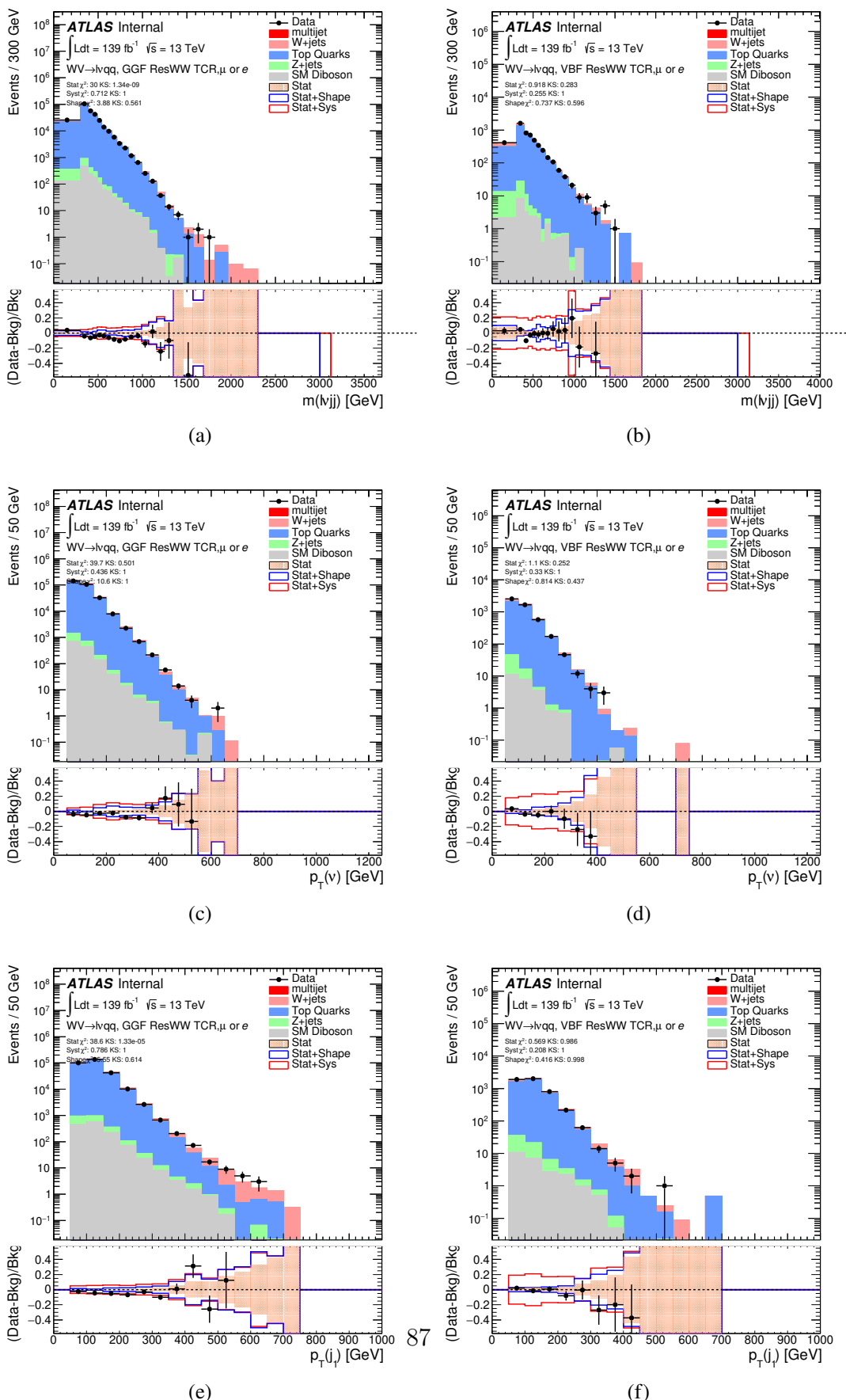


**Figure 7.10:** Data MC comparison for the resolved  $WW$  TCR.

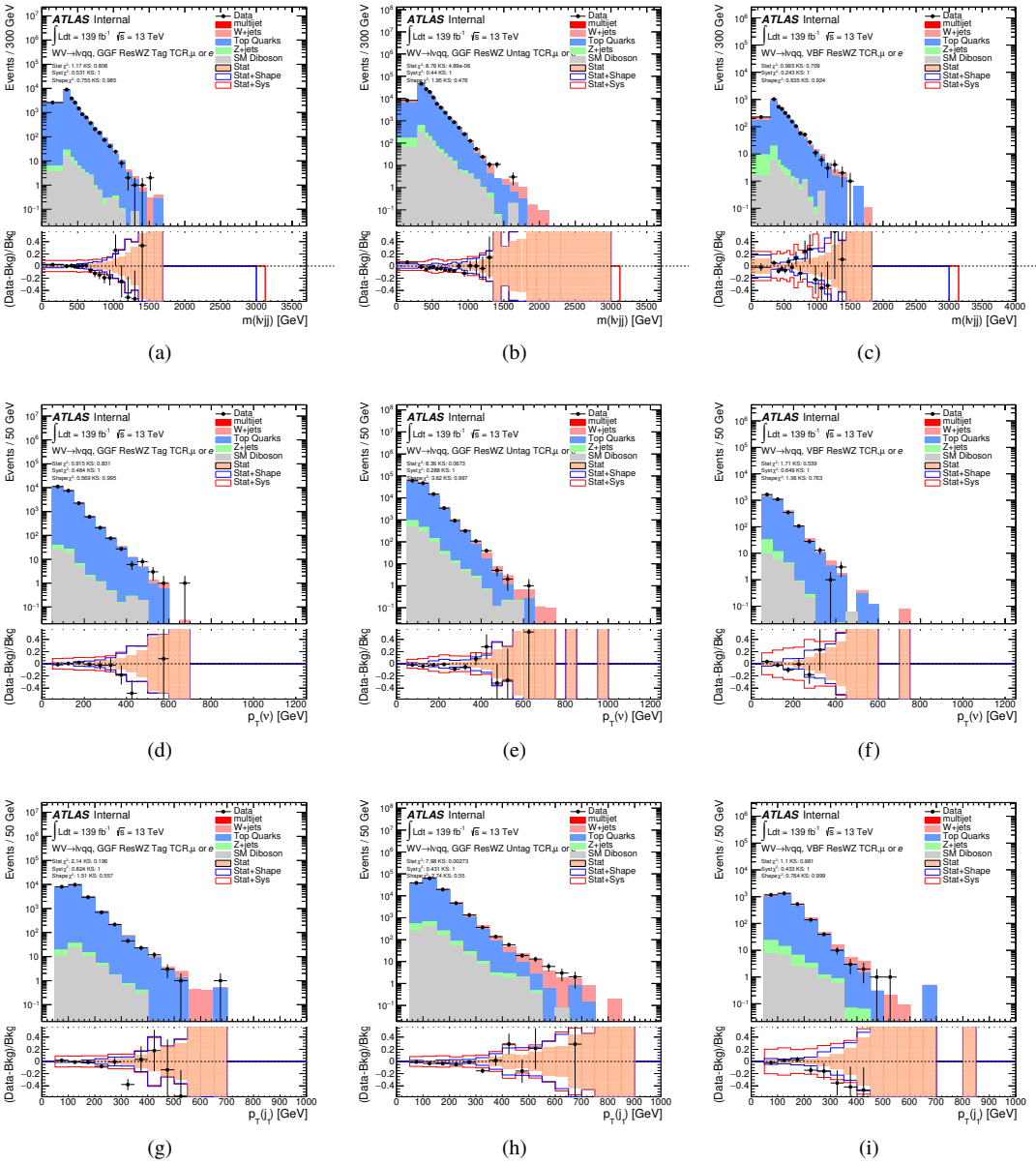


**Figure 7.11:** Data MC comparison for the resolved  $WZ$  TCR.

926 **7.5 Background Estimate**

927 **7.5.1 Multijet Sample**

928     Backgrounds in this analysis containing real leptons (e.g.  $W/Z+jets$ , diboson,  
929      $t\bar{t}$ , single- $t$ ) are well-modeled with simulated samples and constrained with data  
930     from CRs. However, the multijet background containing fake leptons is not well-  
931     modeled with simulation. For this reason, the multijet background is extracted  
932     from data. Heavy flavor decay products, jets, and converted photons can be  
933     mistakenly reconstructed as jets. Fake electrons often arise from jet fakes while  
934     fake muons may also arise from heavy flavor decay. For this analysis, these fake  
935     electrons generally fail the electron ID criteria and fake muons fail the muon  
936     isolation requirement. Therefore, to derive the multijet template shape the SR  
937     and CR selections and inverted lepton requirements are used as seen in Table  
938     7.4. NB: by inverting the lepton isolation/identification criteria the CR and SRs  
939     created are orthogonal to the CR and SRs.

940     The template shape of the MJ background is determined by using a multijet  
941     validation region (MJVR) that requires the inverted lepton isolation/id require-  
942     ment and the two signal jets to satisfy the  $m_{jj}$  requirement used in the  $W+jets$   
943     CRs. The  $E_T^{miss}$  distribution in MJCR is shown in Figure 7.12 for 2017 data.  
944     The template is then extracted by subtracting the data in the MJVR from the  
945     electroweak background processes. This template is then added in the WCR  
946     and a "pre-MJ-fit" is preformed. In this fit the  $E_T^{miss}$  distribution is fit with the  
947     electroweak background normalizations constrained to expected ranges and the  
948     multijet electron and muon background normalizations free to float. The fitted  
949     scale factors from this MJVR template are then applied in the MJCR template.  
950     The fitted uncertainties on the MJCR normalizations are then used to create the

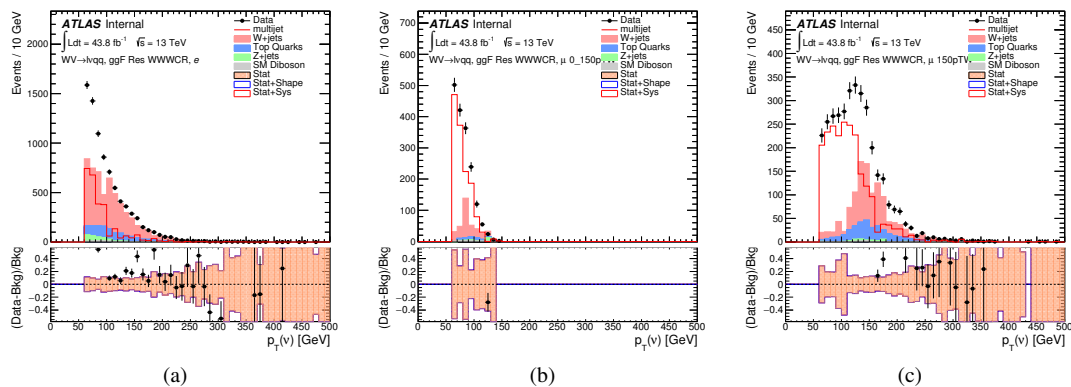
951 MJ template in the SRs. The electron and muon background normalizations are  
 952 parameters in the final simultaneous fit. Technically, there should be a separate  
 953 template for every CR and SR, but some MJ regions have insufficient statistics to  
 954 do this. Additionally, the shapes for the MJ templates for VBF and ggF regions  
 955 are found to be compatible within statistical uncertainty. Therefore, the sample  
 956 MJ template used for VBF and ggF CR/SRs, but with different pre-MJ-fit scale  
 957 factors.

958 This template method was validated using WCR and full Run 2 data. The  
 959 results of the fit are shown in Table 7.5. The multijet contribution in the muon  
 960 channel for  $p_T^W > 150$  GeV is consistent with zero, and therefore neglected in  
 961 the final fit. Applying the extracted normalization factor to MJVR in WCRs for  
 962 various kinematic variables such as  $E_T^{miss}$ ,  $W$  transverse mass, lepton  $p_T$ , and the  
 963 invariant mass as show in Figures 7.13 -7.22. These figures show good agreement  
 964 between the data and background estimate.

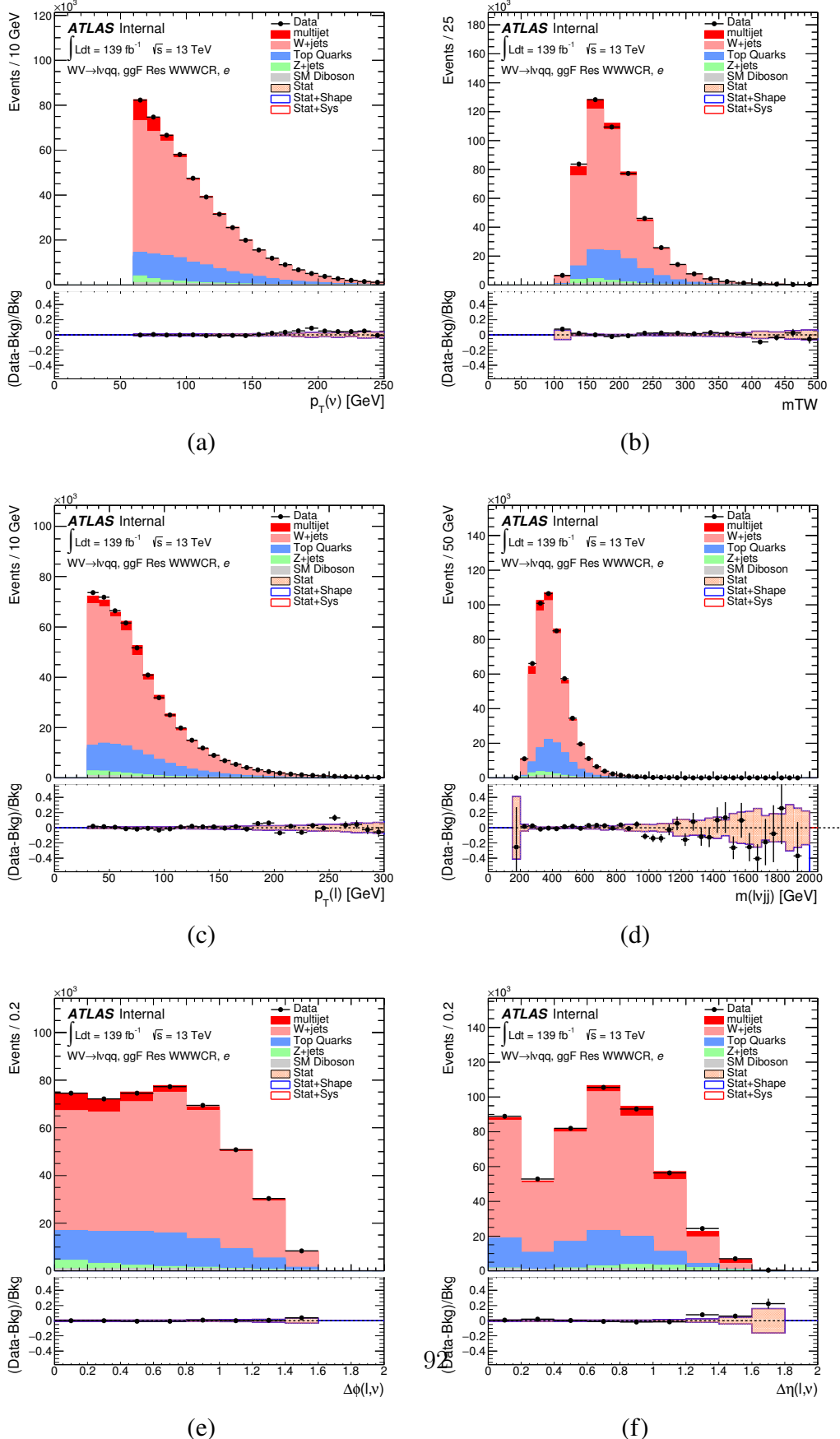
	Criterion	signal lepton	inverted lepton
Electron	ID	TightLH	MediumLH !TightLH
	Calo Isolation	FixedCutHighPtCaloOnlyIso	FixedCutHighPtCaloOnlyIso
Muon	ID	WHSignalMuon	WHSignalMuon
	Track Isolation	FixedCutTightTrackOnlyIso	!FixedCutTightTrackOnlyIso $ptvarcone30/pt < 0.07^*$
*Only applied to events with $pTW < 150\text{GeV}$			

**Table 7.4:** Definitions of “inverted” leptons used in multijet control region

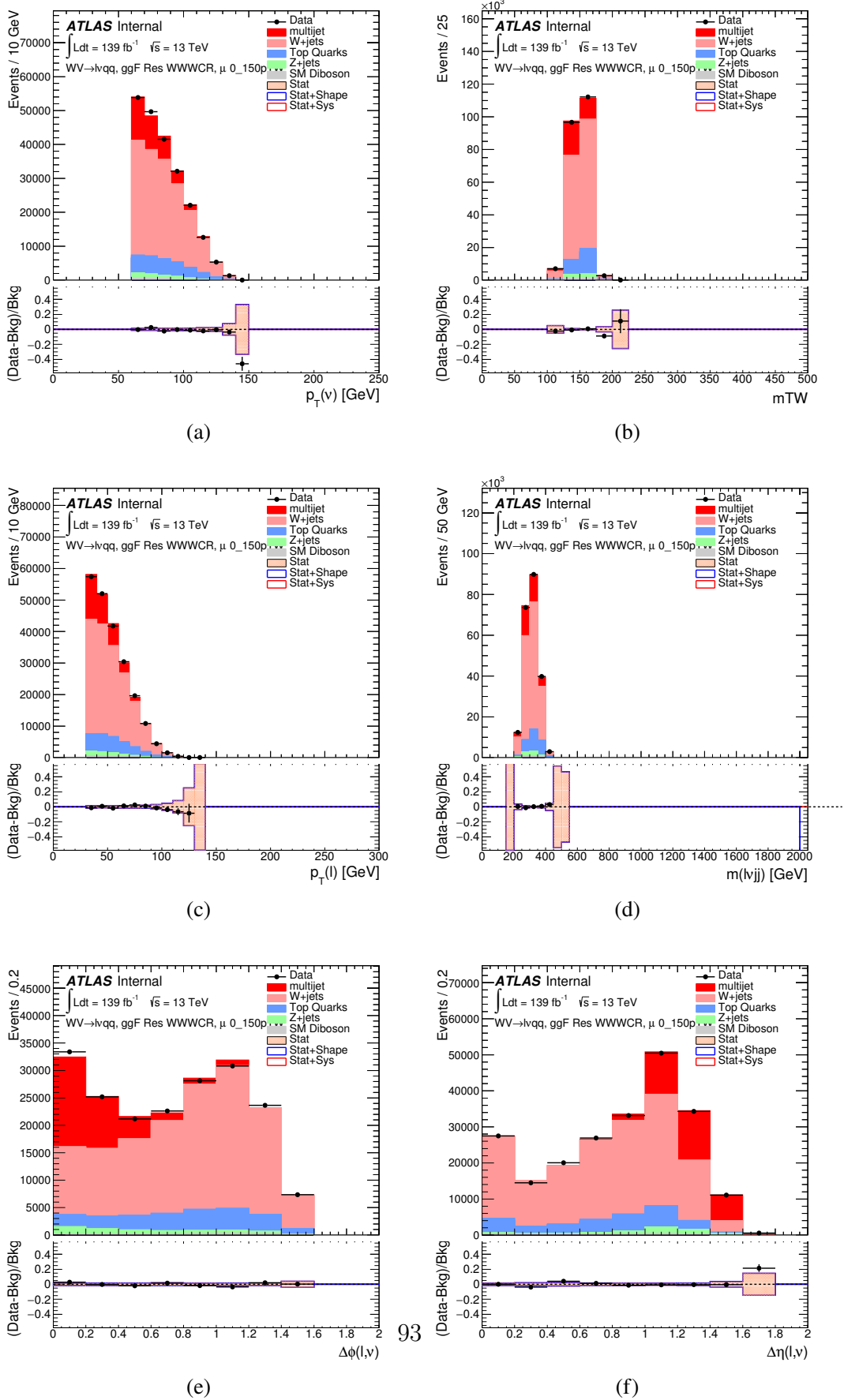
965



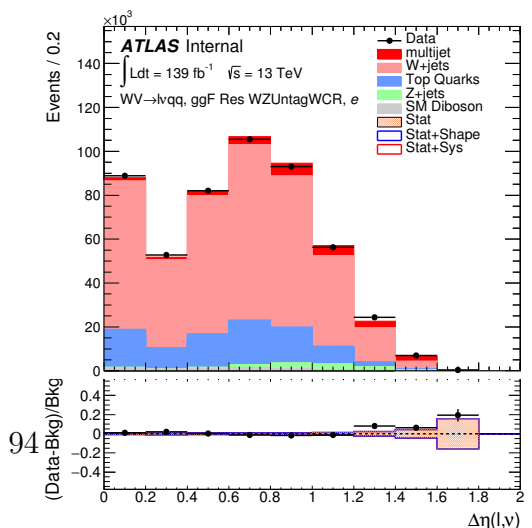
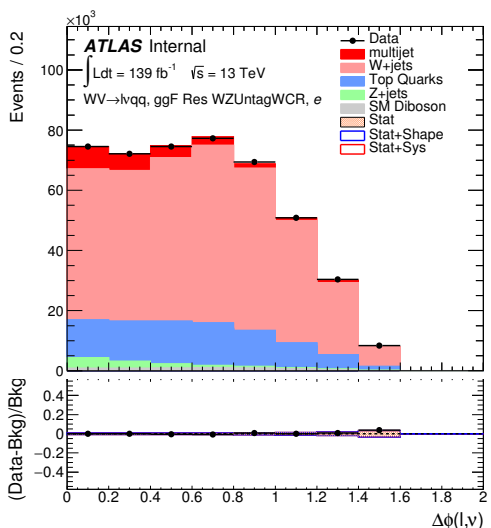
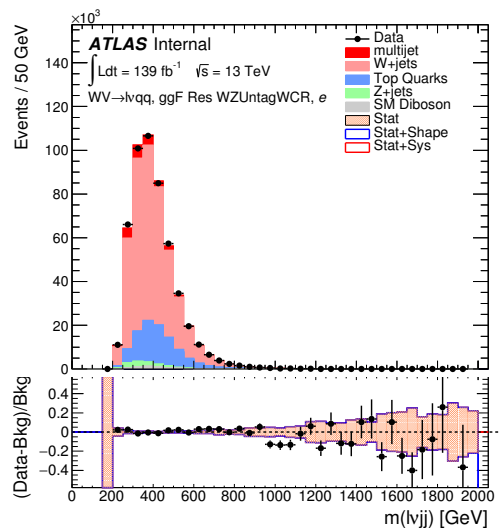
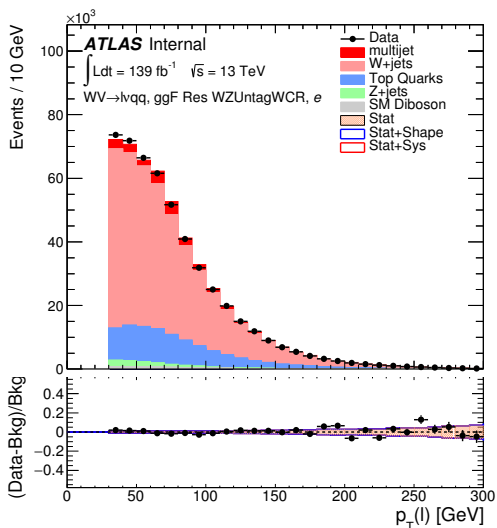
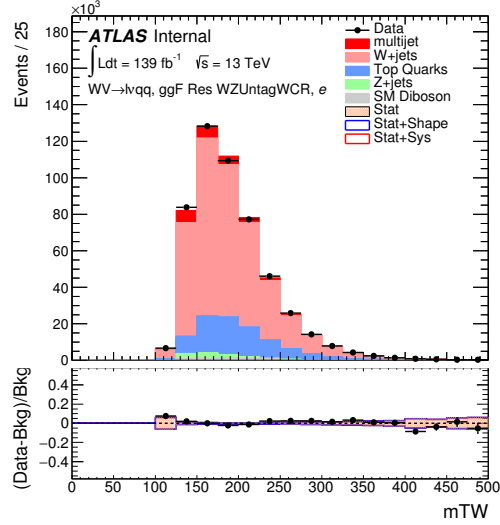
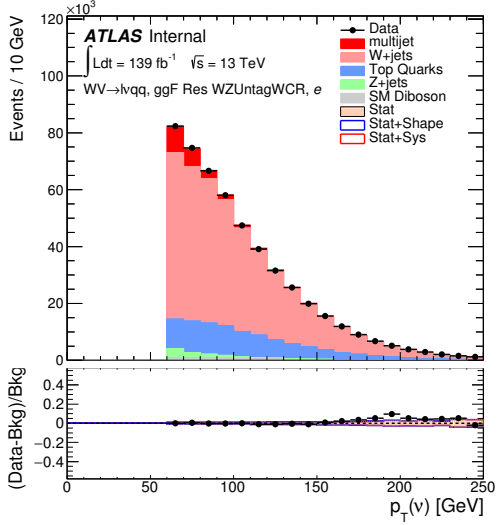
**Figure 7.12:** The  $E_T^{miss}$  distribution in MJCR for 2017 data in the electron channel(left), muon channel with W-boson pT < 150 GeV (center) and > 150 GeV (right). Multi-jet templates are calculated as remaining data components after excluding known MC



**Figure 7.13:** Postfit Data/MC comparison of distributions of  $E_T^{miss}$ ,  $m_T^W$ , lepton



**Figure 7.14:** Postfit Data/MC comparison of distributions of  $E_T^{miss}$ ,  $m_T^W$ , lepton and neutrino  $p_T$ ,  $m_{l\nu jj}$ , lepton- $\nu$  angular distance in the  $WW$  muon channel. The distributions are shown for the  $WW \rightarrow l\nu qq, ggF$  resonance selection with  $\mu_0 < 150\text{ GeV}$ .



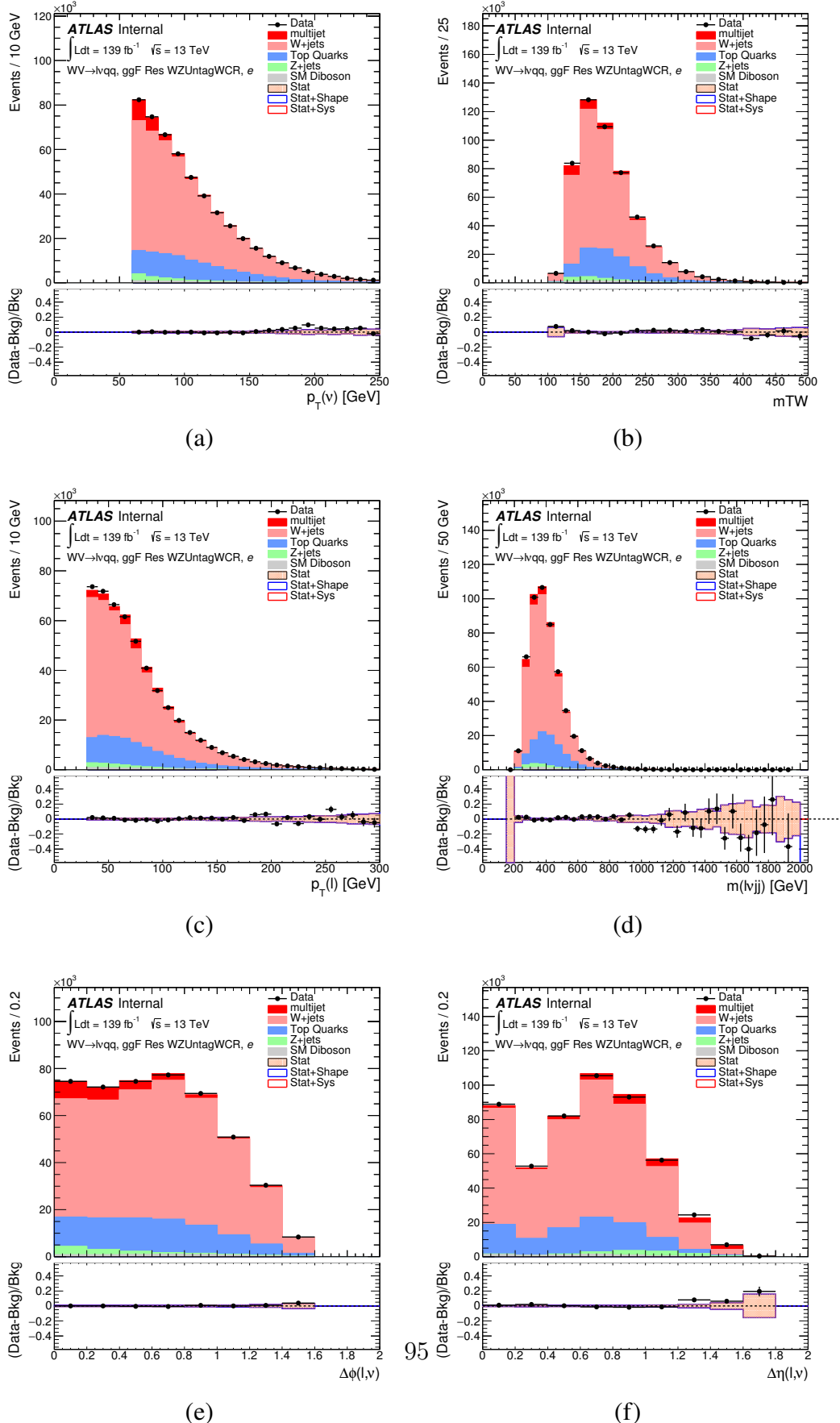
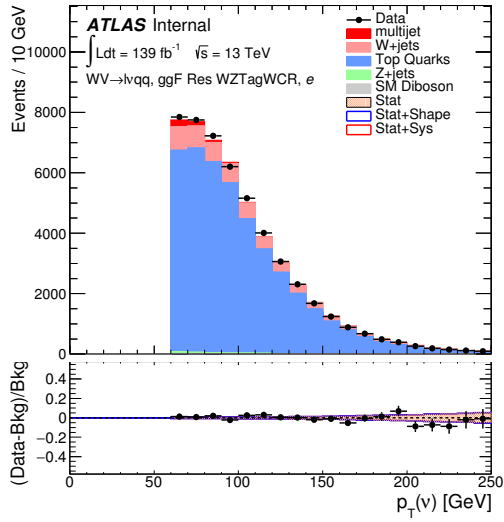
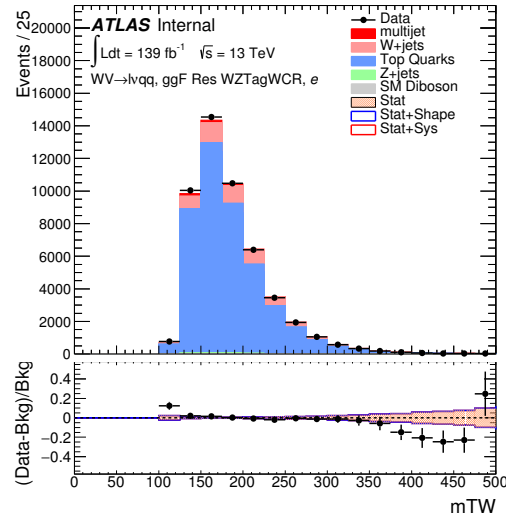


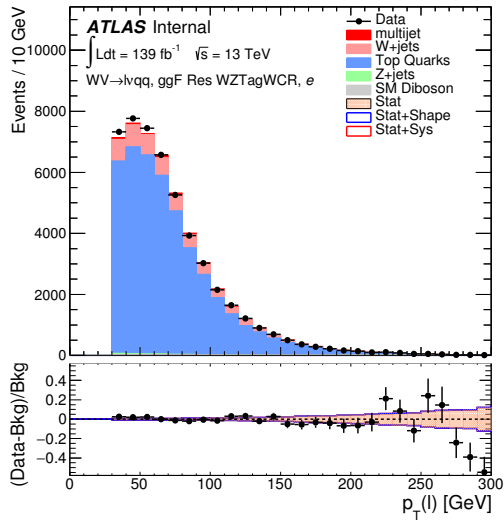
**Figure 7.16:** Postfit Data/MC comparison of distributions of  $E_T^{miss}$ ,  $m_T^W$ , lepton



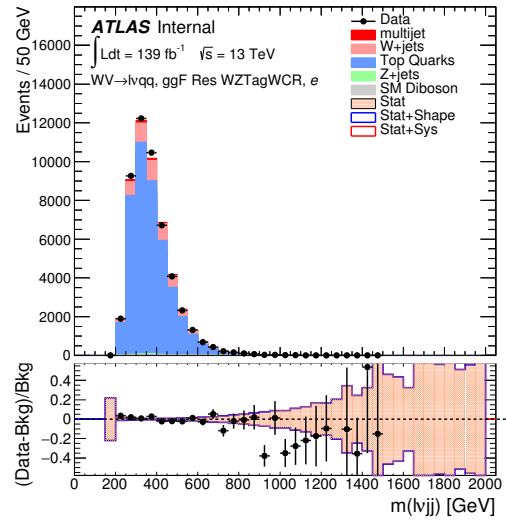
(a)



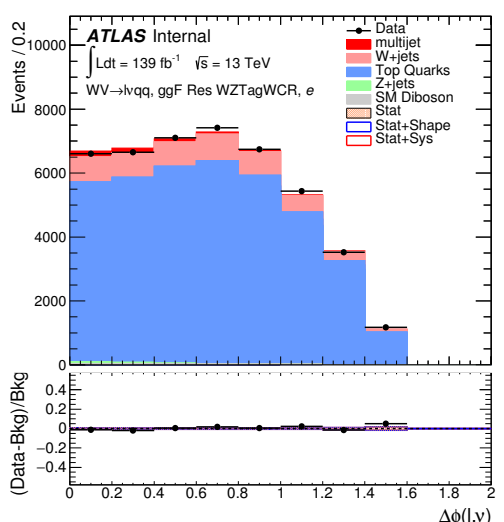
(b)



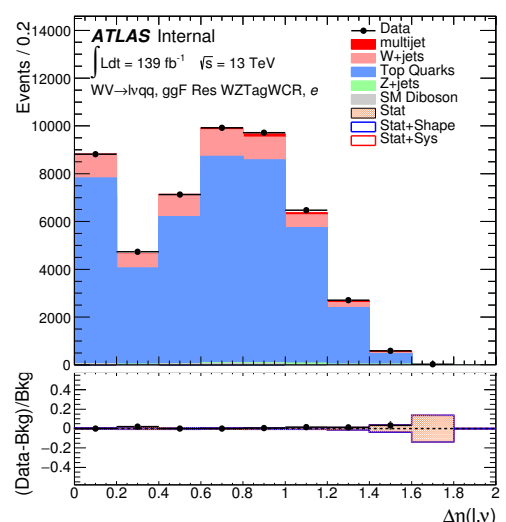
(c)



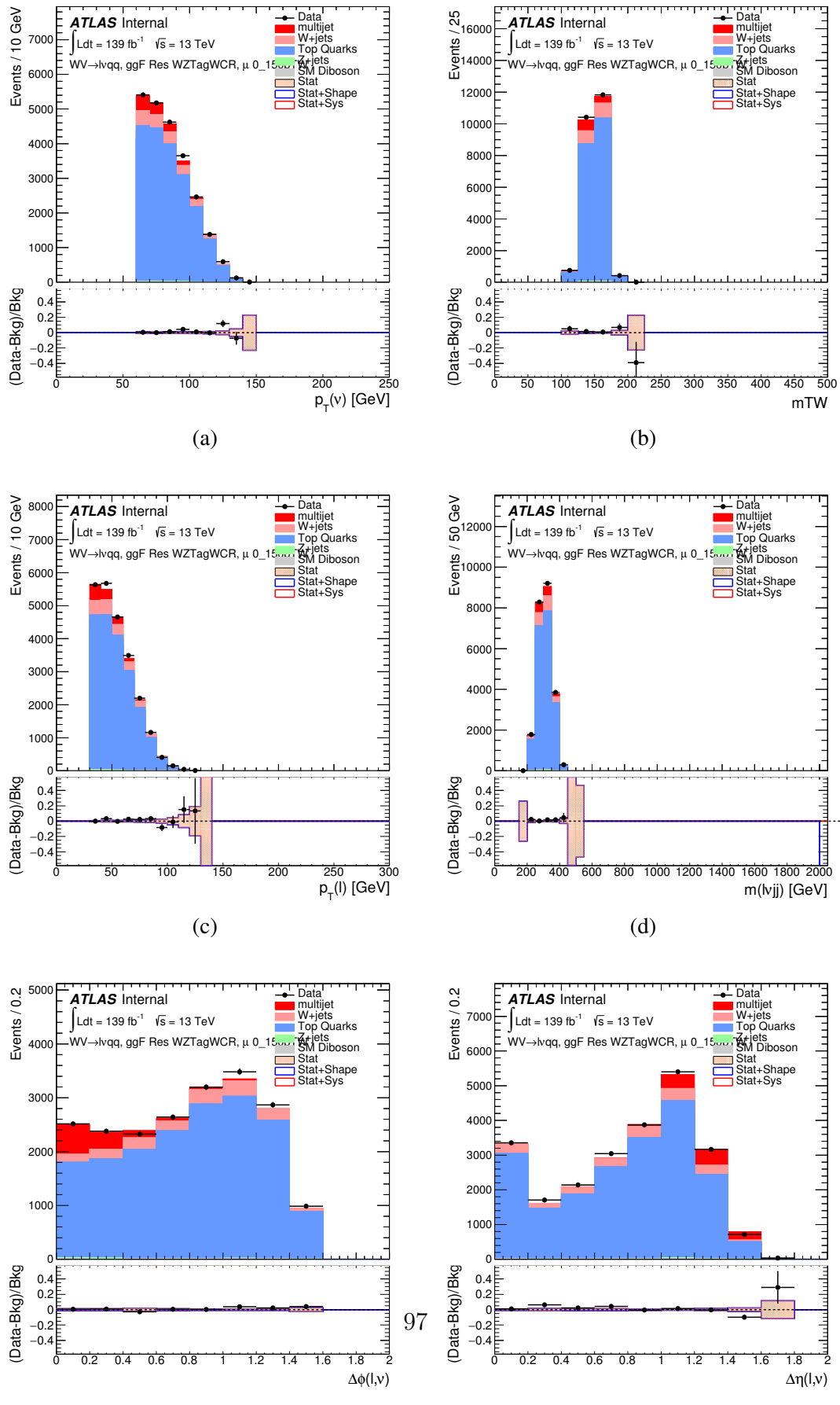
(d)

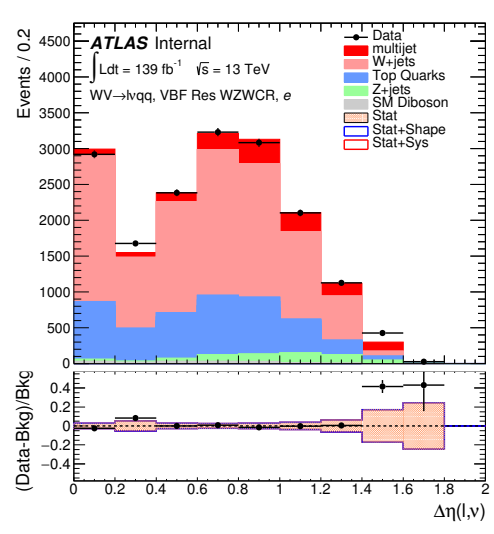
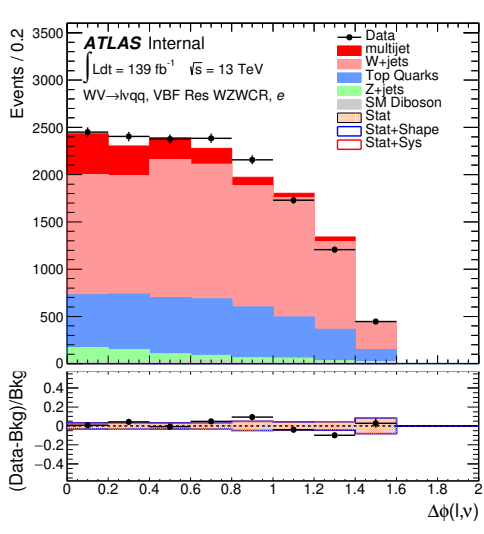
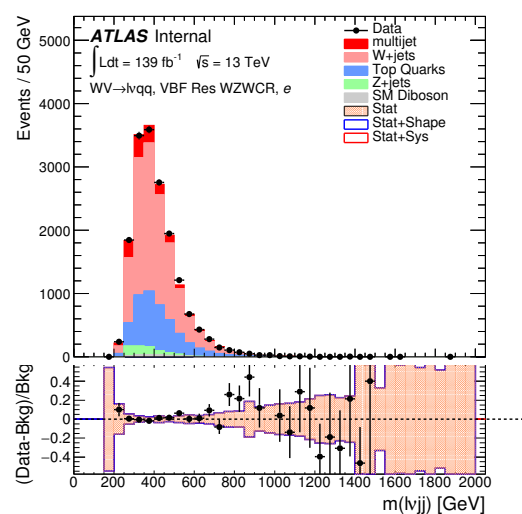
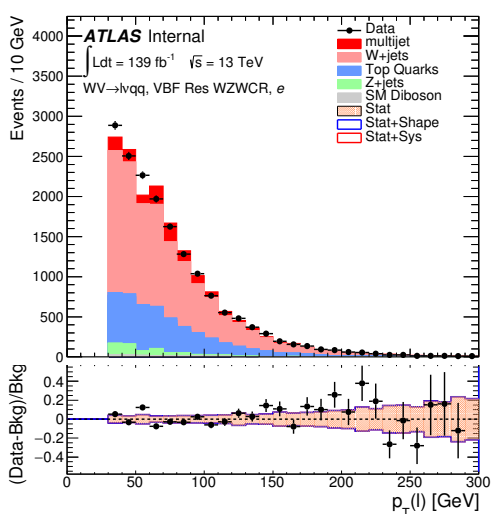
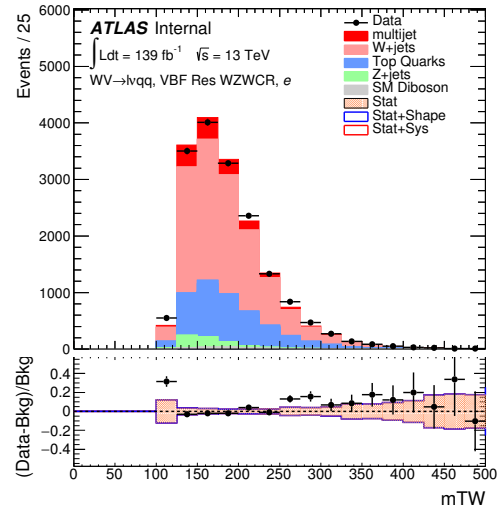
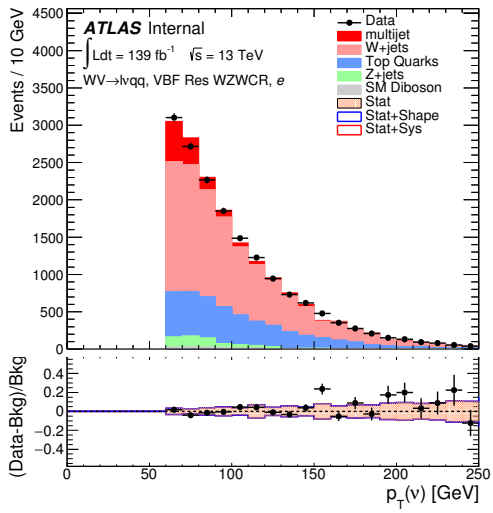


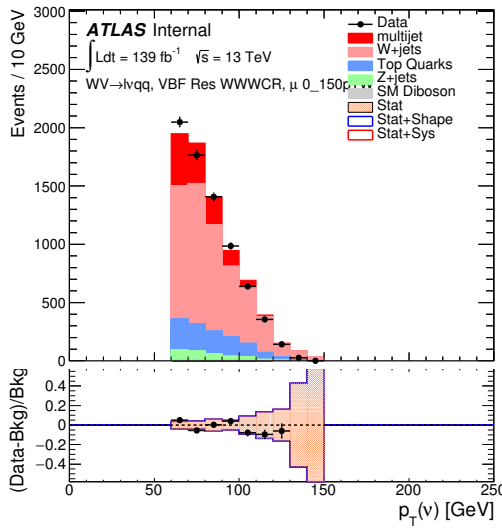
(e)



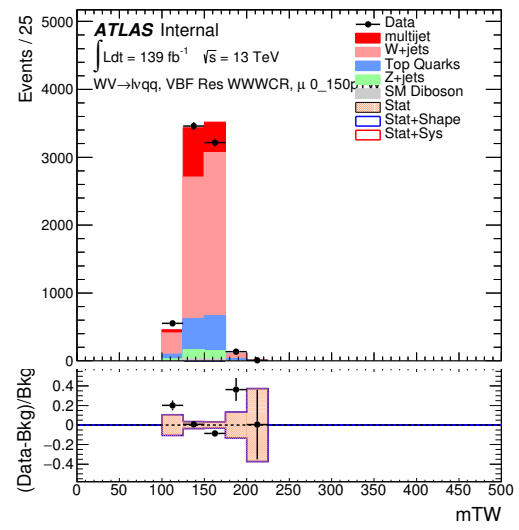
(f)



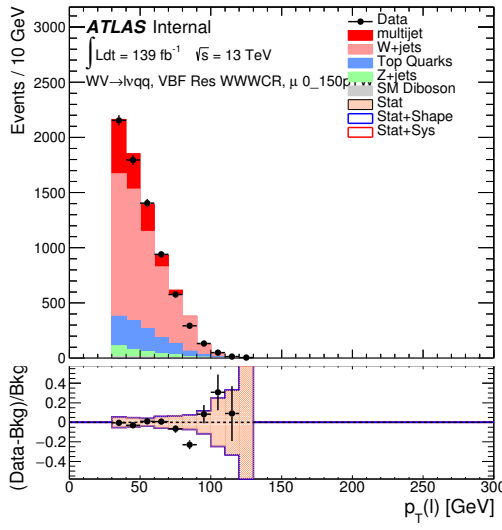




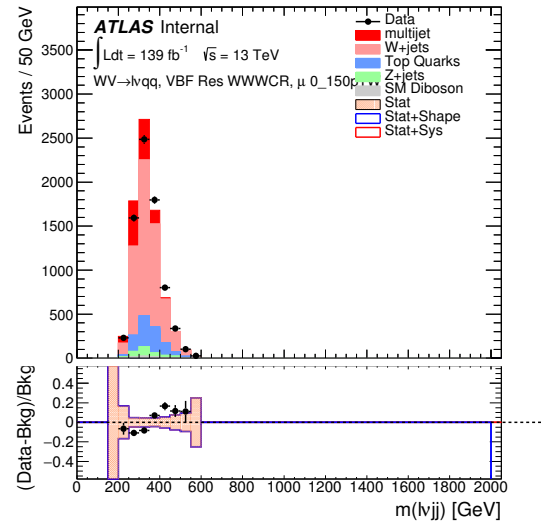
(a)



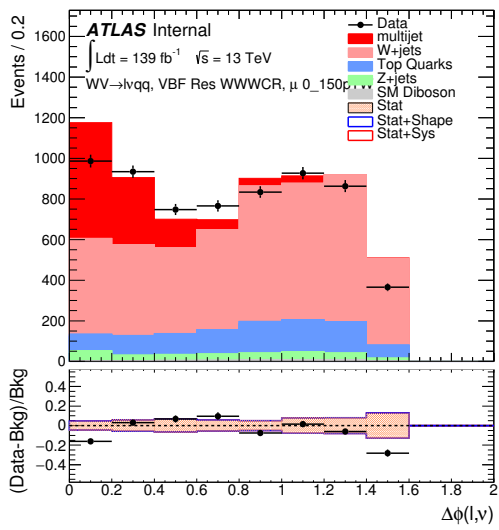
(b)



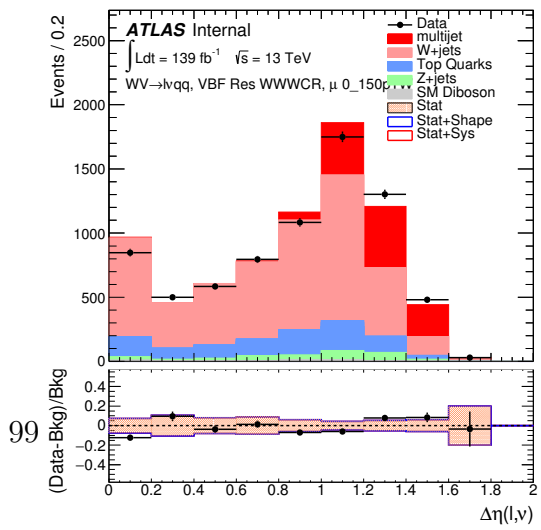
(c)



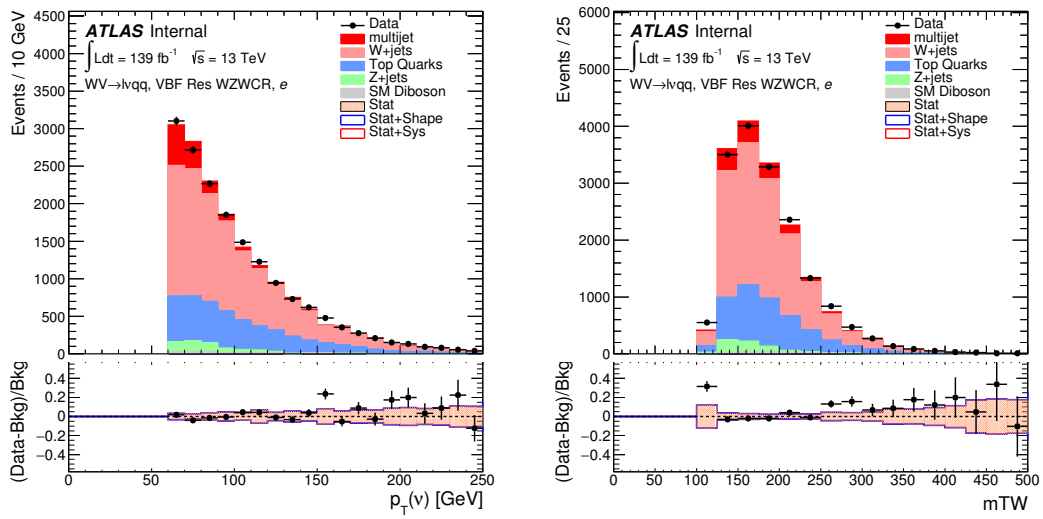
(d)



(e)

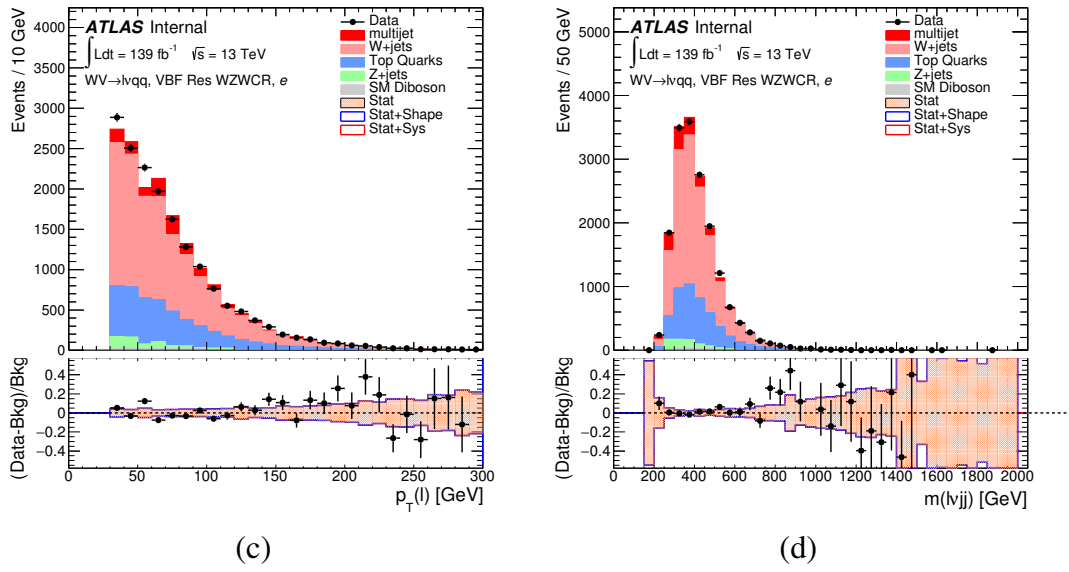


(f)



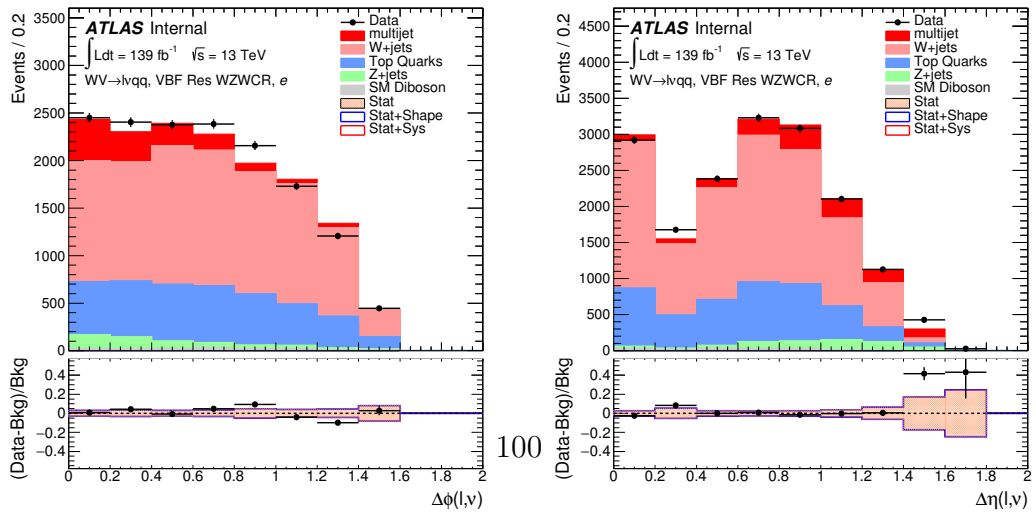
(a)

(b)



(c)

(d)



(e)

(f)

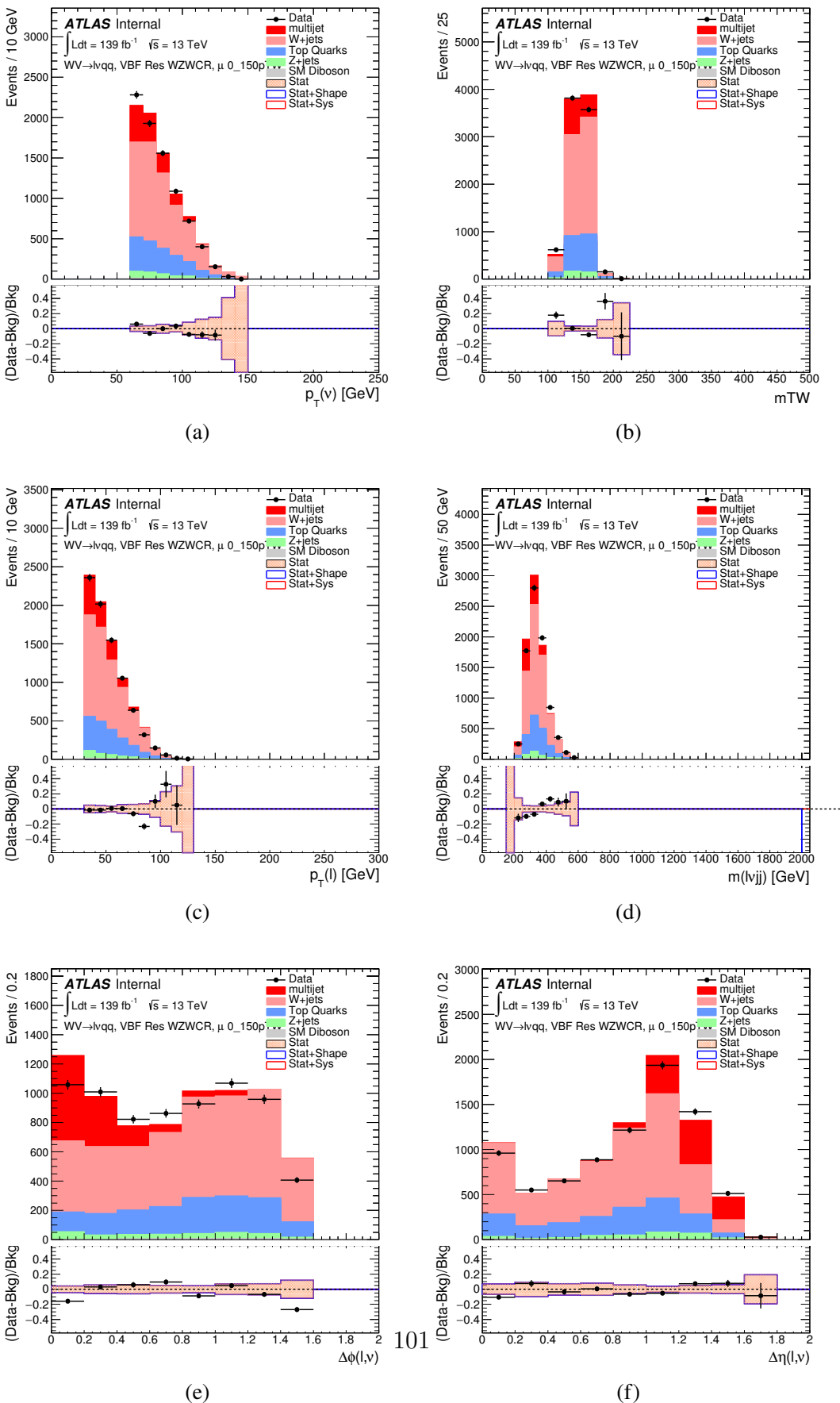


**Figure 7.22:** Postfit Data/MC comparison of distributions of  $E_T^{miss}$ ,  $m_T^W$ , lepton

Full Run 2  
ggF Res WWWCR

Sample	Yield	R.U.	SF
Top&W	$645040 \pm 1971.68$	0.31%	0.998
Z&VV	24075.9		fixed
MJ_el	$24156.3 \pm 1224.62$	5.06%	3.973
MJ_mu	$35528.5 \pm 923.94$	2.60%	9.019

ggF Res WZ01bWCR

Sample	Yield	R.U.	SF
Top&W	$644690 \pm 1981.4$	0.31%	0.997
Z&VV	24075.9		fixed
MJ_el	$24366.5 \pm 1232.69$	5.05%	3.874
MJ_mu	$35528.5 \pm 921.27$	2.58%	8.746

ggF Res WZ2bWCR

Sample	Yield	R.U.	SF
Top&W	$71236.5 \pm 688.74$	0.97%	1.031
Z&VV	518.5		fixed
MJ_el	$595.63 \pm 449.34$	75.44%	0.094
MJ_mu	$1196.9 \pm 222.13$	18.56%	0.294

VBF Res WWWCR

Sample	Yield	R.U.	SF
Top&W	$19032.3 \pm 364.43$	1.91%	0.928
Z&VV	1091.63		fixed
MJ_el	$1425.73 \pm 214.42$	15.03%	0.235
MJ_mu	$1281.36 \pm 157.21$	11.83%	0.314

VBF Res WZWCR

Sample	Yield	R.U.	SF
Top&W	$21341.8 \pm 392.21$	1.84%	0.942
Z&VV	1111.75		fixed
MJ_el	$1413.76 \pm 230.36$	16.29%	0.225
MJ_mu	$1281.36 \pm 157.21$	12.27%	0.314

**Table 7.5:** Fit validation result in WCRs for 2015+16 data. The fit is done in various WCRs, in order to obtain the corresponding scale factors for MJ templates: ggF resolved WCR for the  $WW \rightarrow lvqq$  selection, ggF resolved untagged WCR for the  $WZ \rightarrow lvqq$  selection, ggF resolved tagged WCR for the  $WZ \rightarrow lvqq$  selection, VBF resolved WCR for the  $WW \rightarrow lvqq$  selection, and VBF resolved WCR for the  $WZ \rightarrow lvqq$  selection. Post-fit event yields for electroweak processes and MJ contributions are shown. The SF column shows the corresponding normalization scale factors for electroweak processes from the fit. R.U. stands for relative uncertainty.

966 **Chapter 8**

967 **Systematic Uncertainties**

968 This section describes the sources of systematic uncertainties considered in  
969 this analysis. These uncertainties are divided into three categories: experimental  
970 uncertainties, background modeling uncertainties, and theoretical uncertainties on  
971 signal processes. In the statistical analysis each systematic uncertainty is treated  
972 as a nuisance parameter estimated on the  $m_{VV}$  distribution.

973 **8.1 Experimental Systematics**

974 The uncertainty on the integrated luminosity of the dataset used is 1.7% and  
975 a systematic in the final fit. The luminosity uncertainty is calculated following a  
976 methodology similar to the one in [ref P55].

977 Also, multiple pile up interactions are simulated to match data conditions.  
978 This ensures simulated detector response and particle reconstruction conditions  
979 are as similar as possible. The distribution of the average number of interactions  
980 per bunch crossing applied to simulation is called the  $\mu$  profile. The pileup mod-  
981 eling uncertainty is accounted for by re-weighting simulated events so the average  
982 number of interactions per bunch crossing varies within its uncertainty due to

983 systematics from vertex reconstruction [ref ATL-COM-SOFT-2015-119]. The as-  
984 sociated re-weighting factors are propagated through the entire analysis chain to  
985 construct a systematic uncertainty on  $m_{VV}$ .

986 The single-lepton and  $E_T^{miss}$  triggers used are not fully efficient and therefore  
987 simulated data must be scaled to account for trigger inefficiencies. Trigger effi-  
988 ciencies are given by the ratio of the distribution of offline objects before trigger  
989 selection and after trigger selection.

990 Uncertainties on small-R jet energy scale and resolution are measured in-situ  
991 by calculating the response between data and simulation. This analysis uses a  
992 reduced set of JES and JER uncertainties (totaling 30 and 8 systematics, re-  
993 spectively). These reduced sets of systematics are calculated using a principal  
994 component analysis, yield largely uncorrelated independent systematics. These  
995 uncertainties account for the dependence on  $p_T$ ,  $\eta$ ,  $\mu$ , flavor response and global  
996 sequential corrections. Systematic uncertainties associated with  $b$ -tagging are also  
997 considered. These systematics are evaluated as uncertainties on the scale factor  
998 which account for the difference in  $b$ -tagging efficiencies in data and MC, and the  
999 flavor dependence (between b, c, and light jets).

1000 The uncertainty on the  $p_T$  scale of the large-R jets is determined by comparing  
1001 the jet's  $p_T^{calo}$  to  $p_T^{track}$  in di-jet simulation and data. In addition to this uncertain-  
1002 ties from tracking, modeling (Pythia vs Herwig), and statistical constraints are  
1003 also calculated. The large-R jet  $p_T$  resolution is given by smearing the jet  $p_T$  with  
1004 a Gaussian with a 2% width.

1005 The  $W/Z$ -tagging efficiency cannot be evaluated using the Rtrk method as the  
1006 TCC algorithm uses track measurements to reconstruct jet substructure variables.  
1007 In order to avoid this potential bias, the  $W/Z$ -tagging estimated in data using a  
1008 control sample and correct by comparing it with simulation. The efficiency to

1009      $W/Z$ -induced signal is estimated by a  $t\bar{t}$  control sample, while the efficiency to  
1010     single- $q/g$  background is estimated using a dijet sample. The effects of experimen-  
1011     tal and theoretical uncertainties on the efficiency scale factor are by taking the  
1012     ratio of efficiencies in data and simulation. By taking this ratio the uncertainties  
1013     not arising for jet mass and  $D_2$  cancel.

1014       Lepton identification, reconstruction, isolation systematic uncertainties are de-  
1015       termined by reconstructing the Z mass peak with a tag and probe method. The  
1016       lepton energy and momentum scales are also measured with the Z mass peak.  
1017       Additionally, the track-to-vertex association efficiency is used for muons.

1018       As  $E_T^{miss}$  is calculated using all the physics objects in the event, all those objects  
1019       associated errors result in an uncertainty on  $E_T^{miss}$ . Additionally, the unassociated  
1020       tracks used to construct  $E_T^{miss}$  contribute to the uncertainty on  $E_T^{miss}$ .

## 1021     **8.2 Theory Systematics**

1022       Theoretical uncertainties for signal and background processes arise from un-  
1023       certainties in the parameters used in Monte Carlo simulation. In particular for  
1024       the  $t\bar{t}$ ,  $W/Z+jets$ , and diboson backgrounds and signal samples the QCD scale,  
1025       PDF, generator and hadronization uncertainties were evaluated. To assess the  
1026       QCD scale uncertainty the renormalization and factorization scales were scaled  
1027       up (2.0) and down (0.5) at the event generation stage of sample production. Un-  
1028       certainties due to the choice of the parton distribution functions were evaluated  
1029       by re-weighting samples from the nominal PDF to a set of error PDFs which ac-  
1030       count for the uncertainty of the fits used to produce the PDF set. In addition to  
1031       this samples are re-weighted to different PDF sets to account for the arbitrariness  
1032       of the PDF choice. The difference between the  $m_{WV}$  distributions using differ-  
1033       ent event generators is assessed by comparing samples generated with different

1034 generators. Similarly, the uncertainty in hadronization models is account for by  
1035 comparing samples created using different hadronization models (e.g. Pythia8 vs.  
1036 Herwig7). Figures 8.2 - 8.8 show the impact of these uncertainties on the  $t\bar{t}$  and  
1037  $W/Z + \text{jets}$  backgrounds.

1038 Additionally, contributions to the diboson background for the VBF analysis  
1039 were included in [SOME WAY that is not determined yet].

1040 The normalization of the  $t\bar{t}$  and  $W+\text{jets}$  processes impact the multijet template  
1041 shape. The impact of these normalization is assess by including a shape systematic  
1042 on the multijet background from varying the  $t\bar{t}$  and  $W+\text{jets}$  normalization factors.

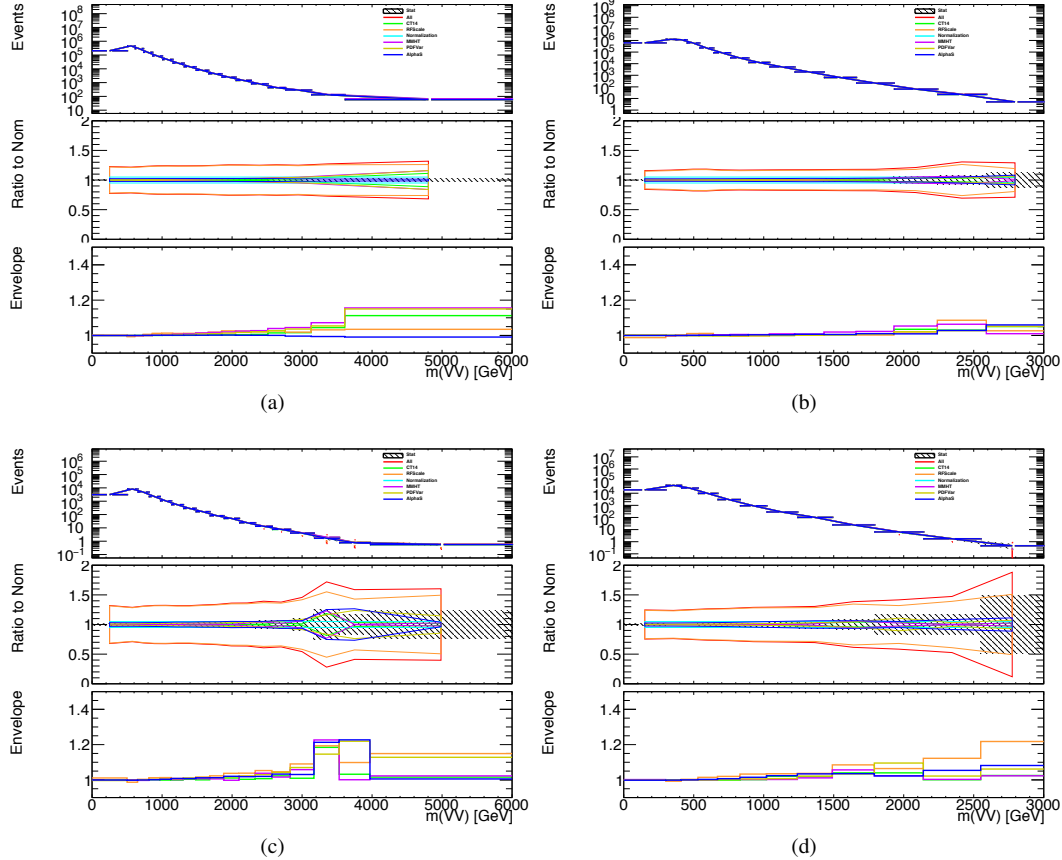


**Figure 8.1:** The  $W/Z + \text{jet}$  systematics for the a) Merged ggF, b) Resolved ggF, c) Merged VBF, and d) Resolved VBF regions. The top subplot shows the nominal and variation distributions/bands, the middle shows the ratio of the two, and the final shows just the shape of the envelope (the final uncertainty).

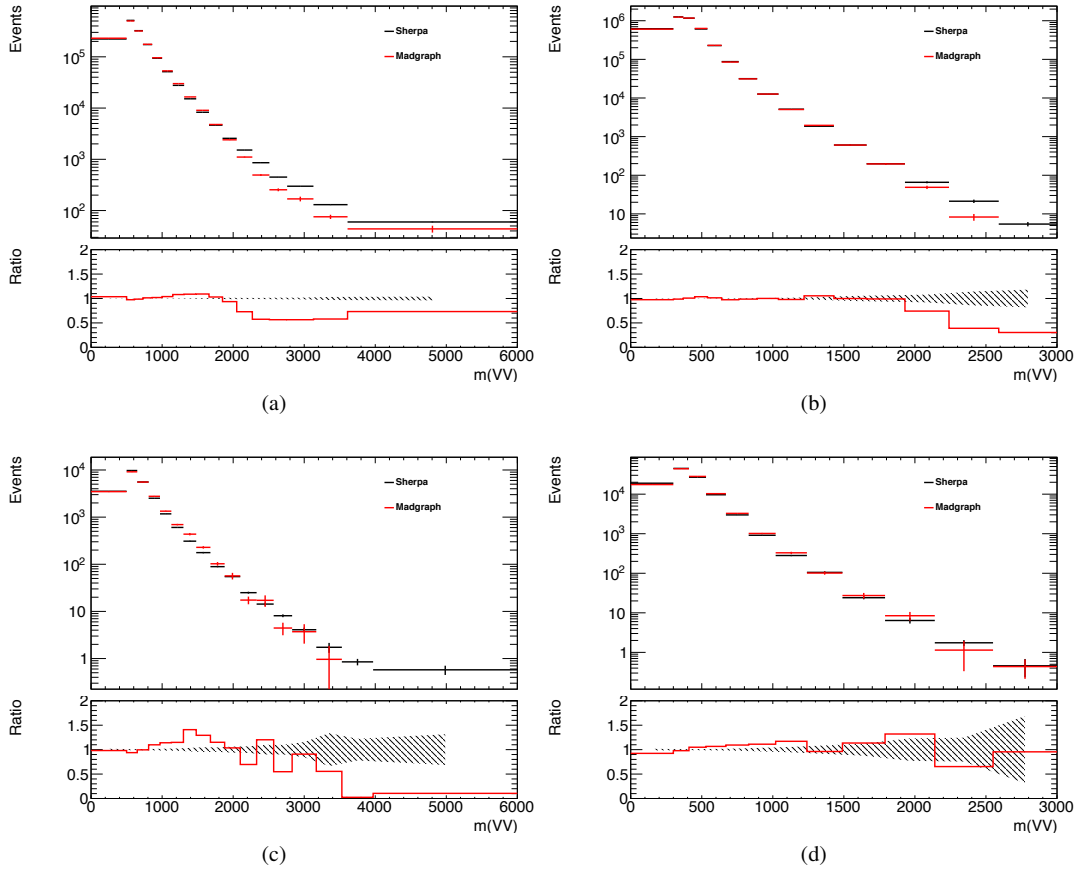


**Figure 8.2:** The two-point generator comparison between Sherpa and MadGraph for the  $W/Z + \text{jet}$  samples in the a) Merged ggF, b) Resolved ggF, c) Merged VBF, and d) Resolved VBF regions. The normalization of the Madgraph sample is set to the Sherpa value to consider only shape effects. The bottom inset shows the ratio of the two.

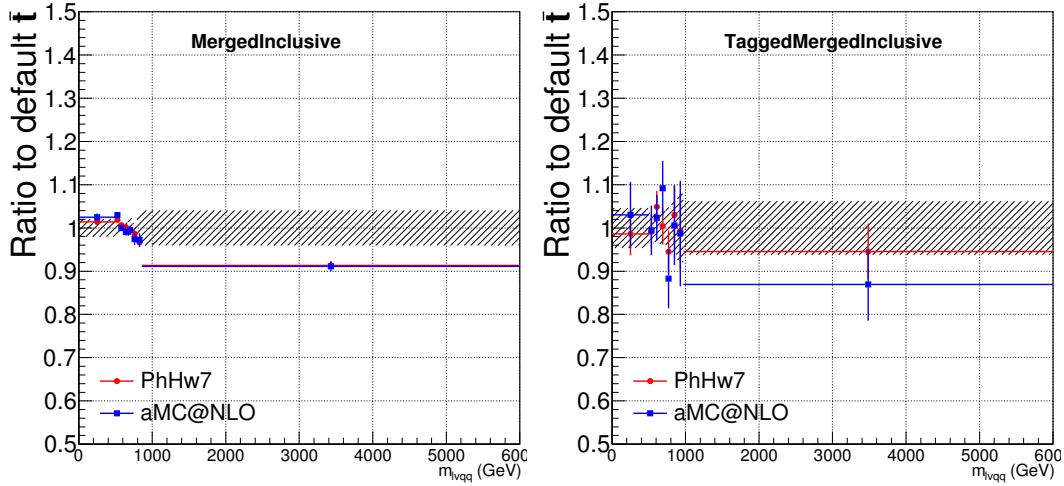


**Figure 8.3:** Ratio between the variations of generator (red) and hadronization (blue) variations for the Merged regime for  $t\bar{t}$  sample.

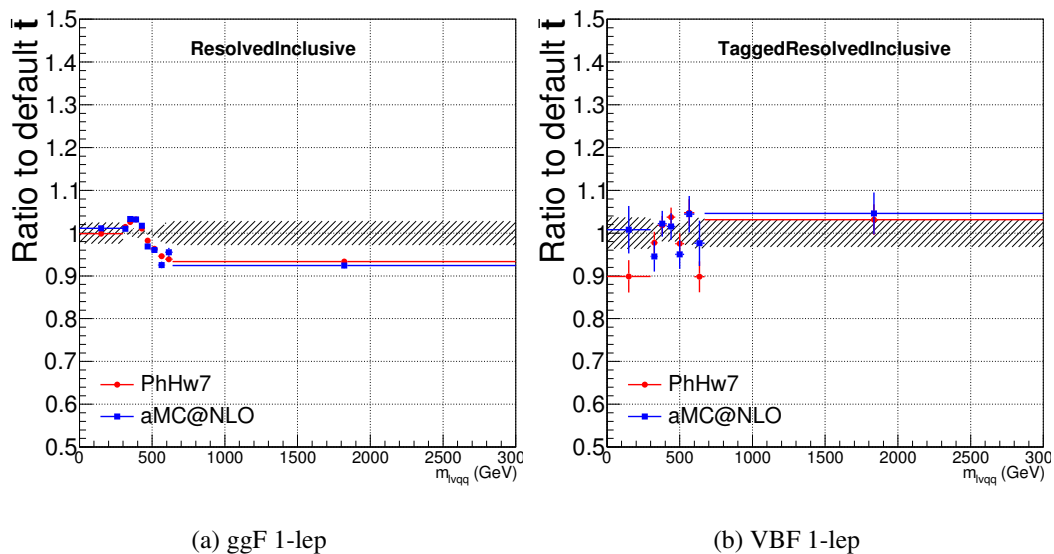


**Figure 8.4:** Ratio between the variations of generator (red) and hadronization (blue) variations for the Resolved regime for  $t\bar{t}$  sample.

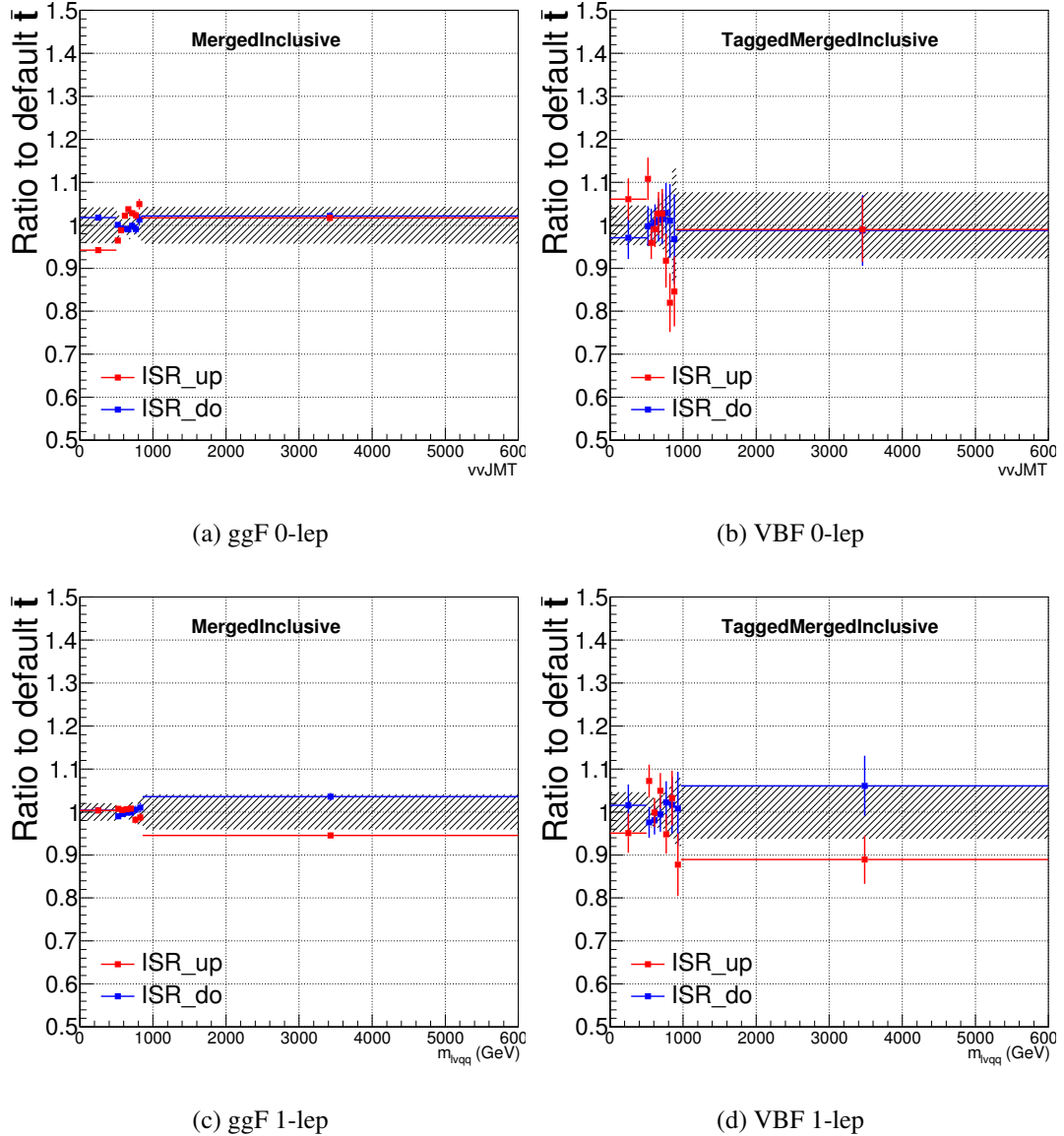


**Figure 8.5:** Ratio between the variations of ISR up (red) and down (blue) variations for the Merged regime for  $t\bar{t}$  sample.

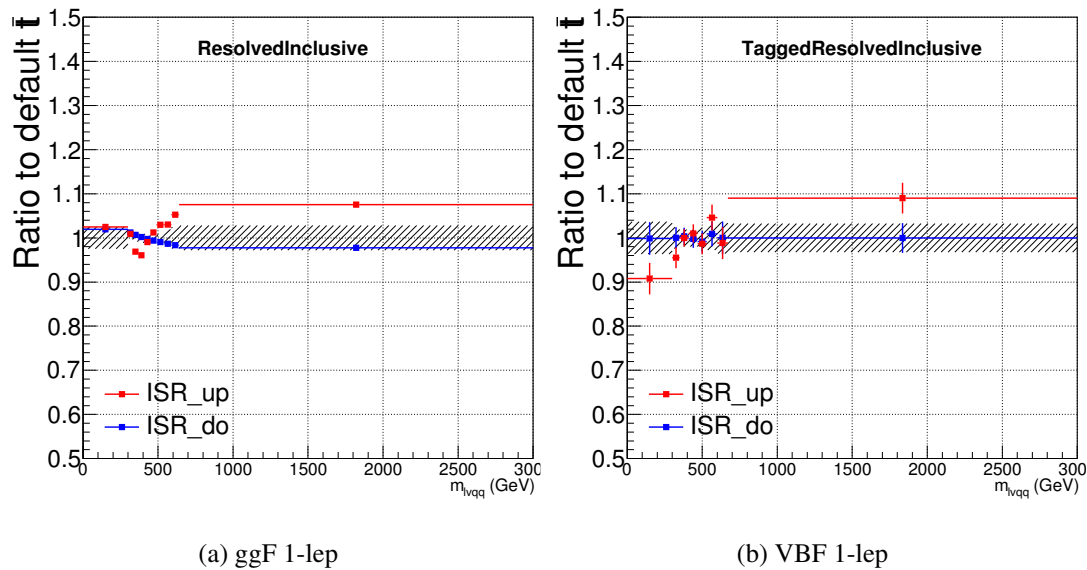


**Figure 8.6:** Ratio between the variations of ISR up (red) and down (blue) variations for the Resolved regime for  $t\bar{t}$  sample.

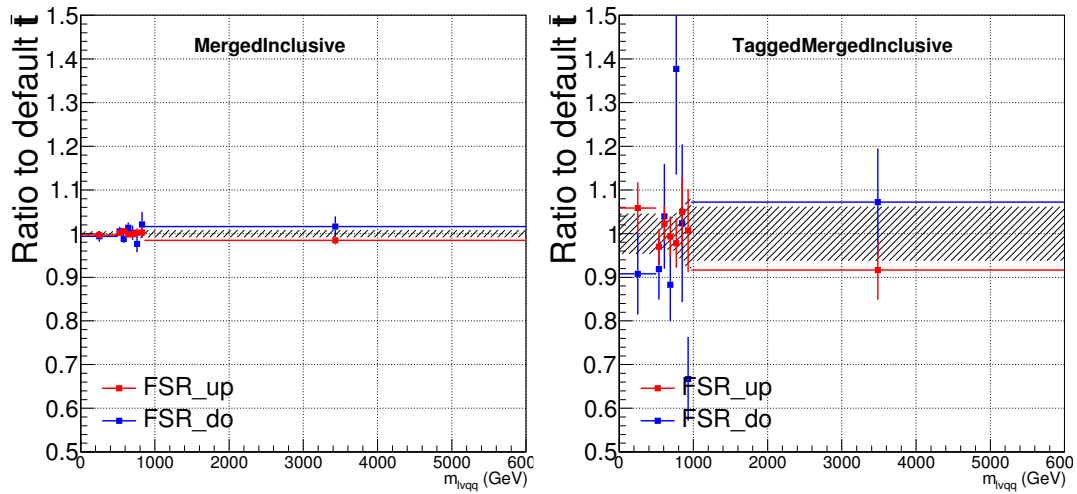


**Figure 8.7:** Ratio between the variations of FSR up (red) and down (blue) variations for the Merged regime for  $t\bar{t}$  sample.

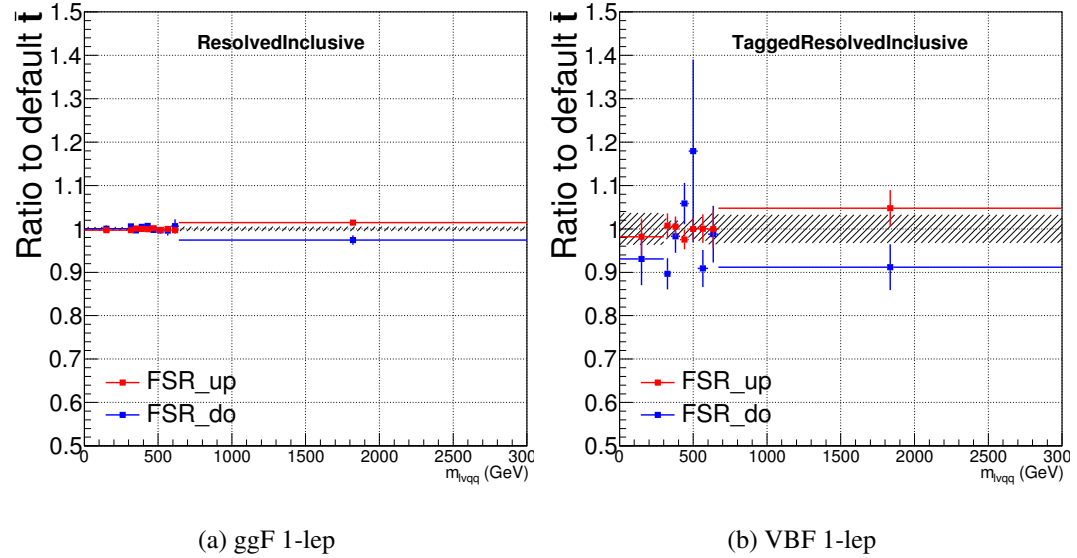


**Figure 8.8:** Ratio between the variations of FSR up (red) and down (blue) variations for the Resolved regime for  $t\bar{t}$  sample.

1043 **Chapter 9**

1044 **Statistical Analysis**

1045 To determine the compatibility of the data collected with the proposed reso-  
1046 nances a statistical procedure based on a likelihood function is used. A discovery  
1047 test is used to measure the compatibility of the observed data with the back-  
1048 ground only hypothesis. If the observed data is sufficiently incompatible with the  
1049 background only hypothesis, this could indicate a discovery. In the absence of  
1050 discovery, upper limits on the signal strength parameter,  $\mu$ , are assessed using the  
1051 CLs method.

1052 **9.1 Likelihood Function Definition**

1053 The likelihood function is product of Poisson probabilities for all analysis bins  
1054 and systematic constraints:

$$\mathcal{L}(\mu, \boldsymbol{\theta}) = \prod_c \prod_i \frac{(\mu s_{ci}(\boldsymbol{\theta}) + b_{ci}(\boldsymbol{\theta}))^{n_{ci}}}{n_{ci}!} e^{-(\mu s_{ci}(\boldsymbol{\theta}) + b_{ci}(\boldsymbol{\theta}))} \prod_k (\theta'_k | \theta_k) \quad (9.1)$$

1055 Here  $c$  are the analysis channels considered and  $i$  runs over all the  $m_{\ell\nu qq}$  bins  
1056 used in the fit. The signal strength parameter,  $\mu$ , multiplies the expected signal

yield in each analysis bin,  $s_{ci}$ . The background content for channel  $c$  and bin  $i$  is given by  $b_{ci}$ . The dependence of signal and background predictions on systematic uncertainties is described by the aforementioned set of nuisance parameters  $\boldsymbol{\theta}$ , which are parameterized by Gaussian or log-normal priors denoted here as  $\theta_k$ . Statistical uncertainties of the simulated bin contents are also included as systematic uncertainties. Most systematics are correlated among all the analysis regions and considered to be independent from each other. The validity of this assumption is checked by evaluating the covariance of nuisance parameters.

## 9.2 Fit Configuration

The binning of  $m_{\ell\nu qq}$  in the likelihood fit is determined by the statistical uncertainty of signal mass width. For each signal mass point, the signal mass resolution is given by the fitted Gaussian width of the  $m_{\ell\nu qq}$ . The fitted signal widths are then fit to a line to give a parameterized signal mass width, as shown in Figures 9.1 and 9.2. Bin widths are set first to this parameterized signal mass resolution. Then if the statistical uncertainty of the data or simulated background is more than 50%, bins are merged until the statistical uncertainty is less than 50%.

For this analysis, each signal model fits the Merged and Resolved channels for the relevant signal production mode simultaneously. The control regions are used to extract  $W + \text{jets}$  and  $t\bar{t}$  backgrounds normalizations in the signal regions.

Systematics may be affected by low statistics, leading to unsmooth  $m_{VV}$  distributions with unphysically large fluctuations. This can lead to artificial pulls and constraints in the fit. To remove such issues a multi-step smoothing procedure is applied to all systematic variation distributions in all regions. First, distributions are rebinned until the statistical error per bin is at least 5%. Next all local extrema are identified. The bins around smallest extrema are iteratively

1082 merged until only four local extrema remain. Then distributions are rebinned so  
1083 that statistical uncertainties in each bin are  $< 5\%$ .

1084 For some systematics, up and down variations may be in the same direction  
1085 with respect to the nominal distributions, leading to asymmetric distributions.  
1086 This causes the variations to not cover the nominal choice, and the interpretation  
1087 of the confidence interval is skewed. This asymmetry may also lead to uncon-  
1088 strained systematics in the fit. To handle such asymmetric systematics, if the up  
1089 and down variation for a given systematic are in the same direction for at least  
1090 three  $m_{VV}$  bins the variation is averaged for those bins. The averaging proce-  
1091 dure replaces bin-by-bin the up and down variation bins by  $b_{\pm}^{new} = b_{nom} \pm \frac{|b_+ - b_-|}{2}$ ,  
1092 where  $b_{nom}$  is the nominal bin content and  $b_{\pm}$  are the original up and down varia-  
1093 tion bin content. The same procedure is also applied to any variations where the  
1094 integral of the difference between the up/down variation and the nominal distri-  
1095 bution is twice that of the other down/up variation, further ensuring variations  
1096 are symmetric around the nominal distribution.

1097 Finally, systematics that have a negligible effect on the  $m_{VV}$  distribution are  
1098 not considered in the fit. Shape systematics where no bin in the variational dis-  
1099 tribution deviates more than 1% from the nominal distribution (after normalizing  
1100 all histograms to the nominal) are not included in the fit. Also, statistical bin  
1101 uncertainties  $< 1\%$  are ignored.

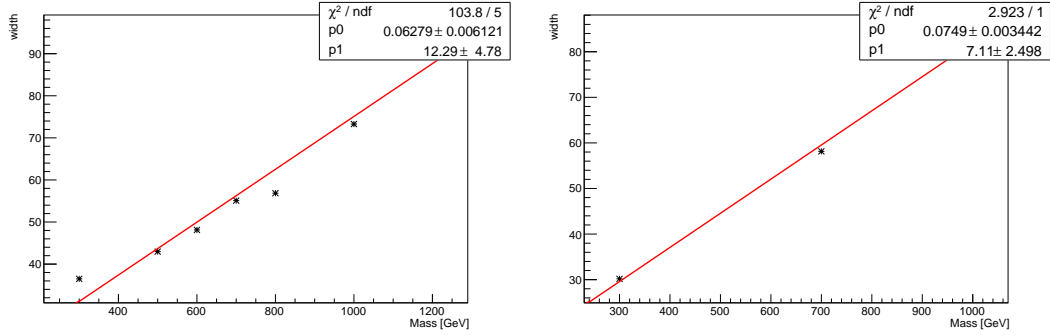


**Figure 9.1:** The HVT signal mass resolution as a function of mass fit with a straight line in the Resolved ggF region (left) and VBF (right) region.

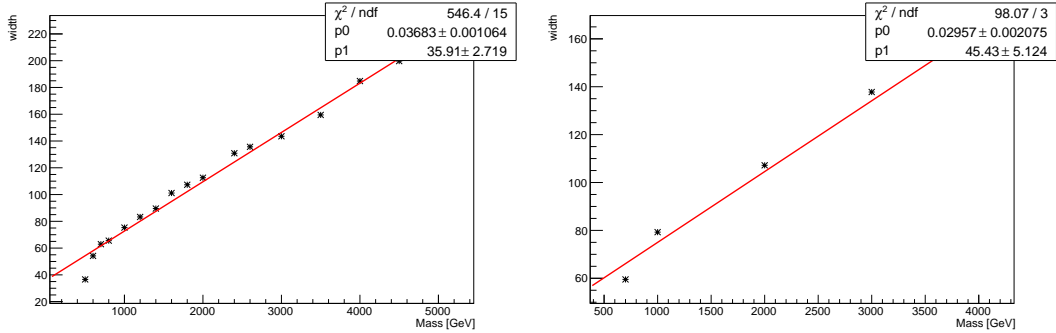


**Figure 9.2:** The HVT signal mass resolution as a function of mass fit with a straight line in the Merged ggF region (left) and VBF (right) region.

### 1102    9.3 Best Fit $\mu$

1103    The best fit signal strength parameter is denoted by  $\hat{\mu}$  and calculated by  
 1104    maximizing the likelihood function with respect to all systematics and  $\mu$ . The  
 1105    corresponding set of systematics that maximize the likelihood are given by  $\hat{\mu}$ .  
 1106    The first term in the likelihood is maximized when the expected number of signal  
 1107    and background events is equal to the number of events in data ( $n_{ci} = \mu s_{ci} +$   
 1108     $b_{ci}$ ). Thus, by maximizing the likelihood, the fit determines values of  $\mu$  and  $\theta$   
 1109    that give the best agreement between expected and measured event yields. The

1110 second term in the likelihood is a penalty term which decreases the likelihood  
1111 when systematics are shifted from their nominal values. This prevents the fit  
1112 from profiling systematics in unphysical ways to maximize the likelihood. The  
1113 uncertainty on  $\mu$  is calculated by varying  $\mu$  up and down until the natural log of  
1114 the likelihood function shifts by one-half.

## 1115 9.4 Discovery Test

1116 To determine if the observed dataset is consistent with tested signal model a  
1117 likelihood ratio is constructed:

$$\lambda(\mu) = \frac{\mathcal{L}(\mu, \hat{\theta}_\mu)}{\mathcal{L}(\hat{\mu}, \hat{\theta})} \quad (9.2)$$

1118 The denominator in this equation is the maximized value of  $\mathcal{L}$  over all system-  
1119 atics and  $\mu$ . The numerator is the maximized likelihood over all systematics for  
1120 a given  $\mu$  value, where the maximized systematics are given by  $\hat{\mu}_\mu$ . To test for  
1121 the existence of signal the observed dataset the null hypothesis ( $H_0$ ) is defined as  
1122 the background only hypothesis and the alternate hypothesis includes signal and  
1123 background ( $H_1$ ). This test quantifies the compatibility of observed data with  
1124  $H_0$  by calculating a p-value representing the probability of observing data as dis-  
1125 crepant or more than the observed data under the  $H_0$ . The test statistic used to  
1126 calculate this p-value is given by ( $r_0$ ):

$$r_0 = \begin{cases} -2 \ln \lambda(0), \hat{\mu} > 0 \\ +2 \ln \lambda(0), \hat{\mu} < 0 \end{cases} \quad (9.3)$$

1127 The expected distribution of the the test statistic under  $H_0$  ( $f(r_0|0)$ ) is used to  
1128 calculate the p-value:

$$p_0 = \int_{r_0, obs}^{\infty} f(r_0 | 0) dr_0 \quad (9.4)$$

1129        Small p-values indicate the observed data is poorly described by  $H_0$ . This  
 1130   equivalent Z-score of a given p-value is usually used to further quantify the agree-  
 1131   ment between the observed data and  $H_0$ . The Z-score is given by the number of  
 1132   standard deviations away from the mean of a Gaussian distribution, the integral  
 1133   of the upper tail of the distribution would equal the p-value. Mathematically:

$$Z = \Phi^{-1}(1 - p_0) \quad (9.5)$$

1134        where  $\Phi$  is the Gaussian cumulative distribution function. The statistical  
 1135   significance of these tests are expressed as the  $Z$ -score. In particle physics,  $3\sigma$  is  
 1136   considered evidence for new phenomena and  $5\sigma$  is the threshold for discovery.

## 1137   **9.5 Exclusion Limits**

1138        In the absence of discovery, upper limits on the signal strength,  $\mu$  are set using  
 1139   the CLs method [cite P60]. The test statistic for this test,  $q_\mu$ , is constructed as:

$$\tilde{\lambda}_\mu = \begin{cases} \frac{\mathcal{L}(\mu, \hat{\theta}_\mu)}{\mathcal{L}(\hat{\mu}, \hat{\theta})}, \hat{\mu} > 0 \\ \frac{\mathcal{L}(\mu, \hat{\theta}_\mu)}{\mathcal{L}(0, \hat{\theta}_0)}, \hat{\mu} < 0 \end{cases} \quad (9.6)$$

$$\tilde{q}_\mu = \begin{cases} -2 \ln \tilde{\lambda}(\mu), \hat{\mu} < \mu \\ +2 \ln \tilde{\lambda}(\mu), \hat{\mu} > \mu \end{cases} \quad (9.7)$$

1140        As defined, larger values of  $q_\mu$  correspond to increasing incompatibility between  
 1141   the observed data and the background + signal hypothesis. The observed value  
 1142   of the test statistic,  $q_{\mu, obs}$ , is then compared to its expected distribution,  $f$ , to

1143 calculate p-values to assess the likelihood of the background+signal hypothesis.

1144 Using these distributions,  $CL_s$  values are computed as:

$$CL_{s+b} = \int_{q_{\mu,obs}}^{\infty} f(q_{\mu}|\mu) dq_{\mu} \quad (9.8)$$

1145

$$CL_b = \int_{q_0^{obs}}^{\infty} f(q_{\mu}|\mu = 0) dq_{\mu} \quad (9.9)$$

1146

$$CL_s = \frac{CL_{s+b}}{CL_b} \quad (9.10)$$

1147  $CL_{s+b}$  is the p-value for the signal + background hypothesis and  $CL_b$  is the  
1148 p-value for the background only hypothesis. The  $CL_s$  value is interpreted as  
1149 the probability to observe the background + signal hypothesis normalized to the  
1150 probability of background-only hypothesis. Normalizing by  $CL_b$  prevents setting  
1151 artificially strong exclusion limits due to downward fluctuations in data.

1152 In this analysis,  $\mu$  values are scanned for each bin in the fit to find the  $\mu$  value  
1153 that yields  $CL_s=0.05$ , meaning the likelihood of finding data more incompatible  
1154 with the signal+background hypothesis (relative to the background only hypoth-  
1155 esis) is 5%. The 95% upper limit on the cross section is then calculated as the  
1156 product of the  $\mu$  value found, branching ratio, and theory cross section.

## Part IV

1157

## Results

1158

1159 **Chapter 10**

1160 **Statistical Interpretation**

1161 **10.1 Discovery Tests**

1162 To test for the existence of signal in the observed dataset, the discovery tests  
1163 discussed earlier are used to calculate p-values as a function of resonance mass.  
1164 The results of these tests are shown in Figures 10.1 - 10.5. Across the different  
1165 DY signals the largest excesses are  $\sim 2.2\sigma$  at 600 GeV and  $1.8\sigma$  at 2 TeV. The  
1166 largest excesses for VBF signals are  $< 2.5\sigma$  at for 1 TeV resonances. As these  
1167 deviations do not constitute discoveries, upper limits on  $\mu$  are calculated.

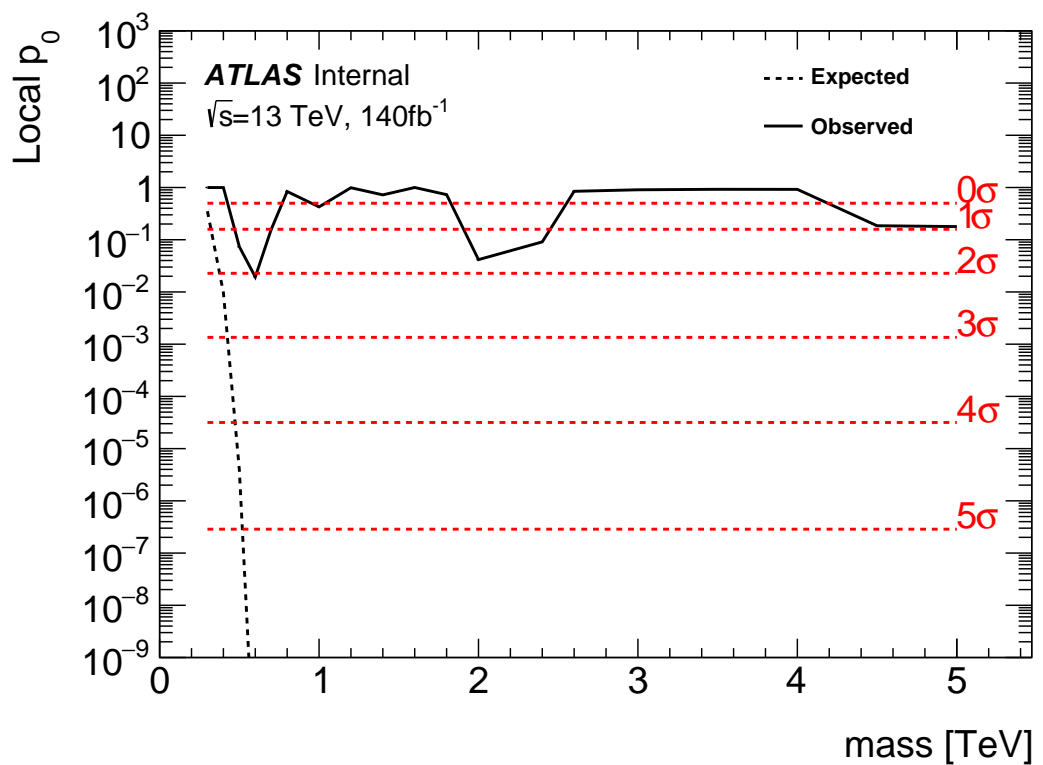


**Figure 10.1:** These plots show the measured  $p_0$  value as a function of resonance mass for HVT Z' DY production.

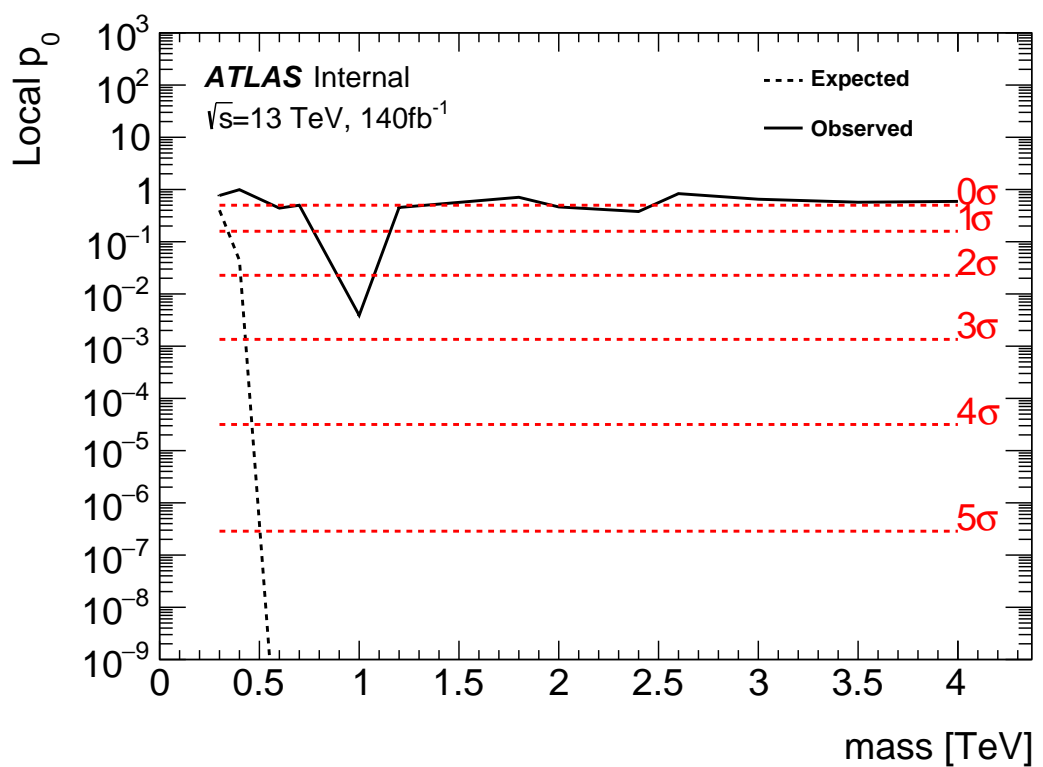


**Figure 10.2:** These plots show the measured  $p_0$  value as a function of resonance mass for HVT Z' VBF production.

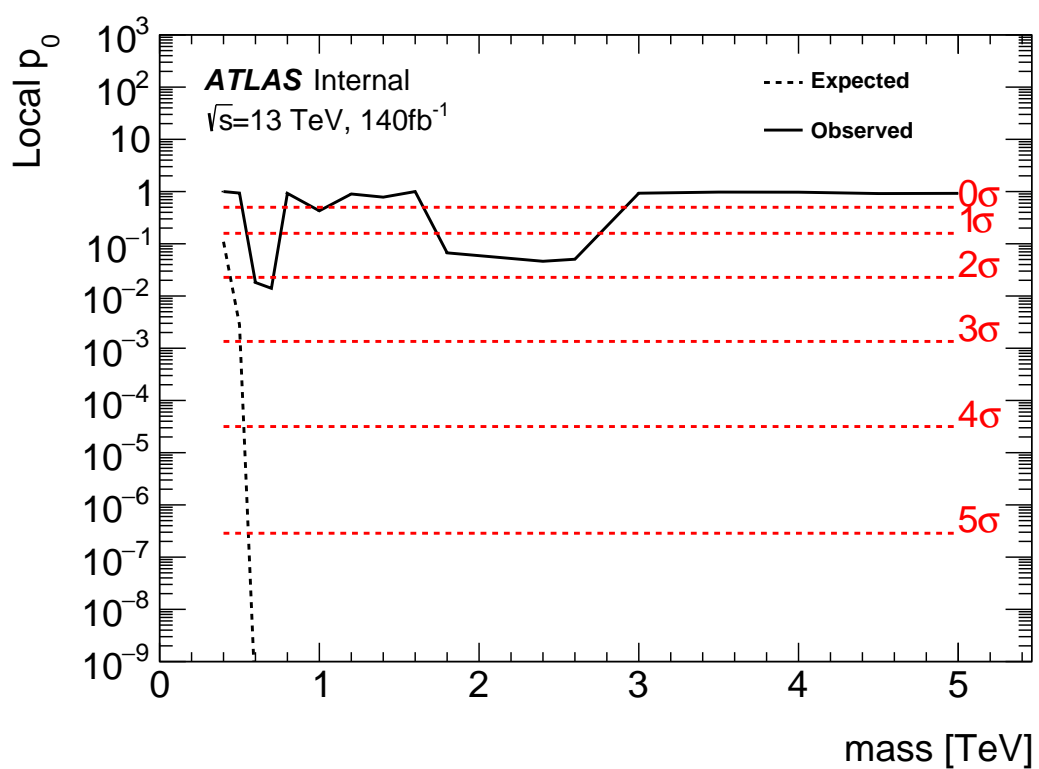


**Figure 10.3:** These plots show the measured  $p_0$  value as a function of resonance mass for HVT W' DY production.

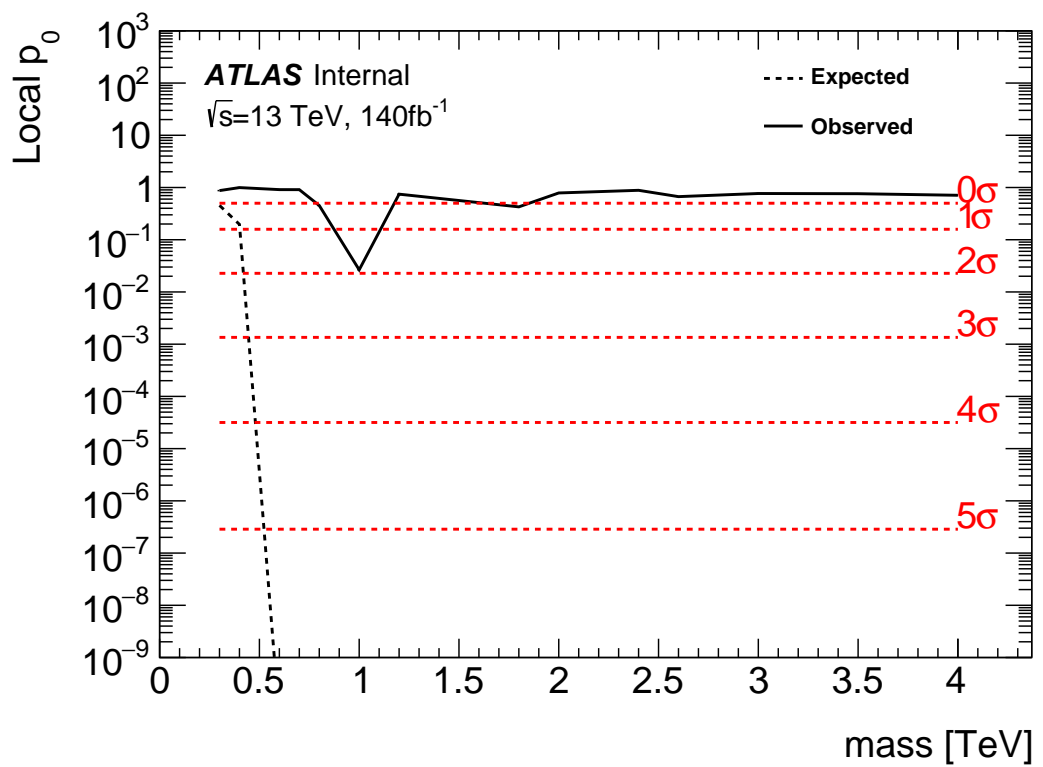


**Figure 10.4:** These plots show the measured  $p_0$  value as a function of resonance mass for HVT W' VBF production.

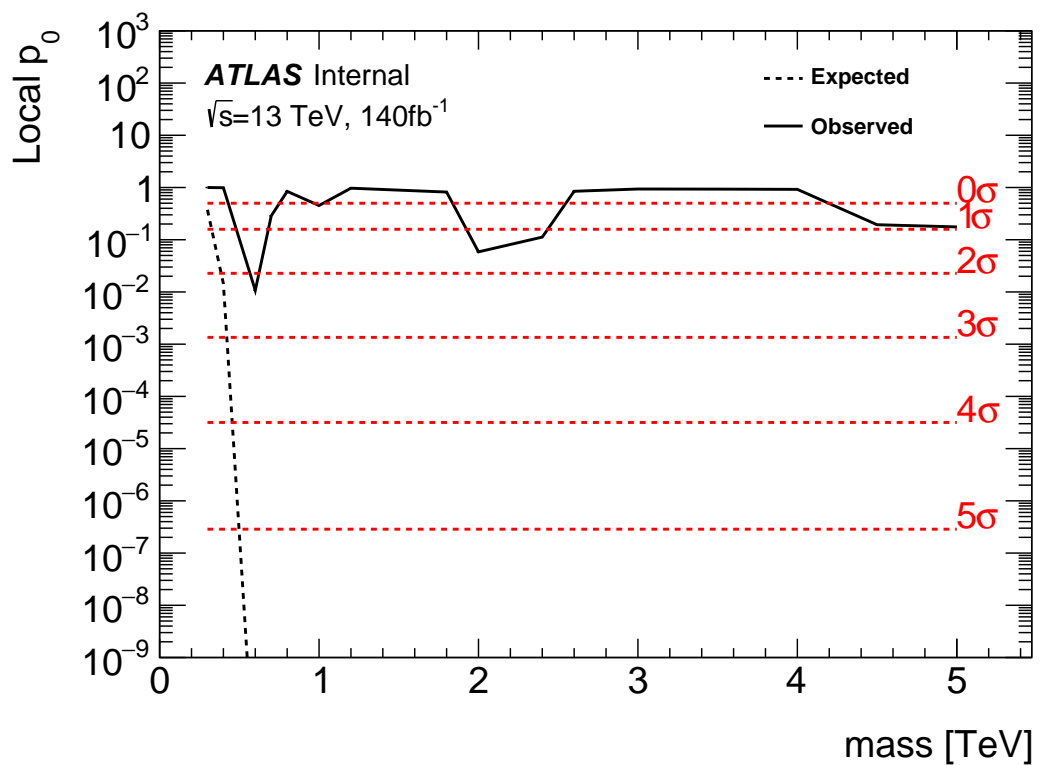


**Figure 10.5:** These plots show the measured  $p_0$  value as a function of resonance mass for the RS Graviton DY production.

<sub>1168</sub> **10.2 Systematic Profiling and Correlations**

<sub>1169</sub> **10.3 Expected and Measured Yields**

<sub>1170</sub> **10.4 Limits**

<sup>1171</sup>

## Part V

<sup>1172</sup>

## Quark and Gluon Tagging

<sub>1173</sub> **Chapter 11**

<sub>1174</sub> **Prospects**

<sub>1175</sub> For the resolved analysis, signal jets are quark enriched and background jets are  
<sub>1176</sub> gluon dominated. By classifying jets in the event as quark or gluon initiated, less  
<sub>1177</sub> background would contaminate the signal region. Figure 11.1 shows the PDGID  
<sub>1178</sub> for the truth parton matched to the jet (meaning the highest energy parton in  
<sub>1179</sub> the jet catchment area) in events passing the resolved signal region selections.  
<sub>1180</sub> PDGID = -1 corresponds to pileup jets,  $0 < \text{PDGID} < 6$  correspond to quarks  
<sub>1181</sub> and  $\text{PDGID} = 21$  corresponds to gluons. From this Figure, it is evident that a  
<sub>1182</sub> notable fraction of the background that contaminates the signal region contains  
<sub>1183</sub> gluon jets, especially for the sub-leading jet.

<sub>1184</sub> As gluons jets have more constituents and therefore more tracks ( $n_{trk}$ ), the  
<sub>1185</sub> background jets have more tracks than the signal jets. This is shown in Fig-  
<sub>1186</sub> ure 11.2. Therefore, by cutting on the number of tracks in a jet, quark and gluon  
<sub>1187</sub> jets may be distinguished (i.e. jets with less than a given number of tracks are  
<sub>1188</sub> classified as a quark, otherwise the jet is classified as a gluon.) Moreover, as the  
<sub>1189</sub> momentum of the jet increases the number of tracks also increases logarithmically.  
<sub>1190</sub> Therefore by applying a cut on the number of tracks that scales with the  $\ln(p_T)$   
<sub>1191</sub> is more powerful than a threshold cut on the number of tracks. Figure 11.3-

1192 Figure 11.6 show normalized heat maps of  $\ln(p_T)$  vs the number of reconstructed  
1193 tracks for the background and a 300 GeV Z' signal. In these plots it is evident  
1194 that the number of tracks in the background jets grows more quickly with  $\ln(p_T)$   
1195 than for the signal jets. This is expected given that the signal is quark dominated  
1196 and the background is gluon dominated.

1197 In Figure 11.8 is the ROC Curve for quark gluon tagging with cut on the  
1198 number of tracks in a jet that depends on  $\ln(p_T)$ . The sum of the backgrounds in  
1199 the signal region were used for this curve. Here the quark tagging efficiency is the  
1200 ratio of quarks tagged as quarks to the total number of quarks in the signal region.  
1201 The gluon rejection is calculated as the reciprocal of the gluon tagging efficiency.  
1202 Choosing a 90 efficient working point with a rejection of 1.4 corresponds to a slope  
1203 of 4 and intercept of -5. Focusing on the background in Figure 11.9, this cut helps  
1204 minimize gluon contamination in the signal region. Also, from these heat maps it  
1205 is obvious that the number of tracks in gluon jets grows more quickly than those  
1206 in quark jets.

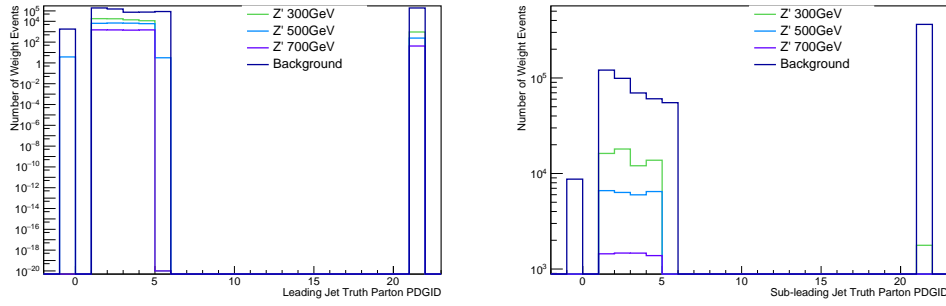


**Figure 11.1:** PDGID of the truth-level parton matched to the small-R jets passing the Resolved GGF WW Signal Region selections for the (a) Leading (b) Sub-Leading jets . These distributions are shown for 300, 500, and 700GeV Z' signals and the background.

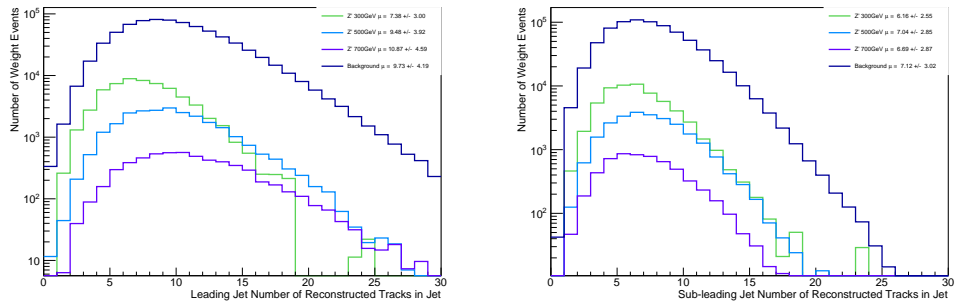


**Figure 11.2:** The number of tracks in small-R jets in events passing the Resolved GGF WW Signal Region selections for the (a) Leading (b) Sub-Leading jets. These distributions are shown for 300, 500, and 700GeV Z' signals and the background.

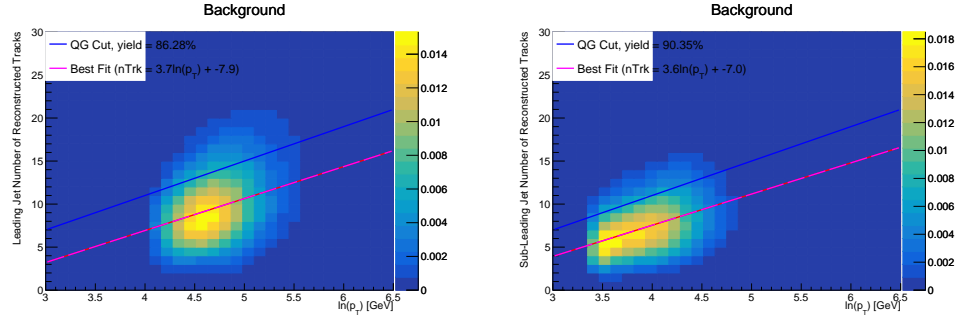


**Figure 11.3:** The number of tracks in background small-R jets in events passing the Resolved GGF WW Signal region selection vs.  $\ln(p_T)$  for (a)Leading (b) Sub-Leading jets. The best fit line for the distribution is also shown, as well as the percentage of jets that pass a cut of number of tracks  $< 4 \times \ln(p_T) - 5$ . Note the number of total entries in these plots has been normalized to one.

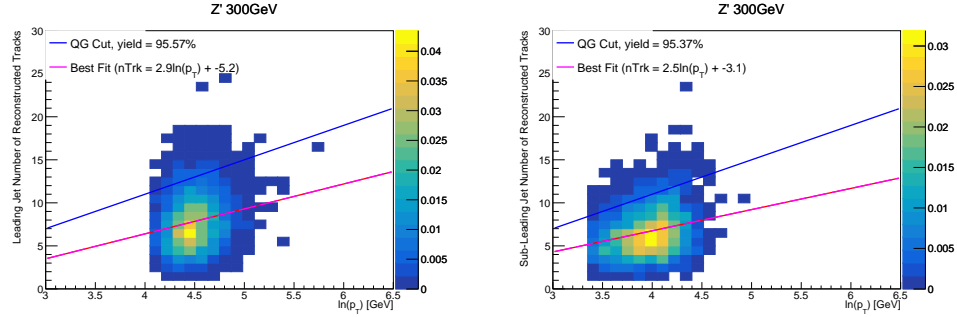


**Figure 11.4:** The number of tracks in small-R jets in 300GeV  $Z'$  events passing the Resolved GGF WW Signal region selection vs.  $\ln(p_T)$  for (a)Leading (b) Sub-Leading jets. The best fit line for the distribution is also shown, as well as the percentage of jets that pass a cut of number of tracks  $< 4 \times \ln(p_T) - 5$ . Note the number of total entries in these plots has been normalized to one.

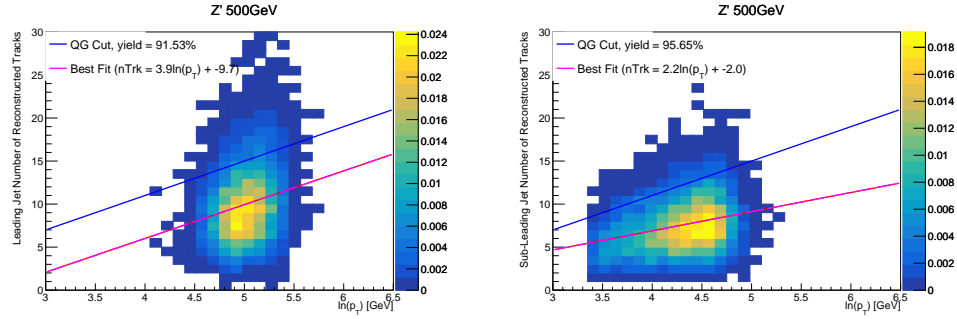


**Figure 11.5:** The number of tracks in small-R jets in 500GeV  $Z'$  events passing the Resolved GGF WW Signal region selection vs.  $\ln(p_T)$  for (a)Leading (b) Sub-Leading jets. The best fit line for the distribution is also shown, as well as the percentage of jets that pass a cut of number of tracks  $< 4 \times \ln(p_T) - 5$ . Note the number of total entries in these plots has been normalized to one.

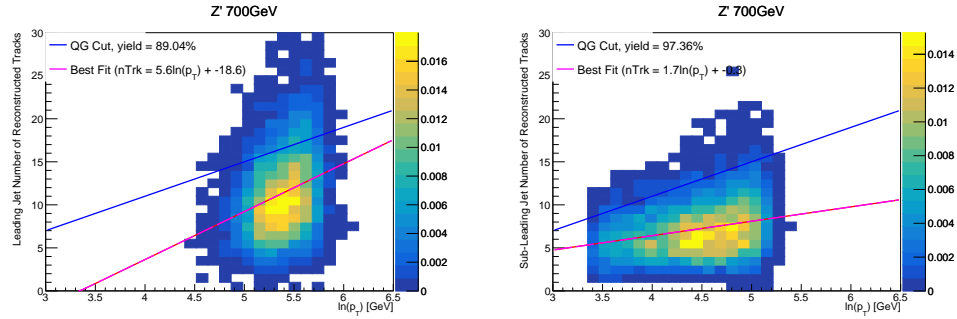


**Figure 11.6:** The number of tracks in small-R jets in 700GeV  $Z'$  events passing the Resolved GGF WW Signal region selection vs.  $\ln(p_T)$  for (a)Leading (b) Sub-Leading jets. The best fit line for the distribution is also shown, as well as the percentage of jets that pass a cut of number of tracks  $< 4 \times \ln(p_T) - 5$ . Note the number of total entries in these plots has been normalized to one.

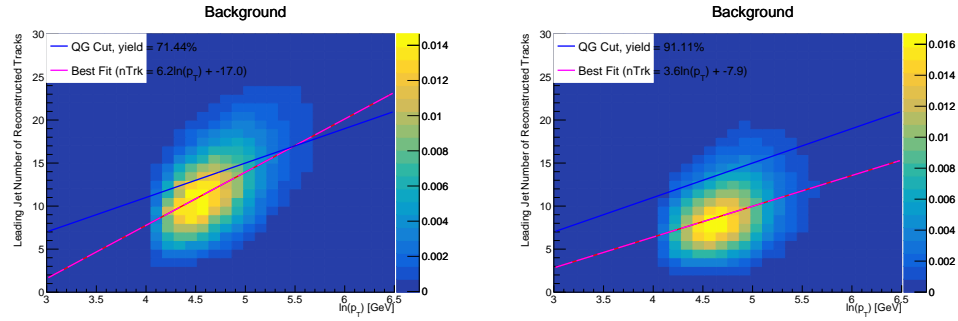


**Figure 11.7:** The number of tracks in leading small-R jets in background events passing the Resolved GGF WW Signal region selection vs.  $\ln(p_T)$  for (a)Gluons (b) Quarks jets. The best fit line for the distribution is also shown, as well as the percentage of jets that pass a cut of number of tracks  $< 4 \times \ln(p_T) - 5$ .Note the number of total entries in these plots has been normalized to one.

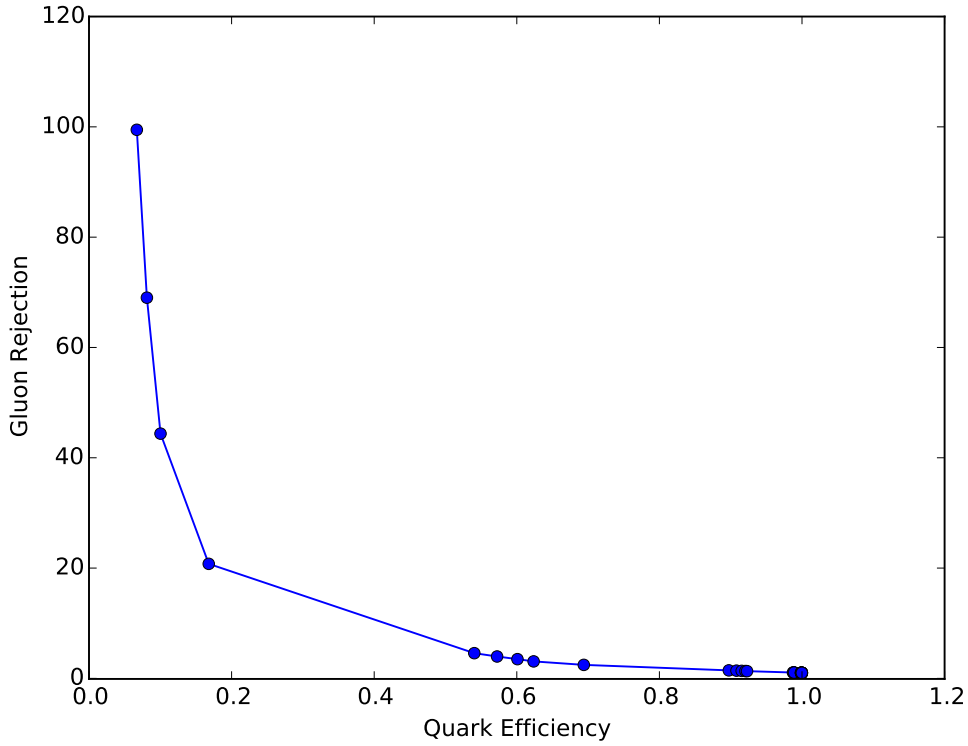


**Figure 11.8:** ROC Curve for Quark and Gluon Tagging with a cut on the number of tracks that depends on the  $\ln(p_T)$ .

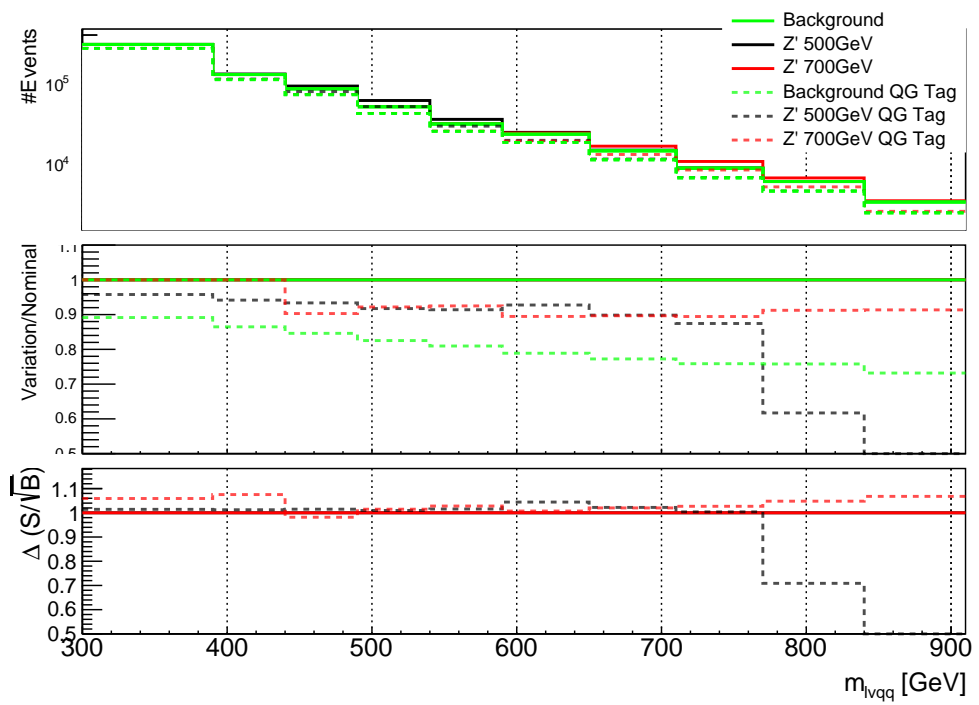


**Figure 11.9:** The top panel shows the distribution of  $m_{lvqq}$  with and without quark gluon tagging. The middle panel shows the ratio of the signals and backgrounds with and without quark gluon tagging. The bottom panel shows the change in  $S/\sqrt{B}$  with quark gluon tagging.

<sub>1207</sub> **Chapter 12**

<sub>1208</sub>  **$n_{trk}$  Calibration**

<sub>1209</sub> As tagger based on nTrk cuts on the number of tracks in jets, a quantity that  
<sub>1210</sub> is not known with infinite precision, relevant systematic uncertainties must be  
<sub>1211</sub> evaluated. The sources of uncertainty in  $n_{trk}$  may be split into modeling and  
<sub>1212</sub> experimental uncertainties.

<sub>1213</sub> Modeling uncertainties are obtained by assessing PDF and ME uncertainties  
<sub>1214</sub> on the number of charged particles in particle-level jets in dijet events. The  
<sub>1215</sub> number of charged particles as a function of jet  $p_T$  is calculated using an Iterative  
<sub>1216</sub> Bayesian (IB) technique [cite paper].

<sub>1217</sub> This measurement ([7]) uses the ATLAS 2012 pp collision dataset, correspond-  
<sub>1218</sub> ing to  $20.3/\text{fb}$  at center-of-mass energy  $\sqrt{s} = 8\text{TeV}$ . Monte Carlo (MC) samples  
<sub>1219</sub> are used to determine the response matrix. The MC sample is a dijet sample gen-  
<sub>1220</sub> erated with Pythia 8.175 using CT10 PDF and AU2 tune. The anti- $k_T$  algorithm  
<sub>1221</sub> is used to cluster jets with a radius parameter  $R = 0.4$ . Jets are required to have  
<sub>1222</sub>  $|\eta| < 2.1$ . Tracks in jets are required to have  $p_T > 500\text{MeV}$ ,  $|\eta| < 2.5$ , track-fit  
<sub>1223</sub>  $\chi^2 < 3.0$  and originate from the primary vertex. Matching tracks to jets is accom-  
<sub>1224</sub> plished using ghost-association [cite]. In this technique, jets are re-clustered with  
<sub>1225</sub> the track collection augmented with "ghost" versions of tracks. These "ghosts"

1226 tracks have the same direction as their parent track, but infinitesimal track  $p_T$ .  
1227 This insures meta-jet properties (e.g.  $\eta$ ,  $p_T$ , etc) are unchanged. A track is  
1228 matched to a jet if it's ghost version remains in the jet after re-clustering. Further  
1229 details of the data, object, and event selection may be found in [cite 35].

1230 To select dijet topologies events are required to have at least two jets with  
1231  $p_T > 50\text{GeV}$  that are relatively well-balanced ( $p_T^{\text{lead}}/p_T^{\text{sub-lead}} < 1.5$ ).

1232 In the IB technique, the prior distribution and number of iterations are the  
1233 inputs [cite Bayesian paper]. The IB response matrix connects number of charged  
1234 particles to the number of tracks in jets determined using the simulated samples.  
1235 This response matrix is used to unfold data to extract the  $n_c$ . Before applying  
1236 the response matrix a fake factor is applied. This accounts for jets that pass  
1237 detector level selections, but not particle level selections. Following this, the IB  
1238 method iteratively applies the response matrix using the nominal Pythia 8.175  
1239 sample as a prior. The number of IB iterations is chosen to minimize unfolding  
1240 bias and statistical fluctuations. For this measurement four iterations was found  
1241 to be optimal by minimizing the unfolding bias from pseudodata simulated with  
1242 Herwig++ with a prior from Pythia 8 AU2. Finally, the inefficiency factor is  
1243 applied to account for events passing particle level selection but not detector  
1244 level, yielding the unfolded nCharged distribution.

1245 This process is prone to three main sources of bias: response matrix, correction  
1246 factor, and unfolding procedure uncertainties. The response matrix is sensitive to  
1247 experimental uncertainties impacting jet track reconstruction and calorimeter jet  
1248  $p_T$ . Correction factors are also sensitive to experimental uncertainties (e.g. JES)  
1249 as such uncertainties modify detector level acceptance. Sensitivity to particle level  
1250 acceptance is calculated by comparing Pythia and Herwig. Finally, the bias from  
1251 the IB prior choice is determined by reweighting the particle-level spectrum, so

1252 the simulated detector level spectrum more closely matches the uncorrected data.  
 1253 Unfolding this modified detector-level simulation and comparing it re-weighted  
 1254 particle-level spectrum indicates bias from the prior distribution choice.

1255 A summary of all the systematic uncertainties associated with this unfolding  
 1256 may be found in [ref paper]. Total uncertainties are < 7% for the number of  
 1257 charged particles in jets. The unfolded distribution of the nCharged in jets from  
 1258 data are further analyzed to extract the quark and gluon nCharged distributions.  
 1259 In dijet events, the jet with a larger  $\eta$  is more energetic and therefore more likely  
 1260 to be a quark. This is due to the quarks in protons generally having a larger  
 1261 fraction of the total momentum of the proton constituents. The more central jet  
 1262 is more likely to be a gluon-initiated jet. This correlation between jet  $\eta$  and flavor  
 1263 may then be used to extract nCharged in  $p_T$  bins using:

$$\langle n_c^f \rangle = f_q^f \langle n_c^q \rangle + f_g^f \langle n_c^g \rangle \quad (12.1)$$

$$\langle n_c^c \rangle = f_q^c \langle n_c^q \rangle + f_g^c \langle n_c^g \rangle \quad (12.2)$$

1264  
 1265 In this equation the f and c subscripts denote the more forward and central  
 1266 jets, respectively. The q and g subscripts denote quark and gluon. The fraction  
 1267 of more forward jets that are say gluons is denoted by  $f_g^f$ . The other relevant jet  
 1268 fractions are denoted with the same naming scheme. Finally,  $\langle n_c \rangle$  is the average  
 1269 number of charged particles in a jet in a given  $p_T$  bin. To show that Eq. (??) may  
 1270 be used to extract quark and gluon  $n_c$  distributions the extracted distributions  
 1271 are compared to  $n_c$  distributions determined using the jet flavor in simulation.  
 1272 Figure [add figure natasha] shows that the extracted and true distributions differ  
 1273 by < 1% over the  $p_T$  ranged probed for this study. Moreover, this implies that  $n_c$   
 1274 depends only on the flavor of the initiating parton and jet  $p_T$ .

1275 These extracted distributions are prone to PDF and ME biases. The bias from

1276 the choice of the CT10 PDF for the Pythia sample is accounted for by comparing  
1277 quark/gluon fractions for the nominal CT10 sample with its eigenvector variations.  
1278 Comparing the quark/gluon fractions from Pythia 8 and Herwig++ quantify the  
1279 uncertainty from the ME calculation. These uncertainties are added in quadra-  
1280 ture with the unfolding uncertainty to give the total modelling uncertainty on  
1281 the extracted  $n_c$  distribution. This is shown in Figure 13.2.

1282 To apply these uncertainties in  $n_c$  distributions in data, per-jet event weights  
1283 are associated with each uncertainty according to:

$$w_i(n_c) = \frac{P(n_c | < n_c > \pm \sigma_{n_c}^i)}{P(n_c | < n_c >)} \quad (12.3)$$

1284 In Eq. (??), i denotes the uncertainty considered, P is the Poisson probability,  
1285 and  $\sigma_{n_c}^i$  represents the average impact of the uncertainty on  $n_c$ .

1286 The previous uncertainties described accounted for modeling uncertainty as-  
1287 sociated with the number of charged particles in a jet. However,  $n_c$  is not a  
1288 measurable quantity. Instead the number of tracks in a jet is measured, which is  
1289 a proxy for  $n_c$ . Therefore the uncertainties associated with the measurement of  
1290 nTracks must also be considered ([9]). These uncertainties were calculated using  
1291 a Pythia 8 dijet sample with NNPDF 23. Track reconstruction efficiency and fake  
1292 rates are the dominant sources of nTrack uncertainties.

1293 The track reconstruction efficiency is effected by the uncertainty of the de-  
1294 scription of the ID material in simulation and the modeling of charged-particle  
1295 interactions with this material. These uncertainties are accounted for by varying  
1296 the ID material by 5-25% (dependent on the region of the detector considered).  
1297 The difference in the tracking efficiency between the nominal and varied simula-  
1298 tion give the uncertainty on the track reconstruction efficiency. Another important  
1299 source of track reconstruction efficiency arises in the core of jets. The high density

1300 of tracks in the jet cores can cause ID clusters to merge. The fraction of lost tracks  
 1301 due to merging is given by the fraction of tracks that have a charge of two mini-  
 1302 mum ionizing particles. This quantity is compared between data and simulation  
 1303 resulting in an uncertainty of 0.4% on tracks with  $\Delta R < 0.1$ . Combining these  
 1304 effects gives a total uncertainty as a function of  $p_T$  and  $\eta$  that is generally  $< 2\%$   
 1305 [references figure 44 from [9]).]

1306       Fake tracks are the other dominant source of nTrk uncertainty. Fake tracks  
 1307 are tracks that cannot be associated to a single particle. Often these tracks are a  
 1308 result of random combinations of hits from charged particles that overlap in space.  
 1309 In dense environments, such as the core of jets or high-pileup environments, fake  
 1310 tracks are more likely. Fake tracks are estimated with a 'control region method'  
 1311 which is briefly summarized here [[8]]. By applying a series of track selections  
 1312 to enrich the fraction of fake tracks (e.g.  $|d_0| > 0.1$ , track  $\chi^2 > 1.4$ , etc) in  
 1313 simulation, templates for fake track parameters are calculated. These templates  
 1314 are then fit to data to determine the fraction of fake tracks. On average the fake  
 1315 rate is found to be 30% (independent of  $p_T$  and  $\eta$ ).

1316       To assess the impact of these two detector level uncertainties, tracks are ran-  
 1317 domly dropped according to the rates described above. Reconstruction and fake  
 1318 uncertainties both lower the number of tracks, hence these uncertainties are one-  
 1319 sided. By dropping tracks in this way a varied nTrk distribution is calculated for  
 1320 both uncertainties. The associated per-jet event weights are then calculated in  
 1321 the same way as the modeling weights as:

$$w_i(n_c) = \frac{P(n_{trk} | < n_{trk} > \pm \sigma_{n_{trk}}^i)}{P(n_{trk} | < n_{trk} >)} \quad (12.4)$$

1322       Adding the modeling and detector level uncertainties in quadrature gives the  
 1323 overall nTrack uncertainty. The effects of the individual uncertainties on the nTrk

1324 distributions can be seen in Fig 13.4. Fig 13.3 shows the  $m_{lvqq}$  and nTrk distri-  
1325 butions for the W and Top control regions before likelihood fitting. In these plots  
1326 the nTrk uncertainties improve agreement between data and MC. The remaining  
1327 differences are likely covered by likelihood fitting and improving the analysis itself.

<sub>1328</sub> **Chapter 13**

<sub>1329</sub> **Application**

<sub>1330</sub> Using the 90% WP of the  $n_{trk}$  tagger improves  $S/\sqrt{B}$  is  $< 3\%$  as shown in  
<sub>1331</sub> Figure 11.9. Although,  $n_{trk}$  is the single most powerful discriminating variable  
<sub>1332</sub> for quark and gluon jets, the addition of other jet variables would improve the  
<sub>1333</sub> classification efficiency. Figure 13.1 shows the possible improvement of 10%  
<sub>1334</sub> in jet classification using the truth label of the jets to classify jets. This type of  
<sub>1335</sub> improvement is possible by using variables such as jet width, and energy correlata-  
<sub>1336</sub> tors. Figure [add BDT figure/use 1612.01551.pdf] shows for a 90% quark tagging  
<sub>1337</sub> efficiency for a 100 GeV jet, a BDT improve the gluon rejection by 0.4. Once this  
<sub>1338</sub> tagger is calibrated it would improve the analysis sensitivity of this channel.

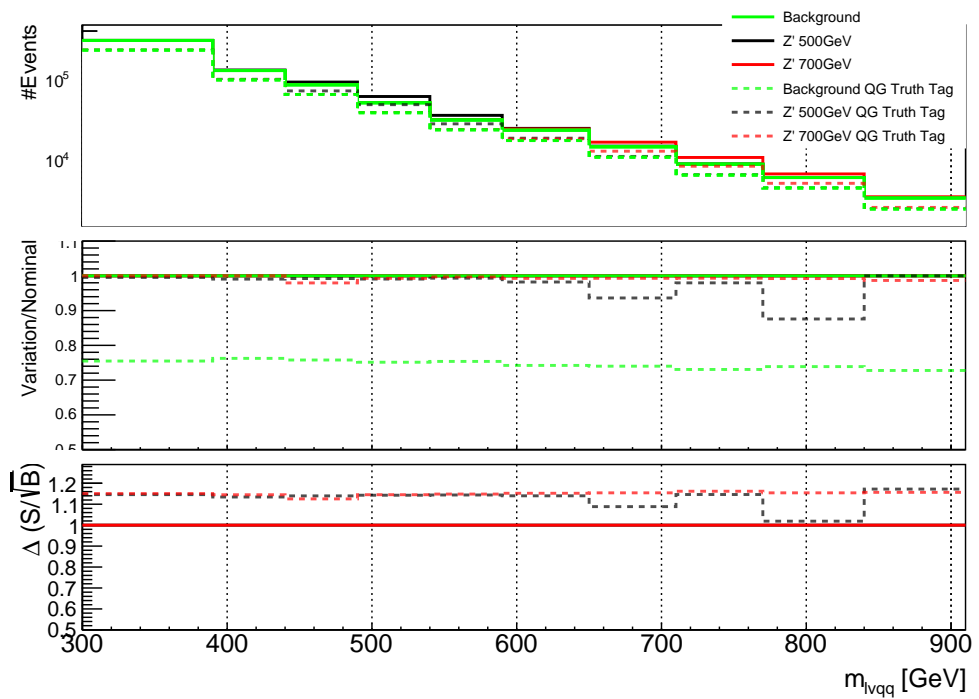


**Figure 13.1:** The top panel shows the distribution of  $m_{lvqq}$  with and without requiring jets to be true quarks. The middle panel shows the ratio of the signals and backgrounds with and without requiring jets to be true quarks. The bottom panel shows the change in  $S/\sqrt{B}$  when requiring jets to be true quarks..

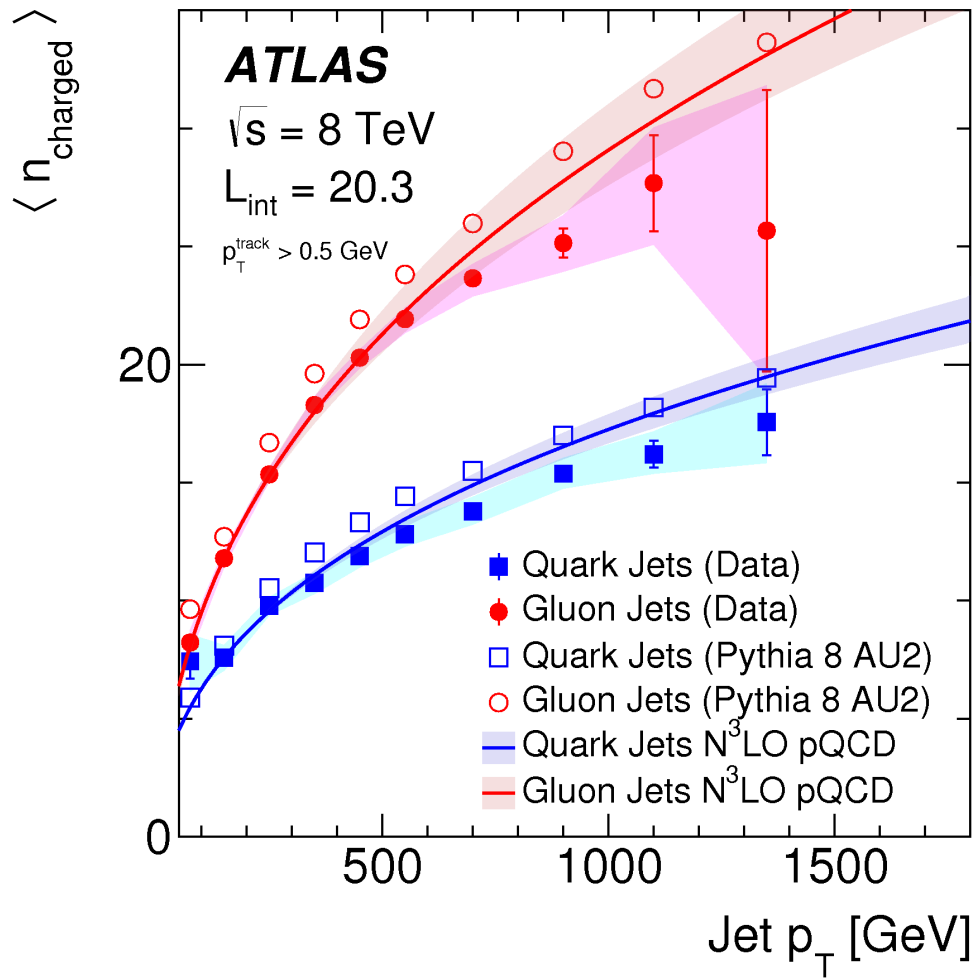


**Figure 13.2:** Unfolded and extracted  $n_C$  qg dstbs..

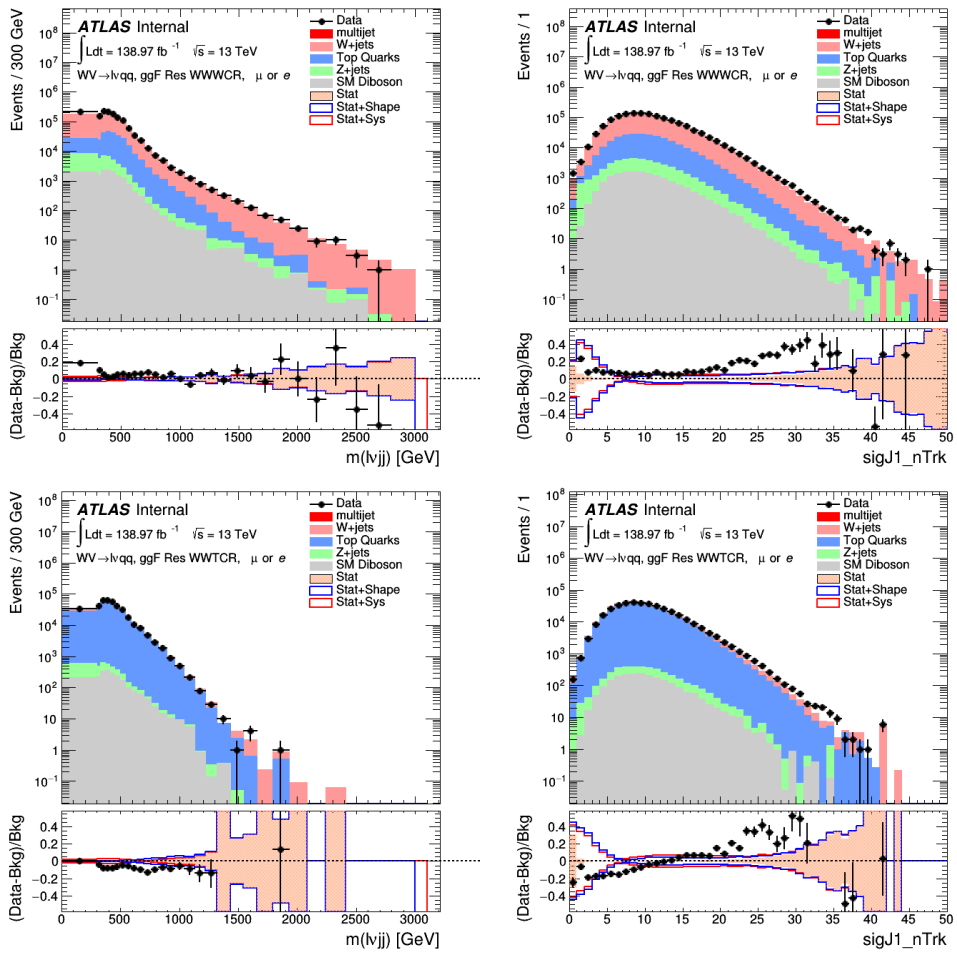


**Figure 13.3:** PDGID of the truth-level parton matched to the small-R jets passing the Resolved GGF WW Signal Region selections for the (a) Leading (b) Sub-Leading jets . These distributions are shown for 300, 500, and 700GeV  $Z'$  signals and the background.

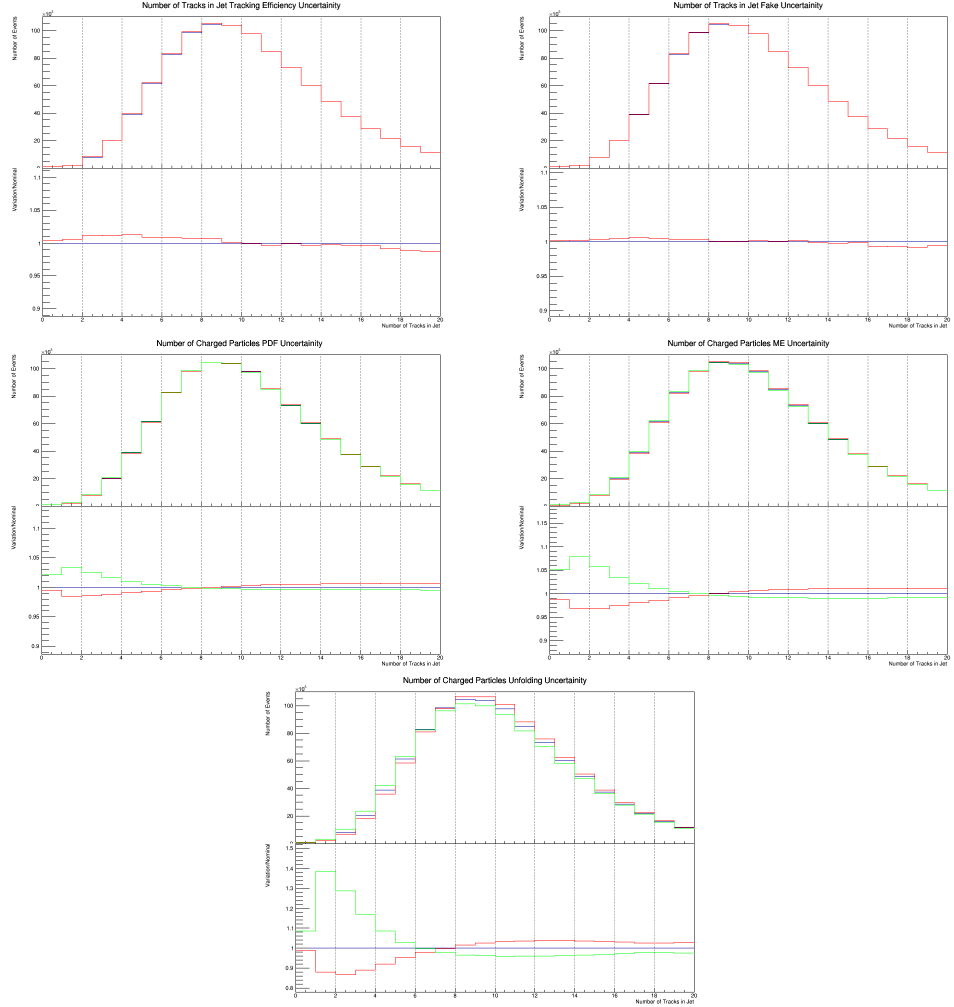


**Figure 13.4:** These figures show the impact of the uncertainties on the number of tracks in the leading jet in the sum of the background sample in the Resolved GGF WW SR (a) tracking efficiency (b) fake (c) PDF (d) ME (e) unfolding uncertainties.

## **Part VI**

1339

## **Conclusion**

1340

<sub>1341</sub> Chapter 14

<sub>1342</sub> Conclusions

<sub>1343</sub> This is where conclusions go.

# Bibliography

- [1] Lecture notes particle physics ii.
- [2] Kaustubh Agashe, Hooman Davoudiasl, Gilad Perez, and Amarjit Soni. Warped Gravitons at the LHC and Beyond. *Phys. Rev.*, D76:036006, 2007.
- [3] G. Altarelli and G. Parisi. Asymptotic freedom in parton language. *Nuclear Physics B*, 126(2):298 – 318, 1977.
- [4] ATLAS Collaboration. Atlas muon reconstruction performance in lhc run 2.
- [5] ATLAS Collaboration. Summary plots from the atlas standard model physics group.
- [6] ATLAS Collaboration. Jet energy scale measurements and their systematic uncertainties in proton–proton collisions at  $\sqrt{s} = 13$  tev with the atlas detector. arXiv: 1703.09665 [hep-ex].
- [7] ATLAS Collaboration. Measurement of the charged-particle multiplicity inside jets from  $s=\sqrt{8}$  tev pp collisions with the atlas detector. arXiv:1602.00988 [hep-ex].
- [8] ATLAS Collaboration. Performance of the atlas track reconstruction algorithms in dense environments in lhc run 2. arXiv:1704.07983 [hep-ex].
- [9] ATLAS Collaboration. Properties of jet fragmentation using charged particles measured with the atlas detector in pp collisions at  $\sqrt{s} = 13$  tev. arXiv:1906.09254 [hep-ex].
- [10] Alex Dias and V. Pleitez. Grand unification and proton stability near the peccei-quinn scale. *Physical Review D*, 70, 07 2004.
- [11] Stefan Höche, Frank Krauss, Marek Schönherr, and Frank Siegert. Qcd matrix elements + parton showers. the nlo case. *Journal of High Energy Physics*, 2013(4), Apr 2013.
- [12] Gregory Soyez Matteo Cacciari, Gavin P. Salam. The anti- $k_T$  jet clustering algorithm. arXiv:0802.1189 [hep-ph].

- 1371 [13] Duccio Pappadopulo, Andrea Thamm, Riccardo Torre, and Andrea Wulzer.  
1372 Heavy vector triplets: bridging theory and data. *Journal of High Energy*  
1373 *Physics*, 2014(9), Sep 2014.
- 1374 [14] Antonio Pich. The Standard Model of Electroweak Interactions. In *Proceed-*  
1375 *ings, High-energy Physics. Proceedings, 18th European School (ESHEP 2010):*  
1376 *Raseborg, Finland, June 20 - July 3, 2010*, pages 1–50, 2012. [,1(2012)].
- 1377 [15] Lisa Randall and Raman Sundrum. A Large mass hierarchy from a small  
1378 extra dimension. *Phys. Rev. Lett.*, 83:3370–3373, 1999.
- 1379 [16] Tania Robens and Tim Stefaniak. Lhc benchmark scenarios for the real higgs  
1380 singlet extension of the standard model. *The European Physical Journal C*,  
1381 76(5), May 2016.